



University of Calgary

PRISM: University of Calgary's Digital Repository

Graduate Studies

The Vault: Electronic Theses and Dissertations

2019-01-22

The Large-Scale Structure of Magnetic Fields Associated with Filamentary Molecular Clouds

Tahani, Mehrnoosh

Tahani, M. (2019). The Large-Scale Structure of Magnetic Fields Associated with Filamentary Molecular Clouds (Unpublished doctoral thesis). University of Calgary, Calgary, AB.

<http://hdl.handle.net/1880/109508>

doctoral thesis

University of Calgary graduate students retain copyright ownership and moral rights for their thesis. You may use this material in any way that is permitted by the Copyright Act or through licensing that has been assigned to the document. For uses that are not allowable under copyright legislation or licensing, you are required to seek permission.

Downloaded from PRISM: <https://prism.ucalgary.ca>

UNIVERSITY OF CALGARY

The Large-Scale Structure of Magnetic Fields Associated with Filamentary Molecular Clouds

by

Mehrnoosh Tahani

A THESIS

SUBMITTED TO THE FACULTY OF GRADUATE STUDIES
IN PARTIAL FULFILLMENT OF THE REQUIREMENTS FOR THE
DEGREE OF DOCTOR OF PHILOSOPHY

GRADUATE PROGRAM IN PHYSICS AND ASTRONOMY

CALGARY, ALBERTA

JANUARY, 2019

© Mehrnoosh Tahani 2019

Abstract

Magnetic fields pervade the interstellar medium and are believed to be important in the star formation process. However, probing magnetic fields in these star forming regions is challenging. I propose and demonstrate a new method, using Faraday rotation measurements, to probe the direction and magnitude of the magnetic field along the line-of-sight in and around filamentary molecular clouds that are forming stars.

Using my method, which utilises rotation measure data from the literature, a chemical evolution code, and extinction maps to estimate electron column density, I determine the magnetic field in four nearby molecular clouds: Orion A, Orion B, Perseus, and California. I find that my method produces results in agreement with the limited number of available Zeeman measurements.

Using the magnetic field results from this new method, I find that the line-of-sight magnetic field on either side of the California and Orion A filaments has opposing magnetic field directions. Three theoretical magnetic field morphologies can explain this change of direction across filaments: toroidal, helical, and bow morphologies. I investigate these three models by combining my results with those of Planck observations to determine the 3D magnetic field structure in Orion A. I find that of the three possible morphologies, toroidal is the least probable whereas the bow morphology is the most natural.

To investigate these morphologies further, I use magnetohydrodynamics simulations to simulate filamentary molecular clouds and their magnetic field evolution. I use different initial parameters to see if the magnetic field lines can become twisted around a rotating filament, potentially forming helical fields. I find that helical fields are not easily generated in these scenarios.

Acknowledgements

First, I would like to sincerely thank my supervisors, René Plume and Jo-Anne Brown, who patiently and considerately taught me important communicating, presenting, collaborating, critical thinking, teaching, and writing skills. Above all, they gave me an opportunity to work on a research topic that has captivated me and has made me a much happier individual. I thank René for his selfless dedication and support.

I would like to acknowledge Christoph Simon, David Knudsen, and Robert Thompson, who supported me in my decision to switch my research topic midway through my program and to start working with René and Jo-Anne in January 2015. They clearly demonstrated that to them the happiness of each member of the department matters the most.

My supervisory committee, David Hobill and David Knudsen, have provided very helpful feedback throughout my project. I particularly would like to thank David Hobill for his keen help and for taking the time to answer questions and discuss concepts. During my PhD program, I also learned from and was encouraged by other faculty members including Michael Wieser, Ann-Lise Norman, and Marzena Kastyak-Ibrahim. I am grateful that the Physics and Astronomy department has compassionate and caring people like those I have mentioned.

I would like to thank my collaborators, Ralph Pudritz, Daniel Seifried, Jouni Kainulainen, and Juan Soler. Ralph Pudritz and Corey Howard welcomed me on my visit to the Physics department at McMaster University. Ralph Pudritz, Corey Howard, and Mikhail Klassen gave me a boost up when I started working with FLASH and simulations. Moreover, the support team of Compute Canada, particularly Doug Phillips and Dimitri Rozmanov, have

been a great help. Their quick responses were greatly appreciated.

Daniel Seifried generously shared his knowledge and previous code, as well as providing comments on Chapter 5. He patiently explained FLASH concepts through many emails and Skype conversations. My FLASH simulations would have taken much longer without his help. Jouni Kainulanen quickly provided extinction maps along with thoughtful and helpful comments and discussions on the work presented in Chapters 3 and 4. Juan Soler provided the dust polarisation map for the work presented in Chapter 4. Tim Robishaw provided excellent detailed information on Zeeman measurements.

The U of C Physics Department office staff have been invaluable during my degree: Camilla Mascardo, Carlos Villafuerte, Gerri Evans, Helen Werner, Marni Farrant, Susan Taylor, and Tracy Korsgaard. They have made the department friendly and welcoming. I am especially grateful for Tracy Korsgaard, as she goes above and beyond to make sure that the Physics and Astronomy graduate students have pleasant years during their programs.

I would like to thank my colleagues and friends, Kianoosh Tahani, Pamela Freeman, Anna Ordog, Cameron Van Eck, James Campbell, Ambrish Raghooonundun, Russell Shanahan, and Robert Bell (in no particular order), for many astrophysics discussions. I would particularly like to thank Pamela Freeman and Robert Bell for providing editorial comments on Chapters 1 and 2, respectively.

I feel so lucky to have had Mark Bryant as my office-mate for the last four years, with many conversations on Alfvén waves, non-ideal MHD, magnetic fields, and philosophical concepts. He has also continuously provided me with fantastic writing tips and feedback. Further, I would like to acknowledge John Mather who provided me with general academic and science advice over the phone and through emails. He has been an inspiration for my personal and academic life.

I would also like to mention my friends Stephanie Becker, Maryam Mozaffari, Anahita Alavi, Sandi and Dave Kyle, Neda Amiri, Jill Blackie, and Nasrin Pak (in no particular order), for being there for me when I needed it, no matter how far or near.

Last but not least, I would like to thank my family, particularly my father, my mother, and my brother, Kianoosh. They have always been a great support. My father introduced me to the world of physics and astrophysics and we had countless enthusiastic astrophysics discussions over the years, until he was no longer *here*. His achievement of his dream despite all the odds, his love of learning, and his faith in me have been a true inspiration. I am also immensely grateful for my mother's love and support. Her astonishing creativity, thirst for learning, and her quick, peaceful adaptation to life challenges have always been a reminder for me to think outside-the-box.

Dedicated to the three most influential people in my life, who believed in me whole-heartedly:

My Father, in his loving memory

My Mother

and

My Mentor, René Plume.

Table of Contents

Abstract	ii
Acknowledgements	iii
Dedication	vi
Table of Contents	vii
List of Figures and Illustrations	x
List of Tables	xii
List of Symbols, Abbreviations and Nomenclature	xiii
Epigraph	xvi
1 Magnetism in Star Formation	1
1.1 From the Interstellar Medium to the Stars	1
1.1.1 Molecular Clouds and Filaments	2
1.2 Roles of Magnetism in Star Formation	6
1.2.1 First Observations	6
1.2.2 Magnetism and the Evolution of Molecular Clouds	7
1.3 Thesis Work	9
2 Background Concepts	10
2.1 Faraday Rotation Measurements	10
2.2 Dust Polarisation Detection	18
2.3 Zeeman Measurements	20
2.4 Theoretical Studies of Magnetic Fields	21
2.4.1 MagnetoHydroDynamics (MHD) Equations	23
3 A New Method to Measure Magnetic Fields Strengths Associated with Filamentary Molecular Clouds	26
3.1 Previous Work and Assumptions	27
3.1.1 Free Electrons in MCs	27
3.2 Data	28

3.2.1	Rotation Measure Catalog	28
3.2.2	Extinction Map	31
3.3	Methodology	31
3.3.1	Estimating RM _{OFF} and RM _{ref}	34
3.3.2	Obtaining the Electron Column Densities	37
3.3.3	Uncertainty Analysis and Sensitivity Study	42
3.4	Results	49
3.4.1	Strength and Morphology of B _{LOS} in Orion A & B	49
3.4.2	California and Perseus	53
3.5	Discussion	56
3.5.1	Decreasing the Uncertainties in B _{LOS}	56
3.5.2	Magnetic Field Morphology: Evidence for Helical Fields?	57
3.5.3	Comparison with Previous Measurements: A Word of Caution	60
3.6	Conclusions	62
4	The 3D Magnetic Field in Orion A	70
4.1	Introduction	71
4.2	Observations	73
4.3	Methodology	75
4.3.1	Constructing the 3D Magnetic Field Vectors	75
4.3.2	Modeling a Toroidal and a Helical 3D Magnetic Field	78
4.3.3	Modeling a Bow Magnetic Field Morphology	80
4.3.4	3D Magnetic Fields: Observed versus Modeled	82
4.4	Results of Modeling	83
4.4.1	The Toroidal Morphology	86
4.4.2	The Helical Morphology	86
4.4.3	The Bow Morphology	88
4.5	Discussion	92
4.5.1	Modified Magnetic Field Strengths	92
4.5.2	Tilted Models for Orion A	95
4.5.3	Selecting the Best Magnetic Field Morphology	96
4.6	Modeling Conclusions	98
5	Magnetohydrodynamics Simulations	100
5.1	The FLASH Units	101
5.1.1	Gravity	101
5.1.2	Adaptive Mesh Refinement and Sink Particles	102
5.1.3	MHD Solver	104
5.1.4	Equation of State	105
5.2	The Input Parameters	105
5.2.1	Density Profile	106
5.2.2	Turbulence	108
5.2.3	Filament Rotation	111
5.3	Setting Up FLASH and Preparing the Input Files	112
5.4	Computational Resources	114

5.5	Running FLASH - The Evolution of the Box	115
5.6	Results	117
5.6.1	Visualising the Results	117
5.6.2	Small-Scale Filaments	118
5.6.3	Large-Scale Filaments	133
5.7	Discussion	137
6	Summary and Conclusion	141
6.1	Summary	141
6.2	Major Contributions	143
6.3	Future Work	144
6.3.1	Observations	144
6.3.2	Theoretical Simulations	145
	Bibliography	147

List of Figures and Illustrations

1.1	Phases of star formation	3
1.2	Filamentary structures and cores	4
1.3	Filamentary structures in the Galaxy	5
1.4	Helical magnetic morphology	8
2.1	Faraday rotation	11
2.2	Taylor et al. (2009) Rotation Measure catalog	15
2.3	Finding RM	16
2.4	Galactic magnetic fields	17
2.5	The dust polarisation technique	19
2.6	Hydrodynamics in nature	22
3.1	RM map in California and Perseus MCs	29
3.2	RM map in Orion region	30
3.3	Schematic illustrating “ON” and “OFF” RM positions	33
3.4	Magnetic field values in OMC-A using different numbers of OFF positions .	36
3.5	B_{LOS} in the Perseus MC	43
3.6	Uncertainties in B_{LOS} due to the chemical code inputs	47
3.7	B_{LOS} in OMC-A	48
3.8	B_{LOS} in OMC-B	51
3.9	B_{LOS} in the California MC	54
3.10	The average of absolute value of B_{LOS} versus extinction	62
4.1	Wrapping of magnetic fields lines around a cylindrical filamentary structure .	72
4.2	B_{LOS} in Orion A	74
4.3	Geometry and coordinates for a filament	76
4.4	Frame of reference in Orion A	77
4.5	Observed B_x , B_y , and B_z	84
4.6	B_{LOS} result combined with PXXXV B_{POS}	85
4.7	Best fit tests for modeled toroidal and helical fields	87
4.8	Best fit tests of bow magnetic morphology.	89
4.9	Modeled bow magnetic morphology compared with data	91
4.10	Observed B_{POS} and B_{LOS} values	93
4.11	Best fit test of modeled toroidal and helical fields with modified observation values	94
4.12	Bow magnetic morphology compared with modified values	95

4.13	Bow magnetic morphology compared with modified values	96
4.14	Plane-of-sky component of magnetic field in Orion as obtained by Planck observations	98
5.1	An illustration of the parent- and child-blocks	103
5.2	An illustration of the filament and its dimensions	107
5.3	An end-on view of the filament with a slice orthogonal to the z-axis	119
5.4	Density evolution of a small-scale filament with initial perpendicular magnetic field and an initial observed filament rotation rate	120
5.5	Magnetic field evolution of a small-scale filament with initial perpendicular field and an initial observed filament rotation rate	121
5.6	Curving of magnetic field lines around the filament due to pressure	122
5.7	Magnetic hourglass morphology due to self-gravity	123
5.8	Magnetic field of a small-scale filament at different z-layers with initial perpendicular field	125
5.9	Evolution of perpendicular field lines with high rotation	126
5.10	Magnetic field evolution of a small-scale filament with initial perpendicular field in the absence or rotation or turbulence	128
5.11	Density evolution of a small-scale filament with initial parallel magnetic field	130
5.12	Magnetic field evolution of a small-scale filament with initial parallel magnetic field	131
5.13	Density evolution of a small-scale filament with initial parallel magnetic field and a high rotation rate	132
5.14	Magnetic morphology of a filament with initial parallel field lines and high rotation frequency in an end-on view	133
5.15	Density evolution of large-scale filamentary MC	135
5.16	Evolution of an initially perpendicular magnetic field morphology of a large-scale filamentary cloud	136

List of Tables

3.1	Orion A MC: B_{LOS} values	64
3.2	Orion A MC: B_{LOS} values with directionality constraints	65
3.3	Orion B MC: B_{LOS} values	65
3.4	California MC: B_{LOS} values	66
3.5	California MC: B_{LOS} values with directionality constraints	67
3.6	Perseus MC: B_{LOS} values	68
3.7	Perseus MC: B_{LOS} values with directionality constraints	69
4.1	Helical field χ^2 values	88
4.2	Bow field χ^2 values	90
5.1	Filamentary time-scales	139

List of Symbols, Abbreviations and Nomenclature

Symbol or abbreviation	Definition
2D	Two Dimensional
3D	Three Dimensional
A_V	Visual Extinction
A_V, MC	Visual Extinction of Molecular Cloud
A_V, ref	Reference Visual Extinction
ALMA	Atacama Large Millimeter/submillimeter Array
AMR	Adaptive Mesh Refinement
APEX	Atacama Pathfinder Experiment
B	Magnetic Field (vector)
B_{LOS}	Line-Of-Sight Magnetic Field Component
B_{POS}	Plane-Of-Sky Magnetic Field Component
c_s	Sound Speed
CMC	California Molecular Cloud
CPU	Central Processing Unit
CR	Cosmic Ray Radiation
DEC	Declination
EMW	ElectroMagnetic Wave
FWHM	Full Width Half Maximum
G	Gravitational Constant
GMC	Giant Molecular Cloud
GPC	General Purpose Cluster
H_2	Molecular Hydrogen
HI	Atomic Hydrogen
HD	HydroDynamics
HDF	Hierarchical Data Format
ISM	InterStellar Medium
J	Current Density Per Unit Area
JCMT	James Clerk Maxwell Telescope
k	Boltzmann Constant
KBHP09	Kainulainen et al. (2009)
K	Kelvin

LOFAR	LOw-Frequency ARray
LOS	Line-Of-Sight
M_{\odot}	Solar Mass
M_J	Jeans Mass
MC	Molecular Cloud
MHD	MagnetoHydroDynamics
MPI	Message-Passing Interface
n_e	Electron Volume Density
N_e	Electron Column Density
N(HI+H ₂)	Hydrogen Column Density
NVSS	NRAO VLA Sky Survey
OMC-A	Orion A Molecular Cloud
OMC-B	Orion B Molecular Cloud
PBS	Portable Batch System
pc	Parsec
PMC	Perseus Molecular Cloud
POS	Plane-Of-Sky
POSSUM	Polarisation Sky Survey of the Universe's Magnetism
PXXXV	Planck Collaboration et al. (2016)
RA	Right Ascension
RM	Rotation Measure
RM _{Gal}	Galactic Contribution in Rotation Measure
RM _{OFF}	The Rotation Measure of an OFF Data Point
RM _{ON}	The Rotation Measure of an ON Data Point
RM _{ref}	The Reference Rotation Measure
Slurm	Slurm Workload Manager
T	Temperature
T_{rot}	Filament's Rotation Period
t_{turb}	Turbulence Time-Scale
TSS09	Taylor et al. (2009)
USM	Unsplit Staggered Mesh
UV	UltraViolet
VLASS	VLA Sky Survey
X _e	Electron Abundance
yr	Year
+ δ B	Upper Limit Magnetic Field Uncertainty
- δ B	Lower Limit Magnetic Field Uncertainty
χ^2	Chi-Square Value
λ_J	Jeans Length
μ G	Micro-Gauss
τ_{ff}	Free Fall Time
ρ	Volume Mass Density
ρ_{charge}	Volume Charge Density
Φ	Gravitational Potential

Epigraph

I happen to have discovered a direct relation between magnetism and light, also electricity and light, and the field it opens is so large and I think rich.

- Michael Faraday

Chapter 1

Magnetism in Star Formation

The space between the stars is filled with a dilute mixture of charged particles, atoms, molecules, and dust grains, known as the InterStellar Medium (ISM; Spitzer 1978). It is this material that ultimately condenses to form stars, planets, and life. Understanding how the stars actually form, however, is a challenging problem. Magnetic fields, which are ubiquitous in the ISM, are believed to be important in the star formation process. To address the problem of star formation, and the role of magnetism in it, I specifically focus on examining the magnetic field morphologies in star-forming regions, both theoretically and observationally. To this end, I present a novel way to map the magnetic fields in star-forming regions. I then construct models to interpret the results obtained from my method and finally, investigate the origin of these magnetic field morphologies in star-forming regions using MagnetoHydroDynamic (MHD) simulations.

1.1 From the Interstellar Medium to the Stars

The ISM contains different regions or phases with different temperature and density conditions. While the warm and hot components (where the temperature, T , is greater than a few thousand Kelvin) fill most of the volume of space, their low density (< 1 particle per cubic centimeter) means they contain very little of the mass. The cold medium in the ISM (where $T <$ a few

hundred Kelvin) contains neutral and ionised atomic gas (mainly atomic Hydrogen, HI, and Carbon, C⁺, respectively), and exists in smaller, denser (> 100 particles per cubic centimeter) regions. These dense regions contain most of the mass of the ISM. The coldest ($T \approx 10\text{-}25\text{ K}$) and densest (> 500 particles per cubic centimeter) regions of the cold medium are known as molecular clouds (MCs) and are composed primarily of neutral molecular gas, with some ionised species as well. It is within these dense molecular clouds that the stars form (André et al. 2010).

1.1.1 Molecular Clouds and Filaments

MCs can have various physical appearances - from somewhat spherical, to elongated and filamentary in shape (André et al. 2014), with sizes from 1 parsec (pc) to 100 pc (Großschedl et al. 2018), where $1\text{ pc} = 3.258$ light years or $3.086 \times 10^{16}\text{ m}$. The largest of these clouds are referred to as Giant Molecular Clouds (GMCs). MCs are believed to be transient features that are constantly forming and being destroyed (Blitz 1987; Larson 1994). This idea is supported by simulations which demonstrate that MagnetoHydroDynamics (MHD) turbulence damps rapidly in MCs (Stone et al. 1998; Mac Low et al. 1998; Padoan and Nordlund 1999). Thus, long MC lifetimes could only be supported if there is a continuous regeneration of MHD turbulence - an idea that has long been problematic. However, Hartmann et al. (2001) show that the majority of MCs in the solar neighborhood appear to be forming young stars, and that the ages of the stars in these clouds are typically $\sim 2\text{ Myr}$. They also show that stellar associations that are older than 10 Myr have no molecular gas - suggesting typical MC lifetimes of less than 10 Myr. Thus, there is no need for a constant injection of turbulence.

Since MCs have been observationally shown to be the nurseries for stellar birth, the first step of star formation is the formation of the MCs themselves. The physics and chemistry of this process, however, still has many open questions.

Among the mechanisms known to be responsible for MC formation, one is that of feedback from nearby, already-formed stars (Dawson 2013). In this feedback-driven cloud formation

process, fast winds are driven from young stars. The collision of these winds with nearby gas clouds causes shock heating and compression of the gas. After the passage of the shock front, this warm, dense gas cools quickly, and rapidly converts the atomic Hydrogen to molecular Hydrogen (H_2), on time-scales of 1-20 Myr, depending on the velocity of the shock front (Bergin et al. 2004).

The two key parameters in the formation of molecules, and by extension MCs, are high volume densities and high column densities (Dawson 2013). Sufficiently high volume densities enable gas clouds to rapidly cool through collisional excitation followed by radiative de-excitation of atomic fine-structure lines and ro-vibrational states of molecular hydrogen. This rapidly cooling, dense gas is conducive to the formation of more complex molecular species through collisional chemical reactions. These newly formed molecules, however, can be quickly destroyed via ultraviolet (UV) radiation from nearby type O and B stars or through Cosmic Ray radiation (CR). High column densities are necessary to shield these molecules from these photo-destruction processes (Goldsmith et al. 2007).

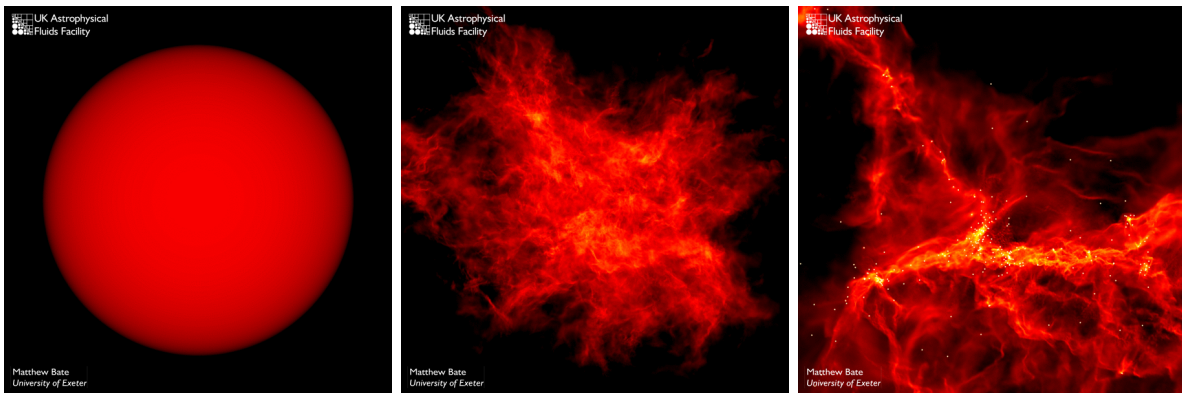


Figure 1.1: Evolution of a homogeneous interstellar cloud in a numerical simulation by Bate (2009). Left panel shows a cloud at time = 0 yr, with physical diameter of 2.6 light-years and containing $500 M_\odot$ of material. During the evolution of the cloud, filamentary structures form first (second panel), and the filaments subsequently form cores and stars (third panel).

After MCs are formed, they can gravitationally collapse to form cores and stars. Cores are the smallest, densest regions within an MC (with sizes around 0.03 to 0.2 pc; Caselli et al. 2002), which form the individual stars. To illustrate this, a theoretical simulation by Bate (2009) follows the evolution of a molecular cloud through to the formation of stars, by perturbing an initially homogeneous spherical cloud. In this process, the cloud first arranges itself into filamentary morphologies as illustrated in Figure 1.1, which subsequently form cores and stars. These simulations have been supported observationally by Herschel Space Observatory¹, which shows that it is these filamentary structures that contain the vast majority of star-forming cores (André et al. 2014). Figure 1.1 indicates these evolutionary stages, in a numerical simulation from an initial homogeneous cloud to filamentary structures and consequently to formation of cores and stars. Figure 1.2 illustrates the Aquila star-forming region as observed by Herschel. The left panel shows the filaments, and the right panel shows that the cores are found within the filaments.

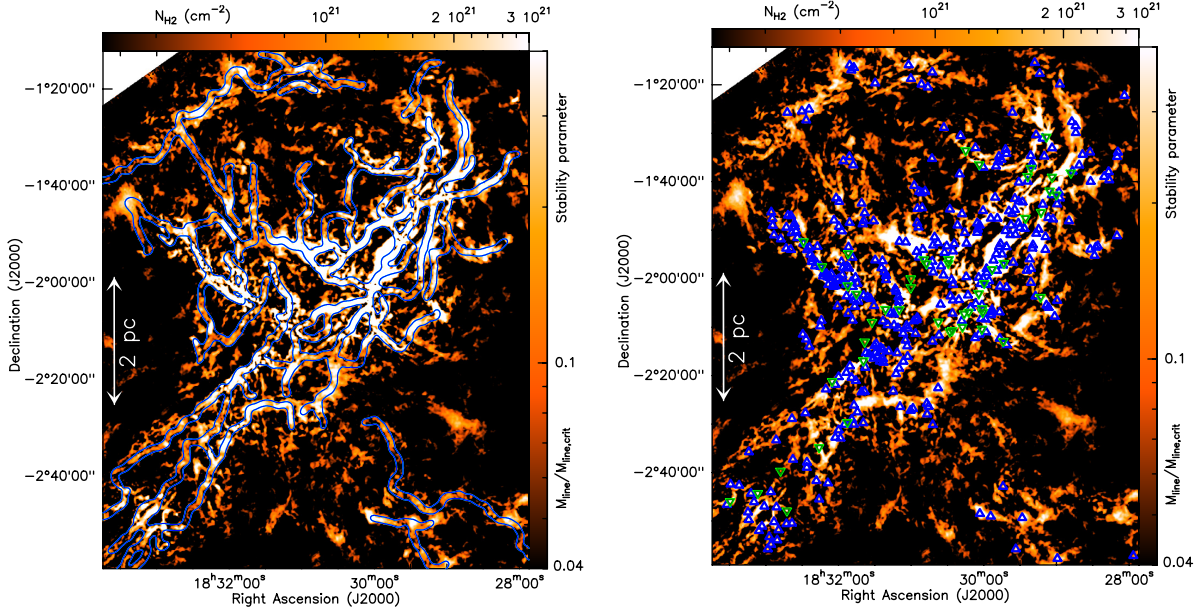


Figure 1.2: Column density map of Aquila cloud Complex as viewed by Herschel. The left panel shows the filaments in the region as traced by the DisPerSE algorithm (Sousbie 2011). The right panel shows the candidate cores in blue and green triangles. Image credit: Figure 11 of Könyves et al. (2015)

¹<https://www.herschel.caltech.edu/>

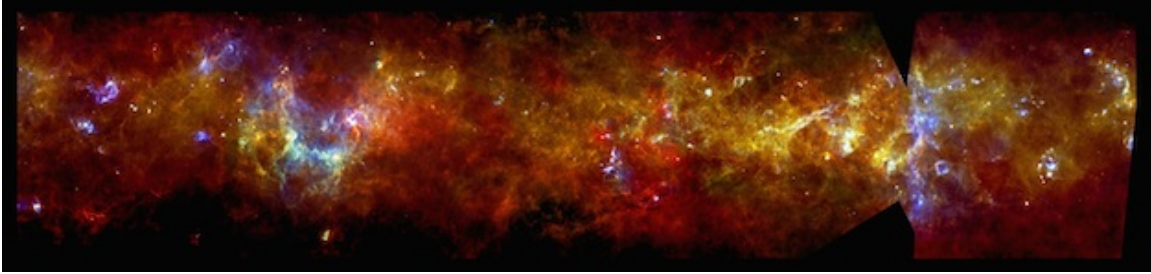


Figure 1.3: The filamentary structure of the Galactic Plane as observed by Herschel. Filamentary structures are ubiquitous in the ISM and molecular filaments are believed to be the nurseries of star formation. Image credit: Molinari et al. (2016), ESA/PACS & SPIRE Consortium, Hi-GAL Project.

Surveys of Herschel, Midcourse Space Experiment (MSX)², and Spitzer Galactic Legacy Infrared Mid-plane Survey Extraordinaire (GLIMPSE)³ revealed that these filamentary structures are ubiquitous in the ISM (André et al. 2010; Churchwell et al. 2009). Figure 1.3 illustrates the filamentary structure of the Galactic Plane observed by Herschel. We often see star-forming cores embedded in larger-scale dense filaments and the most active star-forming regions seem to occur at intersections between massive filaments (Schisano et al. 2014; André et al. 2010; Molinari et al. 2010). Thus, it is clear that molecular filaments are important structures in the path to star formation.

Theoretical simulations by Inoue et al. (2018) suggest that filamentary structures form as a consequence of shock compression of a turbulent molecular cloud and bending of the ambient magnetic field. Observations in and around the Taurus MC by Arzoumanian et al. (2018) support this idea by showing that the observed velocity field seems to be consistent with the scenario of filament formation proposed by Inoue et al. (2018). On smaller physical scales, the gravitational contraction of molecular filamentary structures, to form cores and stars, may be counteracted (e.g Larson 2003) or influenced by different effects such as turbulence (e.g., Padoan et al. 2001), radiative processes (e.g., Krumholz et al. 2010), and magnetic fields (e.g., Mouschovias et al. 2011). In fact, a variety of theoretical (e.g., Mouschovias 1985, 2001; Mouschovias et al. 2009, 2011; Machida et al. 2011; Kunz and Mouschovias 2010;

²<https://irsa.ipac.caltech.edu/data/MSX/mission.htm>

³<https://irsa.ipac.caltech.edu/data/SPITZER/GLIMPSE/>

Klassen et al. 2017) and observational (e.g., Li et al. 2014; Palmeirim et al. 2013; Goldsmith et al. 2008) studies suggest there is a correlation between magnetic fields and each phase of star formation - from the initial formation of the filamentary structures to the formation of cores and stars within them. Thus, magnetic fields play an important role in the overall star formation process.

1.2 Roles of Magnetism in Star Formation

It is only in the last few decades that magnetism has attracted serious attention in the study of star formation and the evolution of filamentary MCs. Magnetic fields in star-forming regions can be thousands to tens of thousands of times weaker than the magnetic field of the Earth (Li et al. 2014; Crutcher et al. 2010). Observed links between the orientation of magnetic field lines and filamentary molecular clouds (MC; Planck Collaboration et al. 2016; Li et al. 2013) show that magnetic fields can be dynamically important in the formation (Li et al. 2014) and evolution (Seifried and Walch 2015) of filaments at different scales. Li et al. (2017) observed that filamentary structures with almost perpendicular magnetic fields have lower star formation rates per solar mass compared to parallel magnetic fields. This highlights the importance of understanding magnetic field morphologies and strengths in star-forming MCs.

1.2.1 First Observations

Magnetic fields in the ISM were initially observed by Hiltner (1949) and Hall (1949). The observations by Hiltner (1949) were performed in an attempt to explain starlight polarisation which he concluded must be due to the ISM and not the stars themselves. Hall (1949) and Hall and Mikesell (1949) subsequently confirmed this idea with additional starlight observations. Spitzer and Tukey (1949), as well as Davis and Greenstein (1949), attributed this ISM polarisation to the alignment of the dust particles perpendicular to the Galactic

magnetic field vectors. Spitzer and Tukey (1949) specifically associated this alignment to ferromagnetic characteristics of the dust particles.

Observations of magnetic fields in filamentary structures were first done by Hall (1955). He observed the starlight polarisation behind a filamentary structure in the Pleiades and found that the dust particles had oriented themselves perpendicular to the filaments. From these observations, he concluded that the plane-of-sky component of magnetic fields (B_{POS}) were parallel to these filaments. The Planck Collaboration et al. (2016) confirmed Hall's observations that the B_{POS} lines tend to be parallel to filamentary structures when the column density is less than $10^{21.7} \text{ cm}^{-2}$ but that it appears to be preferentially perpendicular to filamentary structures when the column densities are higher than this value.

1.2.2 Magnetism and the Evolution of Molecular Clouds

The importance of magnetism in the evolution of MCs is strengthened by the fact that the MCs do not quickly undergo gravitational collapse. It is believed that magnetic fields (and turbulence) act against gravity and prevent a rapid gravitational collapse (Larson 2003). For example, recent observations of magnetic fields in the dense gas of the Pillars of Creation (an active star-forming MC) suggest that magnetic fields in this region ($B_{\text{POS}} = 170 - 320 \mu\text{G}$) are sufficient to provide support against gravitational collapse (Pattle et al. 2018). In other words, magnetism can impact the dynamics and evolution of MCs (e.g Heiles et al. 1993).

More recent observational and theoretical studies have shown that various magnetic field morphologies can have different effects on MC evolution. For example, a helical magnetic field wrapping around a filamentary structure can stabilise the cloud against gravitational collapse (Fiege and Pudritz 2000b). A schematic example of such a helical field is shown in Figure 1.4 for the Orion A region, as suggested by the observations of Heiles (1997) and Buckle et al. (2012). So far, this idea has lacked systematic observational confirmation. On the other hand, the magnetic field morphology in the Pillars of Creation, suggest that while the magnetic fields may be important to prevent gravitational collapse, they might not be

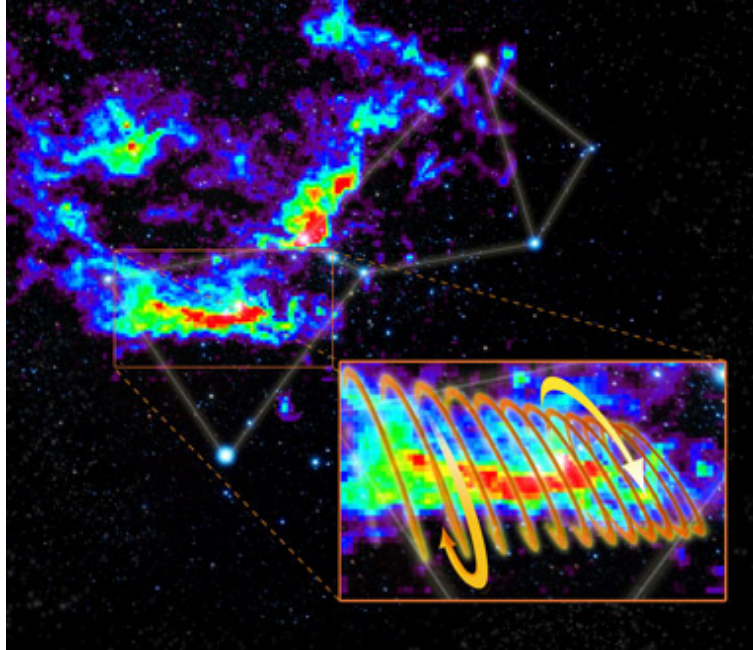


Figure 1.4: Helical magnetic morphology around the Orion A giant filamentary molecular cloud. Different magnetic field morphologies surrounding the filamentary structures can influence star formation in various manners. Image credit: Saxton, Dame, Hartmann, Thaddeus; NRAO/AUI/NSF.

dynamically important in the *formation* of the Pillars (Pattle et al. 2018).

The morphology of the magnetic field in filamentary structures can shed light on their formation and evolution. Simulations show that if a filament is forming due to shear, its magnetic field becomes stronger along the filament's long axis and therefore, becomes largely parallel to the filament (Hennebelle 2013). On the other hand, strong magnetic fields can suppress motion perpendicular to the field lines, but do not affect the parallel motion. Therefore, dense filaments can form by material streaming along the strong field line and will have their long axis oriented perpendicular to the field lines (Koyama and Inutsuka 2002). In other words, field lines that are parallel to the filament's long axis are created and influenced by the dynamics of the filament, whereas the opposite is true for perpendicular field lines. Field lines that are perpendicular to the long axis of the filament help *create* the filament and influence its subsequent dynamics.

Careful theoretical and observational investigations are necessary to understand the details

of how, exactly, magnetism affects the star formation process. While the theoretical studies are fairly well advanced, they are hampered by a lack of observations to compare against. This is mainly because the traditional methods to measure magnetic field strengths in the ISM have a number of inherent difficulties. Thus, there is a need to develop new and novel observational methods to detect magnetic fields in star-forming regions. My thesis addresses this issue by presenting and testing a new technique for measuring the line of sight component of the magnetic fields associated with star-forming molecular filaments.

1.3 Thesis Work

In this thesis, I investigate the magnetic fields in giant filamentary structures both observationally and theoretically. For the observational part, I examine Orion A, Orion B, California and Perseus, and explore the full 3D magnetic field morphologies of Orion A. For the theoretical part, I use MHD simulations to explain my observations in these regions.

My thesis work is presented over six chapters as outlined below.

- Chapter 2: I expand on the present observational and theoretical techniques to measure and understand magnetic fields in star-forming filamentary structures.
- Chapter 3: I propose and demonstrate a new method to map the magnetic fields associated with these star-forming filaments.
- Chapter 4: I investigate the three Dimensional (3D) morphologies of the magnetic fields that are able to explain the observations obtained in Chapter 3.
- Chapter 5: I present numerical MHD simulations to determine the likelihood of these morphologies developing in an evolving filament.
- Chapter 6: I present the overall conclusions of this thesis work, its implication for the role of magnetic fields in star formation, and the future studies which can be done based on this thesis work.

Chapter 2

Background Concepts

Studies of magnetism in the ISM regions are done both theoretically and observationally. In this chapter I focus on the important concepts behind some of the observational and theoretical studies. For the observational background in this chapter, I concentrate on the most common observing techniques to detect magnetic fields in the ISM or MCs. For the theoretical background, I give a brief overview on the concepts behind MagnetoHydroDynamics (MHD) simulations.

The present techniques to find magnetic fields in the ISM include Faraday rotation measurements (e.g., Brown et al. 2008), Zeeman Measurements (e.g., Crutcher 2005), and dust polarisation detections (e.g., Hildebrand 1988; Andersson et al. 2015). A review of these observing techniques can be found in Heiles (1976). Among these techniques, dust polarisation and Zeeman measurements have been successful in mapping magnetic fields of star-forming MCs (Planck Collaboration et al. 2016).

2.1 Faraday Rotation Measurements

When a linearly polarised electromagnetic wave (EMW) propagates through a magnetised region with free electrons, its plane of polarisation will rotate. This phenomenon, as illustrated

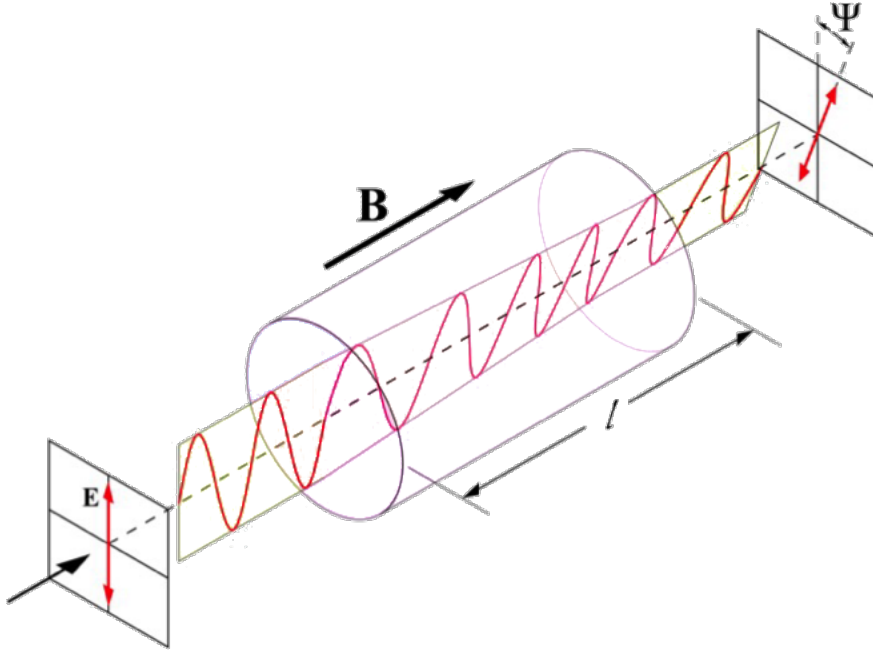


Figure 2.1: Faraday rotation. When a linearly polarised electromagnetic wave goes through a magnetised region that has free electrons, its plane of polarisation rotates. Ψ illustrates the amount of rotation.

in Figure 2.1, is known as Faraday rotation and the amount of rotation is given by

$$\Psi = \lambda^2 \left(0.812 \int n_e \mathbf{B} \cdot d\mathbf{l} \right) = \lambda^2 RM, \quad (2.1)$$

where Ψ is the amount of rotation in radians, \mathbf{B} is the magnetic field of the region in micro-Gauss (μG), λ is the wavelength of the EMW in meters, $d\mathbf{l}$ is the path length through the magnetised region in parsecs, and n_e is the volume electron density of the region in particles per cubic centimeter. The integral value in brackets defines a quantity known as the rotation measure (RM; e.g., Brown et al. 2008).

The rotation of the plane of polarisation is a result of the ISM being a *birefringent medium* in the presence of magnetic fields and free electrons, meaning that it has a different index of refractive for right- and left-circularly polarised EMW. As a result, the two modes have different phase velocities, resulting in their composition, the linearly polarised wave, being rotated relative to the original emission. Wilson et al. (2013) presents a simple step-by-step

derivation and explanation of Faraday rotation.

To follow these steps we need to start with the equation of motion for a free electron in the region with free electrons (ISM for our purpose). The equation of motion describes how an electron responds to both the EMW and \mathbf{B} . In the presence of an external magnetic field (\mathbf{B}), we can write:

$$m_e \ddot{\mathbf{r}} = -e(\mathbf{E} + \dot{\mathbf{r}} \times \mathbf{B}), \quad (2.2)$$

where e is the electron charge, m_e is the electron mass, and \mathbf{E} is the electric field of the EMW. The $\dot{\mathbf{r}}$ term is the first time derivative of the position of the electron (velocity) and $\ddot{\mathbf{r}}$ is the second time derivative (acceleration).

Let us assume that the EMW is propagating in the z-direction and therefore, has E_x and E_y components. For simplicity, we can assume \mathbf{B} is in the z-direction (i.e. $\mathbf{B} = B\hat{z}$). Thus, we have:

$$\begin{aligned} \ddot{r}_x + \frac{e}{m_e} B \dot{r}_y &= \frac{-e}{m_e} E_x, \\ \ddot{r}_y - \frac{e}{m_e} B \dot{r}_x &= \frac{-e}{m_e} E_y. \end{aligned} \quad (2.3)$$

Next I, multiply the second equation of 2.3 by the complex number, $+i$, and add the two lines together. Then, I again multiply the second line of equation 2.3 but, this time, by $-i$, and again add the two lines of equation 2.3. This leads to two new equations which can be described by a single equation (using a \pm sign), as follows:

$$\ddot{r}_{\pm} \mp i \frac{e}{m_e} B \dot{r}_{\pm} = -\frac{e}{m_e} E_{\pm}, \quad (2.4)$$

where r_{\pm} is defined as $r_x \pm ir_y$ and E_{\pm} is defined as $E_x \pm iE_y$, to represent the right- and left-circularly polarised waves. To find the solution to equation 2.4, we substitute the right- and left- circularly polarised electric field components of the EMW, $E_{\pm} = E_0 e^{i(k_{\pm} z - \omega t)}$, with a real amplitude E_0 and angular frequency of ω . This gives us the harmonic solution of $r_{\pm} = r_0 e^{i(k_{\pm} z - \omega t)}$, where r_0 is a general complex number. If we substitute this r_{\pm} into

equation 2.4 we find that r_{\pm} and E_{\pm} have the following relation:

$$r_{\pm} = \frac{-\frac{e}{m_e}}{-\omega^2 \mp \frac{e}{m_e} B \omega} E_{\pm}. \quad (2.5)$$

Since r_{\pm} has an exponential relation with ω , $\dot{r}_{\pm} = -i\omega r_{\pm}$. Therefore, using the equation for current ($\mathbf{J} = -n_e e \mathbf{r}$) we get:

$$J_{\pm} = i \frac{n_e e^2}{m_e (\omega \pm \frac{e}{m_e} B)} E_{\pm}. \quad (2.6)$$

This, combined with $\mathbf{J} = \sigma \mathbf{E}$, where σ is the conductivity of the region, results in

$$\sigma_{\pm} = i \frac{n_e^2}{m_e (\omega \pm \frac{e}{m_e} B)}. \quad (2.7)$$

If we consider the dispersion relation¹ obtained in Chapter 2 of Wilson et al. (2013, equation 2.63):

$$k^2 = \frac{\mu \epsilon \omega^2}{c^2} \left(1 + i \frac{4\pi\sigma}{\omega\epsilon}\right), \quad (2.8)$$

by substituting 2.7 into 2.8, we obtain:

$$k_{\pm}^2 = \frac{\omega^2}{c^2} \left(1 - \frac{\omega_p^2}{\omega(\omega \pm \omega_c)}\right), \quad (2.9)$$

where ω_p is the plasma frequency ($\omega_p = \sqrt{\frac{n_e e^2}{m_e \epsilon}}$) and ω_c is the cyclotron frequency ($\omega_c = \frac{e}{m_e} B$).

The relation $k = \frac{\omega}{c} n$ gives us the refraction index:

$$n_{\pm}^2 = 1 - \frac{\omega_p^2}{\omega(\omega \pm \omega_c)}, \quad (2.10)$$

for two oppositely-handed EMWs. This causes the left- and right- handed components of a linearly polarised EMW to have different phase velocities. Therefore, after they travel a

¹A dispersion relation relates the wavenumber to the angular frequency of the wave.

distance of Δz in a classical treatment of the problem in Wilson et al. (2013), the phase-shift can be found by $2\Delta\Psi = (k_+ - k_-)\Delta z$. For $\omega \gg \omega_p$ and $\omega \gg \omega_c$ we obtain

$$\Delta\Psi = \lambda^2 \frac{e^3}{8\pi^2\epsilon_0 m_e^2 c^3} \int n_e B_{\parallel} dl. \quad (2.11)$$

In this approach we initially assumed that the magnetic field is in the z-direction (the direction of propagation). If we take the more general form, it can be shown that:

$$\Delta\Psi [rad] = 0.812 \int n_e [cm^{-3}] \mathbf{B} [\mu G] \cdot d\mathbf{l} [pc]. \quad (2.12)$$

This equation assumes a quasi-longitudinal approximation, meaning that the magnetic field is roughly along the line of propagation. In this case, the earlier-mentioned criteria for ω , in this more general form, will be $\omega \gg \omega_p$ and $\omega \gg \omega_c \sec \theta$, where θ is the angle between the wave propagation direction \mathbf{k} and the magnetic field direction (e.g., Hutchinson 1987). Luckily, in the ISM, this approximation is valid up to about 89.9 degrees (i.e., generally all the time; Brown 2002). Brown (2002) provides a detailed step-by-step approach to get to equation 2.12 from equation 2.10. A full quantum mechanical derivation of Faraday rotation produces the same result (e.g., Berman 2010).

For our purposes, we use radio galaxies, quasars, and pulsars as the background sources of linearly polarised EMW. These galaxies and quasars contain very energetic objects, such as supermassive black holes producing Active Galactic Nuclei (AGN)². The fainter background sources are identified as low luminosity AGNs and star-forming galaxies. These galaxies and quasars produce synchrotron emission.

Synchrotron emission is continuum electromagnetic radiation produced when the charged ultra-relativistic particles are deflected in the presence of magnetic fields. A source with Synchrotron radiation can be at most 70% linearly polarised (Pacholczyk 1970; Rybicki and Lightman 1986). As this linearly polarised EMW passes through the ISM in our galaxy, it

²The center of a galaxy which produces much higher luminosity is referred to as AGN.

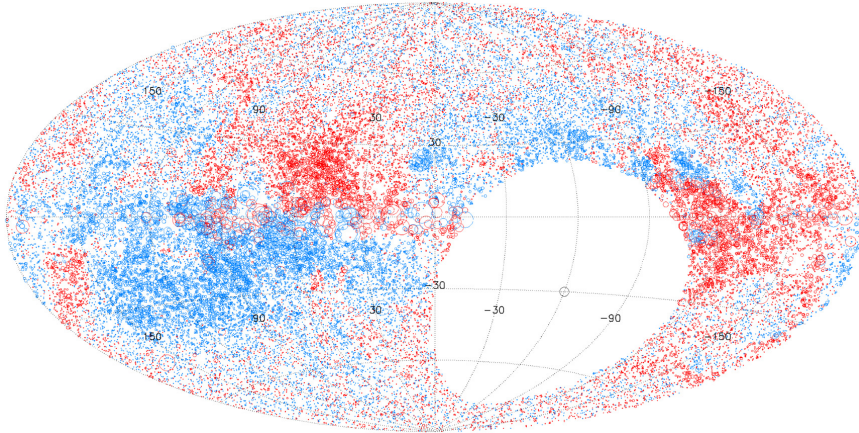


Figure 2.2: Taylor et al. (2009) Rotation Measure catalog. The data points consist of 37,543 RM values over the north sky. Red (blue) circles show positive (negative) RM and the size of the circle show the strength of RM.

will undergo Faraday rotation, where there is sufficient number of free electrons with an embedded magnetic field. Various RM catalogs of background sources are available (e.g., Broten et al. 1988; Brown et al. 2003, 2007; Taylor et al. 2009; Van Eck et al. 2011). For this thesis work, I use the Taylor et al. (2009) catalog, which is shown in Figure 2.2.

To calculate the rotation measure values of compact background sources, the linear relation between λ^2 and the change in polarisation angle in equation 2.1 is used (e.g., Brown et al. 2008). At each observed wavelength the polarisation angle is measured and the slope of the linear fit of polarisation angles vs λ^2 's provides the RM. Therefore, observations at multiple wavelengths are necessary to obtain a RM value. Figure 2.3 shows examples of these RM calculations. The right panel in Figure 2.3 is from Brown and Taylor (2001) where the RM values are obtained using the Synthesis Telescope at the Dominion Radio Astrophysical Observatory (DRAO)³, in Penticton, British Columbia, Canada. The left panel is from Van Eck et al. (2011), where the observations were done by the Very Large Array (VLA)⁴ in central New Mexico. In both panels the x-axis shows the wavelength squared, and the y-axis shows the observed polarisation angles.

The measured RM, along with estimates of the electron density distribution, can be used

³<https://www.nrc-cnrc.gc.ca/eng/solutions/facilities/drao.html>

⁴<https://public.nrao.edu/telescopes/vla/>

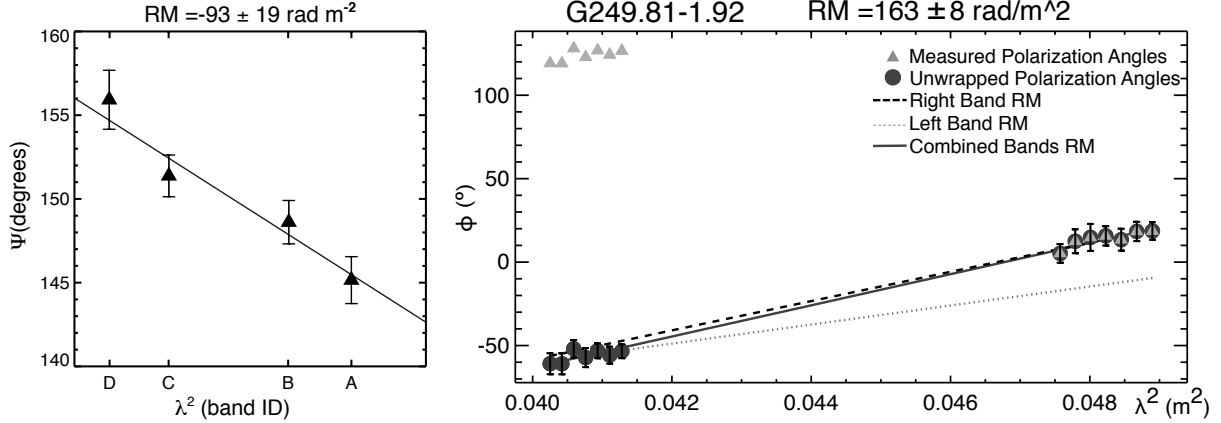


Figure 2.3: Finding RM produced by the ISM on the linearly polarised EMW from background sources. The slope of the linear relationship between polarisation angle and λ^2 provides the RM. The right panel is from Brown and Taylor (2001), and the left panel is from Van Eck et al. (2011). In each of the panels x-axis shows the squared wavelengths of the observed EMW, and the y-axis shows the observed polarisation angles.

to infer information about the Galactic magnetic field. Figure 2.4 illustrates an example of these studies with a sketch of the resulting topography of the Galactic magnetic field. Faraday rotation measurements have also been used to investigate the magnetic field of diffuse low-extinction filaments (Stil and Hryhoriw 2016) as well as magnetic fields in large Galactic HII regions, such as one close to the California Molecular Cloud (CMC; Harvey-Smith et al. 2011).

Faraday rotation, however, has not been commonly used to observe the magnetic fields in molecular clouds. One of the main reasons for this was the belief that molecular clouds are primarily neutral and so could not possibly induce significant Faraday rotation. Nevertheless, there have been a handful of attempts to study magnetic fields in high-extinction MCs using Faraday rotation (Wolleben and Reich 2004a; Reich et al. 2002; Wolleben and Reich 2004b; Yusef-Zadeh et al. 1997). For example, Wolleben and Reich (2004a) utilise the concept of a Faraday screen - an object that can change the polarisation angle and intensity of the polarised background - to estimate the field strength within the region. However, their method relies on an imprecise estimate of the distance to the screen, uncertainty in the electron density and, likely, an oversimplification of the shape of the screen itself. In Chapter 3, however, I will

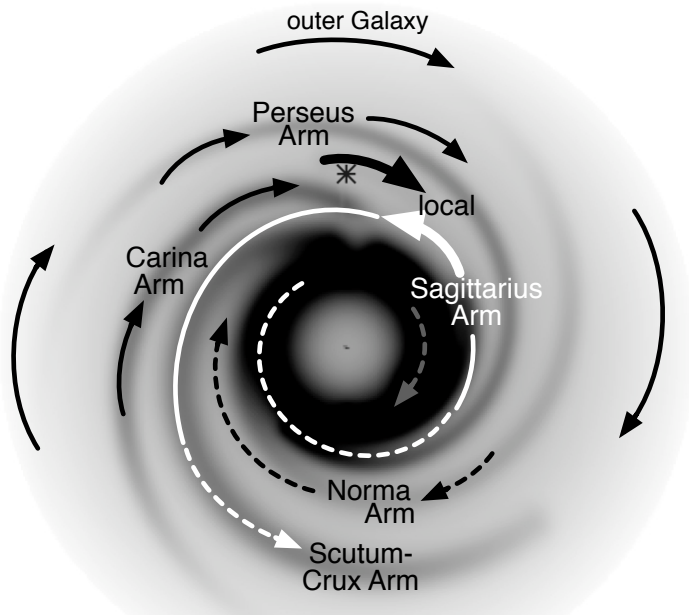


Figure 2.4: A sketch of the resulting topography of the Galactic magnetic field in the disk of the Galaxy based on a study using rotation measures of compact sources. The model combined rotation measures from extragalactic sources and pulsars, and utilised the electron density model of Cordes and Lazio (2001). The skinny arrows show the field directions as determined from the study of Van Eck et al. (2011) combined with those from previous work (bold arrows). The dashed arrows indicate magnetic field directions that are uncertain. (Figure 11 from Van Eck et al. (2011))

introduce a *new* method to utilise Faraday rotation to measure the line-of-sight component of the magnetic field associated with filamentary molecular clouds.

2.2 Dust Polarisation Detection

The first observations of magnetic fields in the ISM, as discussed in Chapter 1, started with the detection of ISM dust polarisation. Andersson (2015) provides a detailed review of this technique and its history.

The main assumption in this technique is that dust grains in the ISM align their long axis perpendicular to the magnetic fields. As a consequence, these particles' thermal radiation will be polarised perpendicular to the magnetic field of the region. These dust grains can also polarise the EMW from background stars, as explained by Mie's theory of scattering (Lock and Gouesbet 2009). By measuring the polarised radiation from the starlight and the dust grains themselves, we can map the magnetic field in the plane of the sky (B_{Pos}).

Surveys done by Planck⁵, BLASTPol⁶, James Clerk Maxwell Telescope BISTRO⁷, and CARMA⁸, among others, have provided dust polarisation observations in different star-forming regions and at different scales: from giant molecular clouds to small star-forming cores (Planck Collaboration et al. 2016; Fissel et al. 2016; Pattle et al. 2018; Hull and Plambeck 2015). The dust polarisation technique has been widely used to map magnetic fields in MCs and GMCs particularly, in recent years by the Planck Space Observatory. Figure 2.5 shows the plane-of-sky component of the magnetic field in the Orion region obtained by Planck.

⁵<https://pla.esac.esa.int>

⁶<https://sites.northwestern.edu/blast/>

⁷https://www.eaobservatory.org/jcmt/science/large-programs/gb_bfields/

⁸<https://www.mmaray.org/>

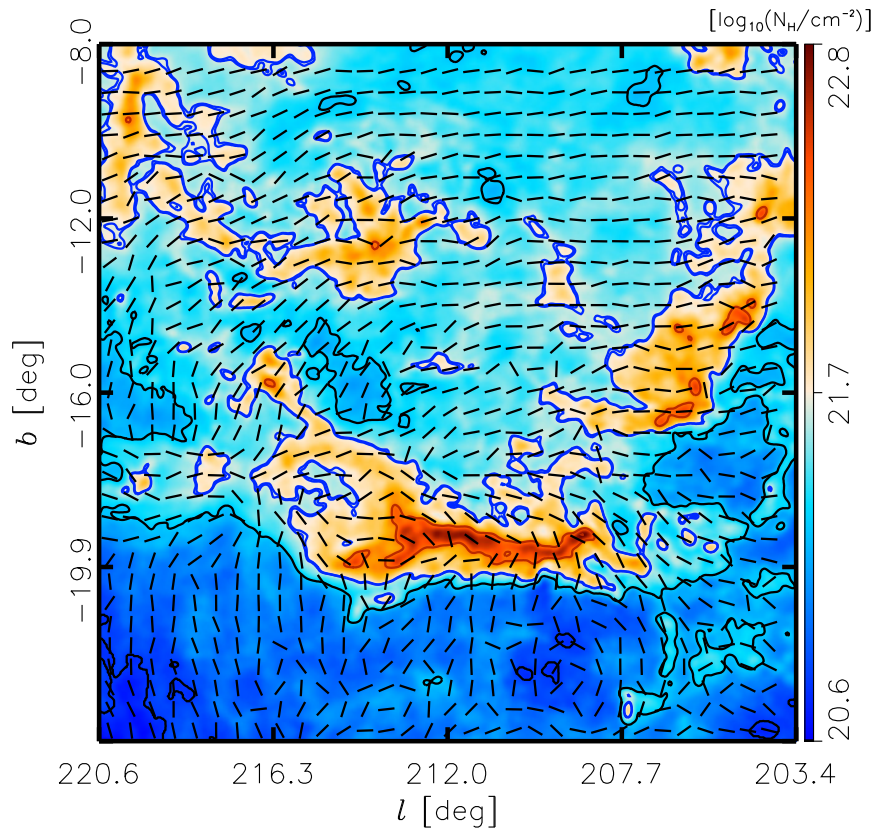


Figure 2.5: The plane-of-sky component of the magnetic field in the entire Orion region, observed by the Planck Observatory. The x- and y-axes indicate the galactic and latitude of the region in the Galactic coordinate system. The color coding shows the column density of the region, with red and yellow illustrating higher column density and blue indicating a lower column density. The lines show the magnetic field orientation in the plane of the sky. The region includes both the Orion A and Orion B MCs. (Figure 5 from Planck Collaboration et al. (2016))

2.3 Zeeman Measurements

The dust polarisation technique only provides the orientation of the plane-of-sky component of magnetic fields (B_{POS}) and not their line-of-sight (B_{LOS}) component. To obtain the B_{LOS} component in MCs and GMCs Zeeman measurements can be used.

In the presence of magnetic fields a spectral line will be split into several lines. This phenomenon is known as the Zeeman effect or Zeeman splitting. The quantum mechanical derivation of the Zeeman effect is provided in a number of texts (e.g Hentschel 2009). A beautiful, though inaccurate⁹, classical analysis of Zeeman splitting and how the direction of magnetic fields are found using Zeeman observations is given in Clarke (2010). Robishaw (2008) provides a thorough review of the history of Zeeman measurements in the ISM and in solar physics.

Zeeman measurements in the ISM began in 1957 when Bolton and Wild (1957) suggested that observations of 21-cm Zeeman splitting caused by the ISM magnetic fields could be possible. This suggestion was based on Zeeman observations of weak solar magnetic fields by Babcock (1953). Using the hypothesis of Bolton and Wild (1957), Davies (1963) provided Zeeman measurements of a few interstellar clouds (namely, in the Orion and Perseus arms). Verschuur (1967) employed the 21-cm Zeeman measurement to detect the magnetic field strength in Tau A and Cas A within the Taurus and Orion regions, respectively.

As a consequence of relatively weak magnetic fields seen in MCs (e.g., 10s of μG), the splitting happens with very small frequency differences between the right and left circularly polarised components (Troland and Heiles 1982), and even with very high sensitivity observations, the frequency difference can still be masked in the noise (Killeen et al. 1992). Given the need for extremely high sensitivity observations, Zeeman measurements are also very time consuming (Crutcher and Troland 2008), requiring long telescope integration times in regions with relatively small magnetic fields (Robishaw 2008). Thus, even though Zeeman measurements provide B_{LOS} , there are not enough Zeeman measurements of MCs and GMCs

⁹It is inaccurate because it explains a quantum mechanical phenomenon via a classical treatment.

available to study the magnetic field of filamentary MCs over large scales.

2.4 Theoretical Studies of Magnetic Fields

Theoretical studies of magnetic fields in the ISM can be done by MHD simulations, based on *fluid* theory and Maxwell's equations. The study of a fluid without considering magnetic fields is called HydroDynamics (HD); when we include magnetic fields this is known as MagnetoHydroDynamics.

We see MHD or HD processes in our daily lives, such as in the motions of clouds in the blue sky, or the flow of water from a mountain, as shown in Figure 2.6. To study the fluid, one can consider each single particle, atom, or molecule in their pair-wise interactions with other particles in the fluid. However, this is extremely time-consuming and not necessary to model the system. Instead we can assume that the system is composed of *fluid elements*, also referred as fluid parcels.

A critical concept when discussing a fluid is the mean free path. A particle's mean free path is the average distance that the particle travels before colliding with another particle. Therefore, a mean free path is related to the collisional rate or the collisional cross section of particles. The ISM (a gas or plasma, in general) may be considered fluid if the collisional mean free path between particles is much smaller than the characteristics length- and time-scales of the system (the scale in which the system quantities such as pressure and temperature change noticeably).

Fluid elements, which contain many individual particles of the system, are much larger than the mean free path of the individual particles and are much smaller than the characteristic scale of the overall system. Therefore, each fluid element is in thermodynamic equilibrium (i.e. the particles have a Maxwell-Gibbs velocity distribution; Kunz 2019). A typical particle mean free path for the ISM or a molecular cloud is around 10^{-7} pc (Ryden et al. 2010; Mo et al. 2010; Kunz 2016). This mean free path is much smaller than the characteristics large-scale



Figure 2.6: Examples of HD in nature. Motion of the clouds in the blue sky or a waterfall are examples of HD illustration in nature.

gradients in the ISM or a molecular cloud.

We can then use the usual laws of physics to describe these fluid elements, rather than the individual particles. As a first step, we can write the conservation of mass for the fluid and fluid elements. Conservation of mass for the fluid elements is described by the continuity equation:

$$\frac{\partial \rho}{\partial t} + \nabla \cdot (\rho \mathbf{v}) = 0, \quad (2.13)$$

where ρ is the mass density of the fluid, t is time, and \mathbf{v} is the bulk velocity of the fluid elements (Kulsrud 2005).

In addition to the mass conservation, since the system can contain charged particles, we need to consider conservation of charge, or the charge continuity equation:

$$\frac{\partial \rho_{\text{charge}}}{\partial t} + \nabla \cdot (\rho_{\text{charge}} \mathbf{v}) = 0, \quad (2.14)$$

where ρ_{charge} the charge volume density and $\rho_{\text{charge}}\mathbf{v}$ is the current density per unit area (\mathbf{J}).

Next, we take the conservation of momentum, which equates the changes of momentum to the net forces in the system.

$$\frac{\partial(\rho\mathbf{v})}{\partial t} + \nabla \cdot (\rho\mathbf{v}\mathbf{v}) = -\nabla P + f, \quad (2.15)$$

where P is the pressure, and f describes other forces in the system per unit volume. In order to describe a fluid fully, we also need the conservation of energy equation. The adiabatic energy conservation is given by

$$\frac{d}{dt}\left(\frac{P}{\rho^\gamma}\right) = 0 \quad (2.16)$$

where γ is the ratio of specific heats C_P/C_V (Kulsrud 2005).

2.4.1 MagnetoHydroDynamics (MHD) Equations

In the presence of magnetic fields and when a fluid contains charged particles we consider MHD equations instead of only pure HD equations to describe the system. In this thesis, I only talk about single fluid ideal MHD, where the fluid elements are of only one type and that the resistivity of the system can be neglected (Freidberg 2014). To expand the HD equations to MHD we need to consider Maxwell's equations:

$$\begin{aligned} \nabla \cdot \mathbf{E} &= \frac{4\pi\rho_{\text{charge}}}{\epsilon} && \text{(Gauss's Law)} \\ \nabla \times \mathbf{E} &= -\frac{1}{c} \frac{\partial \mathbf{B}}{\partial t} && \text{(Faraday's Law)} \\ \nabla \times \mathbf{B} &= \frac{4\pi\mu}{c} \mathbf{J} + \frac{1}{c} \frac{\partial \mathbf{E}}{\partial t} && \text{(Ampere's Law)} \\ \nabla \cdot \mathbf{B} &= 0 && \text{(no magnetic monopole),} \end{aligned} \quad (2.17)$$

where \mathbf{E} is the electric field in the system, \mathbf{B} is the magnetic field, ϵ is the permittivity, μ is the magnetic permeability, \mathbf{J} is the current density per unit area, and ρ_{charge} is the volume charge density of the system. We assume ρ_{charge} is approximately zero, meaning that each

fluid element and the entire fluid are quasi-neutral.

To include magnetic fields and gravity in an astrophysical context we can rewrite the momentum equation in form of:

$$\frac{\partial(\rho\mathbf{v})}{\partial t} + \nabla \cdot (\rho\mathbf{v}\mathbf{v}) = -\nabla P - \rho\nabla\Phi - \frac{1}{8\pi}\nabla B^2 + \frac{1}{4\pi}\mathbf{B} \cdot \nabla\mathbf{B}, \quad (2.18)$$

where Φ is the gravitational potential given by:

$$\nabla^2\Phi = 4\pi G\rho, \quad (2.19)$$

where G is the gravitational constant and ∇^2 is the Laplacian operator.

Furthermore, Maxwell's equations will yield the induction equation:

$$\frac{\partial\mathbf{B}}{\partial t} = \nabla \times (\mathbf{v} \times \mathbf{B}), \quad (2.20)$$

where \mathbf{B} is the magnetic field and \mathbf{v} is the fluid bulk velocity. When considering these equations, we still need to satisfy the requirement of a divergence-free magnetic field (i.e. no magnetic monopoles as stated in equation 2.17).

Equations 2.13, 2.16, 2.18, 2.20, along with equation 2.19 and divergence-free magnetic fields represent the MHD equations. As a final note, we need to keep in mind that MHD is a series of approximations to describe a system without the burden of considering all the pair-wise interactions. For this purpose we follow fluid elements, which themselves contain many particles.

When we derive the MHD equations for our systems, we are aware of the presence of these particles in the fluid system and the fact that they are charged. However, after we derive our equations for a fluid in MHD, we ignore the details pertaining these smaller particles. All we care about is that our system is composed of fluid elements and that it follows our derived equations to the accuracy in which we are interested. We need to only remember

that the fluid is quasi-neutral and can respond to magnetic or electric fields as described by the MHD equations, without needing to account for the properties of the individual particles within the fluid elements. Therefore, it is of paramount importance to examine the free parameters in each system to make sure that the system can be correctly modeled by our MHD equations, if not, the equations need to be modified appropriately. In Chapter 5, I will employ these concepts to model the magnetic field structure in rotating and collapsing filamentary molecular clouds using the FLASH MHD code.

Chapter 3

A New Method to Measure Magnetic Fields Strengths Associated with Filamentary Molecular Clouds

The contents of this chapter have been previously published as:

Tahani, M., Plume, R., Brown, J. C., & Kainulainen, J. (2018), ‘Helical Magnetic Fields in Molecular Clouds? A New Method to Determine the Line-of-Sight Magnetic Field Structure in Molecular Clouds’, *A&A*, 614, 100

In this chapter, I propose a new method to find B_{LOS} in MCs based on Faraday rotation measurements. I test this method in four relatively nearby MCs: the Orion Molecular Cloud A (OMC-A; the entire southern complex), the Orion Molecular Cloud B (OMC-B; the entire northern complex), the Perseus Molecular Cloud (PMC), and the California Molecular Cloud (CMC) and find good agreement with available Zeeman measurements. I find that the magnetic field morphology in Orion A and California are consistent with a helical or a bow-shape magnetic field.

3.1 Previous Work and Assumptions

Previous attempts to study magnetic fields in high-extinction MCs using Faraday rotation have been performed by a number of authors (Wolleben and Reich 2004*a*; Reich et al. 2002; Wolleben and Reich 2004*b*; Yusef-Zadeh et al. 1997). For example, Wolleben and Reich (2004*a*) utilise the concept of a Faraday screen - an object that can change the polarisation angle and intensity of the polarised background - to estimate the field strength within the region. However, their method relies on an imprecise estimate of the distance to the screen, uncertainty in the electron density, and likely an oversimplification of the shape of the screen itself.

To estimate magnetic fields in MCs, I use a slightly different approach that avoids these difficulties by using extinction maps to obtain the total column density, and a chemical evolution code to determine more reasonable estimates of the electron density within MCs. By combining these with Faraday rotation measurements, I can work backwards to determine what the magnetic field must be in these regions.

3.1.1 Free Electrons in MCs

Free electrons are necessary for Faraday rotation to occur. The photodissociation region (PDR) models (Hollenbach and Tielens 1999, 1995, 1997) predict the existence of free electrons even in dense regions of MCs, and observations support the existence of free electrons in these regions (Harrison et al. 2013; Flower et al. 2007).

Most of the ISM is not illuminated by strong UV fields and this fact had led to the belief that in high column density regions in typical MCs, the UV field is so strongly attenuated that free electrons should be rare. Therefore Faraday rotation was not expected to occur within MCs.

Cosmic rays (CR), however, are known to be an important source of ionization in both diffuse and dense MCs (Bergin et al. 1999; Williams et al. 1998; Padovani and Galli 2013;

Padovani et al. 2009; Everett and Zweibel 2011; Morlino and Gabici 2015; Bergin et al. 1995; Willacy and Williams 1993; Hasegawa and Herbst 1993) and thus CR ionization is an important source of free electrons in MCs. Calculating the CR ionizing factor, ζ , is not straightforward and this factor may not be constant throughout the entire cloud (Padovani et al. 2016; Padovani and Galli 2013). However, for the resolution and the scales that we are interested in, I assume it to be constant¹. With the confirmed existence of free electrons in MCs, we can expect that Faraday rotation occurs in MCs, as well as in the rest of the ISM.

3.2 Data

My method uses RMs of extragalactic sources with lines of sight passing near and through individual MCs to extract the strength and direction of magnetic fields in environments local to these MCs. Below I describe the RM data and the extinction maps that I use in this method.

3.2.1 Rotation Measure Catalog

I use the RM values from the Taylor et al. (2009, hereafter TSS09) catalog, mentioned in Chapter 2. They obtain RMs for 37543 polarised radio sources by reanalyzing the NRAO VLA Sky Survey data (NVSS; Condon et al. 1998). For the regions of interest, within my specifically defined boundaries, TSS09 has 50 RMs within the OMC-A, 16 in OMC-B, 35 in PMC, and 43 in CMC. Figure 3.1 shows the map of RM data points in the PMC and CMC, and Figure 3.2 shows the map of RM data points in OMC-A and OMC-B. The diameter of the RM circles is proportional to the magnitude of the RM; blue (red) circles indicate positive (negative) RMs, where the average line-of-sight magnetic field is directed towards (away from) us. The background color image represents the visual extinction map (see section 3.2.2), with brighter or green color showing greater extinction.

¹See Everett and Zweibel (2011) for a history of theoretical studies of CR penetration into MCs.

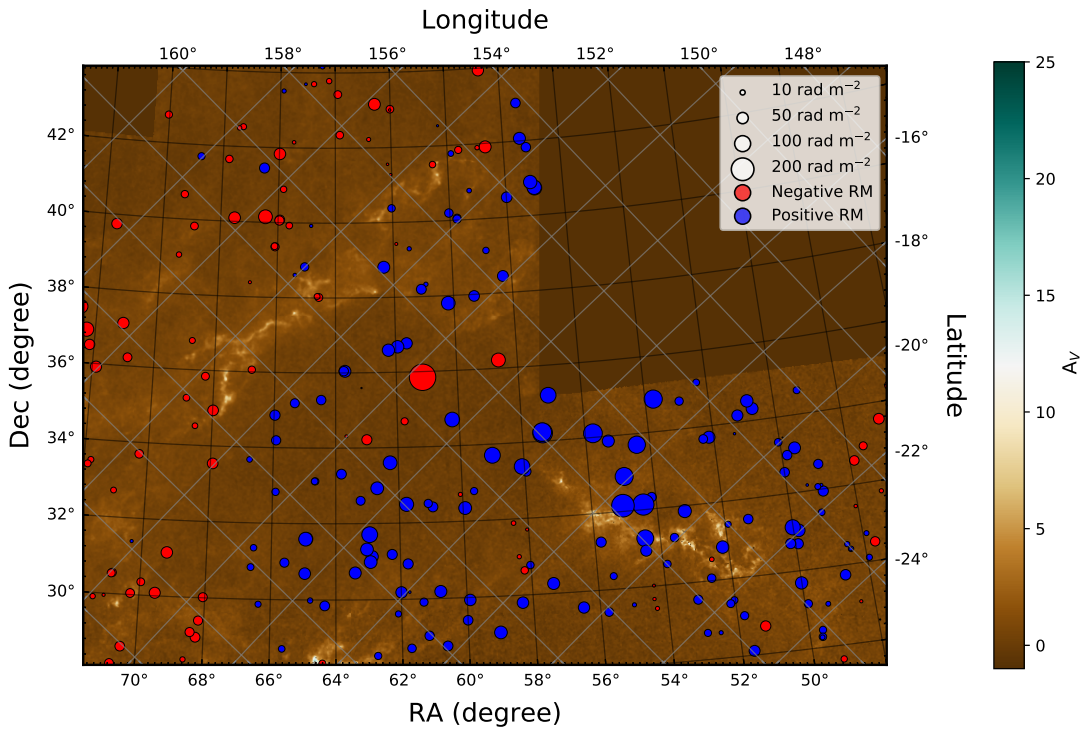


Figure 3.1: RM values from the catalog of TSS09 mapped on the extinction map of CMC and PMC. Blue (red) circles indicate positive (negative) RM values. The size of the circles is proportional to the magnitude of the RM. The gray grid provides galactic coordinates, whereas the black grid provides equatorial coordinates. Color image shows the extinction map (A_V) in units of magnitudes of visual extinction provided by KBHP09.

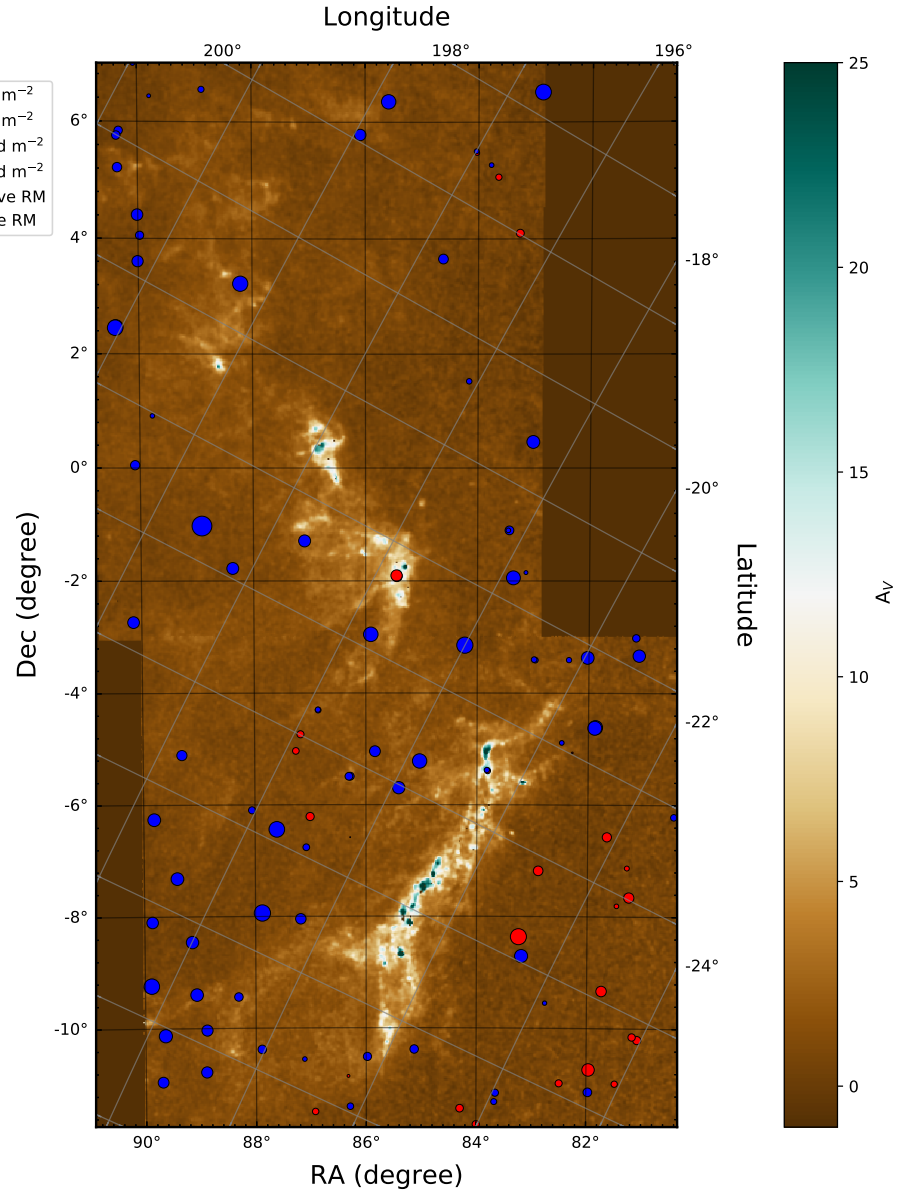


Figure 3.2: RM values from the catalog of TSS09 mapped on the extinction map of Orion. OMC-A is the complex to the south and OMC-B is the complex to the north. Blue (red) circles indicate positive (negative) RM values. The size of the circles is proportional to the magnitude of the RM. The gray grid provides galactic coordinates, whereas the black grid provides equatorial coordinates. Color image shows the extinction map (A_V) in units of magnitudes of visual extinction provided by KBHP09.

3.2.2 Extinction Map

To map the hydrogen ($\text{HI} + \text{H}_2$) column density of each MC, I use visual extinction maps (in units of magnitude of visual extinction or A_V) provided by Kainulainen et al. (2009, hereafter KBHP09). They obtained near-infrared dust extinction maps using the 2MASS data archive and the NICEST (Lombardi 2009) color excess mapping technique. These maps have been produced with a physical resolution of 0.1 pc, which is the Jeans length for a core at $T = 15\text{ K}$ and mean particle density of $\bar{n} = 5 \times 10^4 \text{ cm}^{-3}$. The Jeans length is the length at which gravity starts to dominate an isothermal cloud, or alternatively, the expected scale on which the cloud is fragmenting. It is given by the equation:

$$\lambda_J = \sqrt{\frac{\pi c_s^2}{G\rho}}, \quad (3.1)$$

where c_s is the sound speed, G is the gravitational constant, and ρ is the volume density of the region. I use these extinction maps as a proxy for $N_{\text{HI+H}_2}$ (as well as for obtaining electron abundances), by applying the Bohlin et al. (1977) conversion factor.

3.3 Methodology

The RMs in TSS09 are the result of polarised radiation passing through the entire line-of-sight of the Galaxy, from the source to the receiver (on Earth). Since I wish to recover the component of the RM that is produced by only the MC, I need to decouple the Faraday rotation produced by the Galaxy from that produced within the MC itself.

To accomplish this, I divide the integral in equation 2.1 into two parts: the contribution from the MC (RM_{MC}) and the contribution from everything else along the line of sight (Galactic contribution, RM_{Gal}). The Galactic contribution to the RM can be estimated by using RMs from positions that fall near the MC but are far enough away that they are clearly

not affiliated with it. I refer to these as OFF positions and designate their rotation measures as RM_{OFF} .

RM_{ON} refers to any rotation measure in the TSS09 catalog that lies directly on or very near the MC (see Figure 3.3). Since the angular separation between any RM_{OFF} and RM_{ON} is small compared to the angular size of the Galaxy, I assume that RM_{ON} and RM_{OFF} are essentially sampling the same path length through the Galaxy.

We can then write RM_{ON} as:

$$\text{RM}_{\text{ON}} = \text{RM}_{\text{MC}} + \text{RM}_{\text{Gal}}. \quad (3.2)$$

Comparing RM_{OFF} with RM_{Gal} in Figure 3.3 shows that the path length of RM_{OFF} is larger than that of RM_{Gal} by a value equal to the path length through the cloud (i.e., a cloud-sized patch of the ISM, which I denote as $\text{RM}_{\text{cloud-sized ISM}}$). In theory, I should account for this by subtracting the effects of this patch of the ISM from RM_{OFF} . I could do this by assuming that $\text{RM}_{\text{cloud-sized ISM}}$ corresponds to a region with the same size as the MC but with the characteristics of the general ISM. However, I suggest that for dense clouds (MCs), $\text{RM}_{\text{cloud-sized ISM}}$ is negligible compared to RM_{MC} . To compare these two RMs, I examine the average values of n_e and \mathbf{B} of a typical MC with those of general ISM.

Average electron abundances for a typical MC, with density of around $\bar{n} = 10^3 \text{ cm}^{-3}$, is roughly $10^{-4}\text{-}10^{-5}$ (Harrison et al. 2013). The multiplication of these two yields electron densities of $10^{-1}\text{-}10^{-2} \text{ cm}^{-3}$. The average density of the general ISM is $\bar{n} = 1 \text{ cm}^{-3}$ (McKee and Ostriker 2007), with an average electron abundance of $\simeq 10^{-2}$ (Cox 2005), which together provide an average electron density of 10^{-2} cm^{-3} . Thus, the average electron density of MCs can be between one and ten times that of the general ISM. The magnetic field strengths within MCs are often at least ten times higher than that of the general ISM (Planck Collaboration et al. 2016). Therefore, the contribution of the MC to the RM along the “ON” line-of-sight will be roughly 100 times larger than the ISM contribution of a similar size patch. Thus,

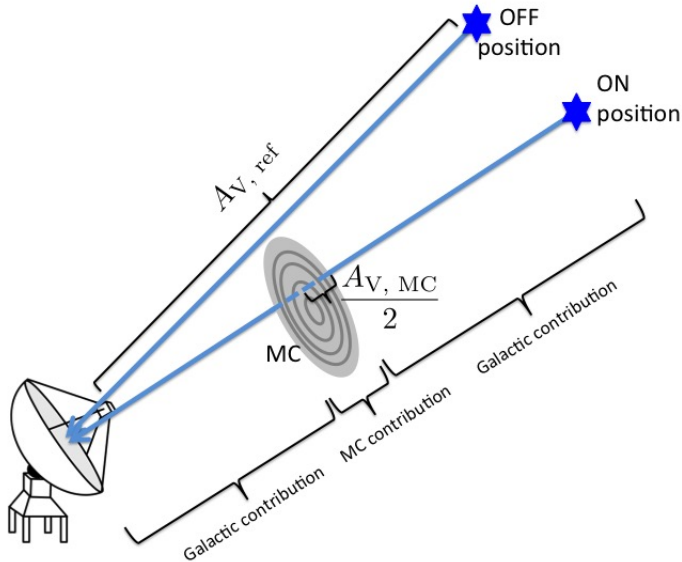


Figure 3.3: Schematic illustrating “ON” and “OFF” RM positions, relative to an MC. To find the magnetic field in the MC, I need to disentangle the RM produced by the Galaxy from that produced by the MC itself. I do so by subtracting the RM of a nearby point, called the OFF position, from the ON position which has an RM produced by both the MC (MC contribution) and the Galaxy (Galactic contribution). See section 3.3.1 for details. Additionally, I need to consider the effects of all the layers of the MC from the exterior to the center of the cloud to reach to extinction value of $A_{V, MC} = A_V - A_{V, ref}$. However, since the cloud is symmetrical along the line-of-sight, and is illuminated from both sides by an ambient UV field, I assume the center of the cloud has an extinction of $\frac{A_{V, MC}}{2}$ magnitudes.

for simplicity, I neglect the effect of the RM_{cloud-sized ISM}, and assume RM_{OFF} is equal to RM_{Gal}. I note, however, that this assumption may not be valid for all Galactic clouds and, in particular, in diffuse clouds RM_{cloud-sized ISM} may have to be specifically included.

I can therefore obtain the RM produced by the MC alone by subtracting the OFF position from the ON position, that is,

$$\text{RM}_{\text{ON}} - \text{RM}_{\text{OFF}} = \text{RM}_{\text{MC}} = \left(0.812 \int n_e B_{\text{LOS}} dl \right)_{\text{MC}}, \quad (3.3)$$

where I have replaced the dot product by using the line-of-sight (LOS) component of the magnetic field within the MC (B_{LOS}). Furthermore, if we assume the magnetic field through the MC is uniform, we can extract B_{LOS} from the integral

$$\text{RM}_{\text{MC}} = \left(0.812 B_{\text{LOS}} \int n_e dl \right)_{\text{MC}}. \quad (3.4)$$

Since $\int n_e dl$ is the electron column density in the MC, N_e , we can then write:

$$\text{RM}_{\text{MC}} = \left(0.812 B_{\text{LOS}} N_e \right)_{\text{MC}}. \quad (3.5)$$

Accordingly we can obtain

$$(B_{\text{LOS}})_{\text{MC}} = \frac{\text{RM}_{\text{MC}}}{0.812 N_e}. \quad (3.6)$$

To find B_{LOS} in the MC I need to determine reasonable values for RM_{OFF} and the electron column density (N_e), for each observed point. This is discussed below.

3.3.1 Estimating RM_{OFF} and RM_{ref}

I need to find suitable ON and OFF positions such that, when the RMs are subtracted, they isolate the effect of the MC alone. To find the ON positions, I search for RM measurements that visually fall on the MCs of interest (i.e., in higher-column-density regions). To find the

OFF positions I hand pick a number of RMs that have low column densities (i.e., $A_V < 1$) and are also far enough away from the cloud that they are clearly not directly related to it. Therefore, in terms of A_V and position, the OFF positions are associated with the general Galactic background rather than with the MC of interest.

Since variable Galactic structure can produce different RM values in different OFF positions, I use a number (N) of OFF positions to determine an “average” OFF position, which I call RM_{ref} , that is,

$$RM_{ref} = \sum_{i=1}^N \frac{RM_{OFF, i}}{N}. \quad (3.7)$$

While I could use all of the positions in my maps that obey the above criteria to produce RM_{ref} , I also wish to examine the magnetic field in the lower column density gas that immediately surrounds the MCs. Therefore, I develop a method to determine the optimal number of OFF positions to incorporate into RM_{ref} . This ensures that I have a robust and useful value for RM_{ref} as well as leaving me enough RMs at the lower column density cloud edges to incorporate into my B field analysis.

For this purpose, I investigate how the derived magnetic field strength and direction change as I increase the number of OFF positions from 1 to N . I find that, with few OFF positions, there is a large variance in the strength and direction of the derived magnetic fields. However, as I continue to increase the number of OFF positions, the variations decrease and the B field strengths and directions stabilise to a constant value (see Figure 3.4). I choose the optimal number of OFF positions as the point at which the variance is minimised.

From this analysis, I find the optimal number of reference points to be 12 for OMC-A, 5 for OMC-B, 8 for CMC, and 11 for PMC. The resultant values of RM_{ref} are 1.4 rad m^{-2} for OMC-A, 32.3 rad m^{-2} for OMC-B, 4.0 rad m^{-2} for CMC, and 31.1 rad m^{-2} for PMC. Using the “reference” positions in lieu of a single OFF position, equation 3.6 becomes:

$$(B_{LOS})_{MC} = \frac{RM_{ON} - RM_{ref}}{0.812N_e}. \quad (3.8)$$

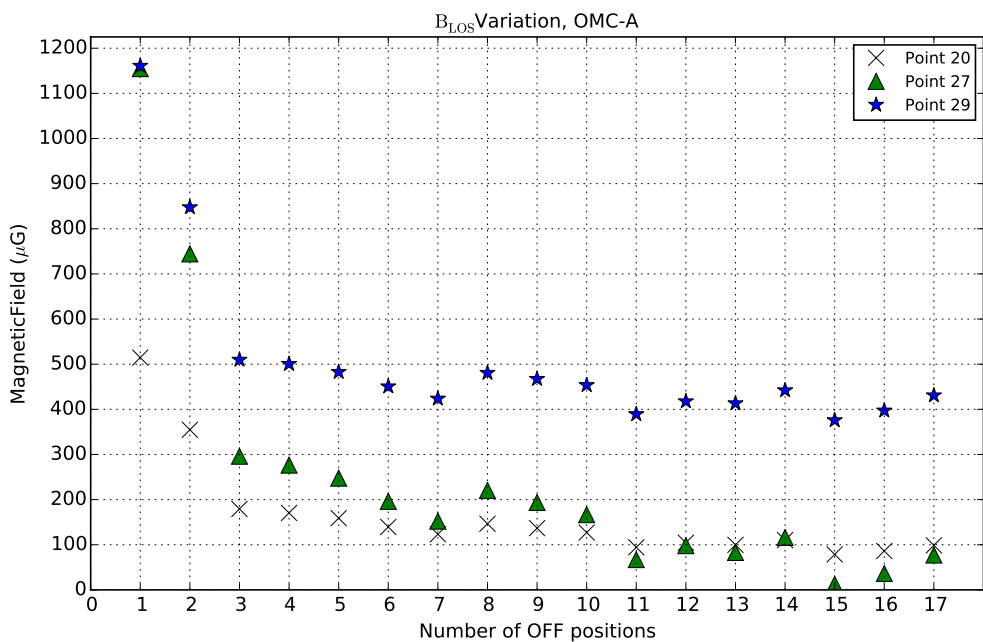


Figure 3.4: Magnetic field values in OMC-A using different numbers of OFF positions to calculate the “reference” value (RM_{ref}). Results are presented for three different points in OMC-A. The x-axis indicates the number of OFF positions used in RM_{ref} . The y-axis shows the calculated magnetic field value. As discussed in the text, the magnetic field stabilises at roughly 12 OFF positions.

3.3.2 Obtaining the Electron Column Densities

Determining the electron column density (N_e) in MCs requires an assessment of the total column density ($N(HI + H_2)$) through the MC, as well as a determination of the electron abundance as a fraction of total column density (X_e). The former can be estimated from the KBHP09 extinction maps and the latter from a chemical model. These steps will be outlined below.

Determining Total Column Density From the Extinction Maps

The KBHP09 maps are created by interpolating the measured extinction values onto a regular grid with a physical spacing of 0.1 pc between points. This corresponds to a different angular separation between points for different clouds due to their distances. The RM measurements are not always at one of the precise positions where A_V is tabulated. Therefore, for each RM_{ON} position I find the closest tabulated extinction point (within a distance of 0.1 pc) and assign it to that RM_{ON} . This provides the extinction along the entire path length at each ON position ($A_{V, ON}$).

Since each chosen OFF position also has an associated A_V , after finding the optimum number of OFF positions and the value of RM_{ref} for each MC, I also find the average extinction value of the reference position using

$$A_{V, ref} = \sum_{i=1}^N \frac{A_{V, OFF, i}}{N}. \quad (3.9)$$

The values of $A_{V, ref}$ are 0.45, 0.46, 0.54, and 0.67 for OMC-A, OMC-B, CMC, and PMC, respectively. To find the extinction value of the MC itself, I once again subtract the extinction in OFF position from that in the ON position, that is,

$$A_{V, MC} = A_{V, ON} - A_{V, ref}. \quad (3.10)$$

Determining the Electron Column Density

In order to estimate the electron abundance, one requires a chemical model, which incorporates a number of relevant chemical reactions for particular gas conditions (density, temperature, UV field strength, cosmic ray ionization rate, etc.) and finds the abundance of each species as a function of time and depth (or A_V) within the cloud. I use an in-house chemical evolution code, developed by René Plume, which has been rigorously tested against the results of other established codes (see Gibson et al. 2009).

The chemical code utilises the UMIST Rate 99 database to obtain the reaction rates (Le Teuff et al. 2000). This code uses a small network of 229 gas-phase reactions coupling 28 different species including C, C⁺, CO, O, O₂, CH, CH⁺, CO⁺, H, H₂, H₂O⁺, H₃O⁺, HCO⁺, O⁺, etc. Additionally this code includes a simple treatment for gas-grain interactions via adsorption, thermal evaporation, CR desorption and photodesorption in manner outlined by Bergin et al. (1995) and Hasegawa and Herbst (1993). It does not include any surface-grain reactions.

This chemical code assumes that each MC has a constant density and temperature, and is illuminated externally by a constant UV field (parametrised by G_o , where $G_o = 1$ Habing is the strength of the average ISM radiation field²) and CR ionization rate. For each of the clouds, I obtain the first three parameters from the literature. I assume a constant CR ionization rate of $1.3 \times 10^{-17} \text{ s}^{-1}$ for all clouds.

The chemical code takes each cloud to be homogeneous and planar in structure, and is sliced into 100 layers of equal thickness. Each layer corresponds to a different depth into the cloud and therefore I can calculate the amount of visual extinction (A_V) from the exterior (surface) of the cloud to the center of each layer. This controls how the external UV is attenuated as a function of depth, which, in turn, affects the importance of photo-reactions. In each layer, the code starts with standard cosmic abundances of all species and runs until we achieve chemical equilibrium. The final outcome is a list of the equilibrium abundance of

²1 Habing = $1.6 \times 10^{-3} \text{ erg s}^{-1} \text{ cm}^{-2}$ (Habing 1968).

each species (including free electrons) as a function of extinction (depth) into the cloud.

Even though I use a simple homogeneous, plane-parallel chemical model rather than a more sophisticated hydrodynamic approach (e.g., Seifried et al. 2017a; Clark and Glover 2014; Smith, Glover, Clark, Klessen and Springel 2014; Glover and Clark 2012), this simplified model provides electron abundances that are similar to these more detailed models. For example, I find that the calculated electron abundances are consistent with those of Glover et al. (2010) in densities of 100 cm^{-3} and 1000 cm^{-3} . This is true even though their initial temperature is different from my initial values. They, however, incorporate a cooling system that allows the high-extinction parts of the gas to cool down to 10 K, which is close to the temperatures I have for the selected regions. These electron abundances are also consistent with those from a variety of established PDR/chemical models (see the comparison by Röllig et al. (2007)). Thus, in this work, there does not seem to be much to gain from applying a more sophisticated approach to the chemical modeling.

The chemical model calculates the electron abundance in each layer of the cloud. However, to reach any given layer, we pass through all overlying layers that may have different electron abundances. Consequently, to calculate the electron column density for a position in the MC with a given A_V , one cannot naively assume that the total electron column density is obtained directly from the electron abundance of one single layer multiplied by the total column density of that position (i.e., $N_e = X_e \times N(\text{HI} + \text{H}_2)$ with X_e and $N(\text{HI} + \text{H}_2)$ being the electron abundance and the hydrogen column density of that position, respectively). I must, instead, account for the contribution of each layer separately, since in each layer the electron abundance may be different due to the different UV attenuation.

The total electron column density, N_e , is given by the equation:

$$N_e = \sum N_{e,i}, \quad (3.11)$$

where $N_{e,i}$ is the electron column density in each layer and the sum is performed over all

overlying layers from the surface of the cloud to the layer of interest. $N_{e,i}$, in turn is given by

$$N_{e,i} = X_{e,i} \times N_i(HI + H_2), \quad (3.12)$$

where $X_{e,i}$ is the electron abundance in each layer and is calculated by the chemical model. $N_i(HI + H_2)$ is the hydrogen column density in each overlying layer. To evaluate $N_i(HI + H_2)$ in each layer, I first subtract the extinction of that layer ($A_{V,i}$) from the extinction of the layer above ($A_{V,i-1}$) and then use the conversion factor of $2.21 \times 10^{21} \text{ cm}^{-2} \text{ mag}^{-1}$ by Bohlin et al. (1977) (also see Güver and Öznel 2009) as follows:

$$N_i(HI + H_2) = (A_{V,i} - A_{V,i-1}) \times 2.21 \times 10^{21}. \quad (3.13)$$

Hence, the total electron column density along the line of sight from the surface of the MC to the layer of interest becomes

$$N_e = \sum N_{e,i} = \sum (X_{e,i} \times (A_{V,i} - A_{V,i-1})) \times 2.21 \times 10^{21}. \quad (3.14)$$

To assess which layers we must include in equation 3.14, I presume the cloud is symmetrical along the line-of-sight as represented in Figure 3.3 and that the UV field is equally illuminating both sides of the cloud. However, the value of $A_{V,MC}$ obtained from the extinction maps is a measure of the extinction through the entire MC (front and back). Accordingly, in an MC with $A_{V,MC} = X$, the total amount of UV attenuation from surface to center is only $X/2$.

The chemical model, however, assumes that the UV field is illuminating only one side of the cloud. Therefore, at a position where I measure $A_{V,MC}$ from the extinction maps, I only perform the sum in equation 3.14 to a layer with $A_{V,MC}/2$. Subsequently, I multiply the final sum by a factor of two to account for the fact that both the front and back sides of the MC contribute equally to the total N_e through the cloud. Thus, the final solution for N_e

is given by:

$$\begin{aligned} N_e &= 2 \times \sum N_{e,i} \\ &= 2 \times \sum^{\frac{A_{V,MC}}{2}} ((A_{V,i} - A_{V,i-1}) \times X_{e,i}) \times 2.2 \times 10^{21}. \end{aligned} \quad (3.15)$$

Using equations 3.8 and 3.15, along with the output from the chemical models and the measured ON and reference rotation measures, therefore enables us to calculate the line-of-sight magnetic field strength and direction in MCs.

The following example illustrates how this is done practically. I consider a particular point (for the purposes of this example, Point 22 in Figure 3.7 in OMC-A, at $\alpha(J2000) = 86.31^\circ$, $\delta(J2000) = -5.49^\circ$). In the TSS09 catalog this position has an RM value of $23.5 \pm 9.5 \text{ rad m}^{-2}$. From the KBHP09 maps, this position has an extinction value of $A_V = 2.84 \text{ mag}$.

Using values for density, temperature, UV field strength, and so on, found from the literature (see section 3.4.1 for details) René Plume runs the chemical code to generate a list of abundances as a function of extinction (or depth) into the MC. Since $A_{V,\text{ref}}$ for OMC-A is 0.45, $A_{V,MC}$ for the MC at this point is $2.84 - 0.45 = 2.39$. Thus, in the output of the chemical code, I find the electron abundances in all layers from $A_{V,MC} = 0$ to 1.20. The output of the code contains five layers to reach to this extinction value. These layers are $(A_{V,i}, X_{e,i}) = (0.16, 1.40 \times 10^{-4}), (0.46, 1.40 \times 10^{-4}), (0.78, 1.41 \times 10^{-4}), (1.08, 1.41 \times 10^{-4}),$ and $(1.40, 1.42 \times 10^{-4})$. The last layer, however, does not exactly match 1.20. Therefore, I interpolate between the last two layers, to find the electron abundance for a layer in between with an extinction value of 1.20.

Subsequently, using equation 3.15 I find N_e as follows:

$$\begin{aligned}
N_e = & 2 \times \left((0.16 - 0) \times 1.40 \times 10^{-4} \right. \\
& + (0.46 - 0.16) \times 1.40 \times 10^{-4} \\
& + (0.78 - 0.46) \times 1.41 \times 10^{-4} \\
& + (1.08 - 0.78) \times 1.41 \times 10^{-4} \\
& \left. + (1.20 - 1.08) \times 1.41 \times 10^{-4} \right) \text{mag} \times 2.2 \times 10^{21} \text{cm}^{-2} \text{mag}^{-1} \\
= & 7.42 \times 10^{17} \text{cm}^{-2}.
\end{aligned} \tag{3.16}$$

Since the value of RM_{ref} for OMC-A is 1.4 rad m^{-2} (section 3.3.1), $\text{RM}_{\text{ON}} - \text{RM}_{\text{ref}}$ used in equation 3.8 is $23.5 - 1.4 = 22.1 \text{ rad m}^{-2}$. Finally, B_{LOS} is calculated from equation 3.8 as:

$$\frac{22.1 \text{ rad m}^{-2}}{7.42 \times 10^{17} \text{cm}^{-2} \times 3.24 \times 10^{-19} \text{pc cm}^{-1} \times 0.812 \frac{\text{rad cm}^3}{\text{m}^2 \mu\text{G pc}}} = 113 \mu\text{G}. \tag{3.17}$$

Results of this calculation for all four MCs considered in this chapter are provided in Tables 3.1, 3.3, 3.4, and 3.6 and Figures 3.7 to 3.5. Details and discussion for each MC are provided in section 3.4.

3.3.3 Uncertainty Analysis and Sensitivity Study

I carry out several analyses to determine how uncertainties in the chosen number of reference points, RM values, chemical code input parameters, positions, and extinction propagate into errors in the derived B_{LOS} . I discuss these below.

Since my B_{LOS} values are obtained using equation 3.8, to estimate the uncertainties in the resultant B_{LOS} , I need to examine the uncertainties induced by both the catalogued RM values and the calculated N_e . Since the uncertainty in N_e depends on the chemical model and its input parameters, I have to investigate the uncertainties that are caused by changing

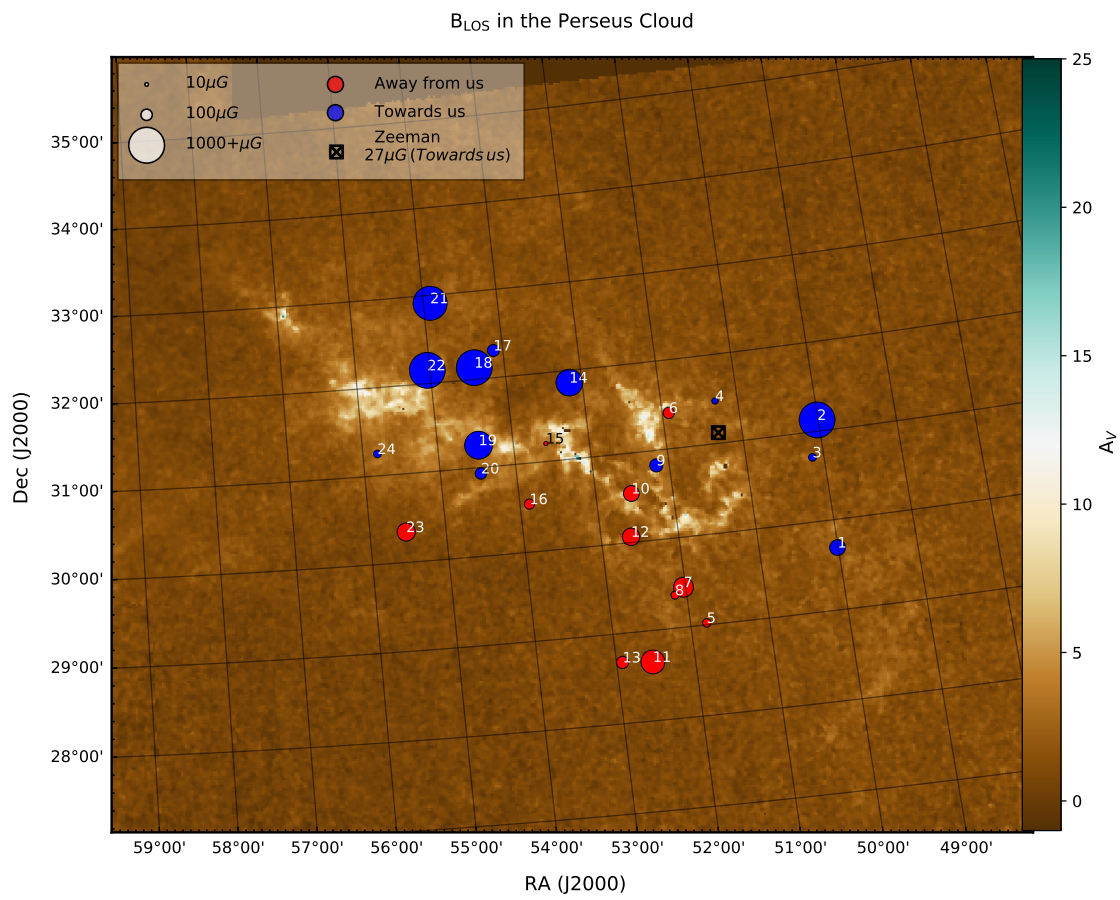


Figure 3.5: B_{LOS} in the Perseus MC. Blue (red) circles show magnetic fields toward us (away from us). The size of the circles indicate the magnitude of magnetic field. Black square shows the location of the available Zeeman measurements. Color image is the extinction map (A_V).

the input temperature and volume density. Additionally, since I positionally overlay the RM catalog and extinction maps, I have to account for any possible mismatches between the RM positions and the grid on which the extinction maps are produced. This mismatch translates into a possible error in the value of A_V assigned to any given RM point. Therefore, my B_{LOS} values are a function of the catalogued RM values, A_V (which, in itself, is a function of the positional coordinates), and the chemical model input density and temperature. Thus B_{LOS} is parameterised by $B_{\text{LOS}}(\text{RM}, A_V, n(\text{HI} + \text{H}_2), T)$ and has an uncertainty of:

$$\delta B_{\text{LOS}} = B_{\text{LOS}} \left(\left(\frac{\delta \text{RM}}{\text{RM}} \right)^2 + \left(\frac{\delta A_V}{A_V} \right)^2 + \left(\frac{\delta n(\text{HI} + \text{H}_2)}{n(\text{HI} + \text{H}_2)} \right)^2 + \left(\frac{\delta T}{T} \right)^2 \right)^{1/2}. \quad (3.18)$$

Uncertainty in B_{LOS} From RM

In the RM catalog of TSS09, the source entries include sky position, Stokes I (total intensity), linear polarised intensity, fractional polarisation, and RM, with estimated errors for each entry. Accordingly, each RM value in the TSS09 catalog has a corresponding RM uncertainty that I incorporate into my error bars. For the ON positions, I simply take the associated errors listed for those positions. The uncertainty in the RM_{ref} measurement, however, is the standard deviation of the RM values of the chosen OFF positions. The B_{LOS} uncertainty from RM for each point is found as follows:

$$\Delta B_{\text{RM}} = B_{\text{LOS}} \left(\frac{\delta(\text{RM}_{\text{ref}}) + \delta(\text{RM}_{\text{ON}})}{\text{RM}_{\text{ON}} - \text{RM}_{\text{ref}}} \right), \quad (3.19)$$

where ΔB_{RM} is the uncertainty in B_{LOS} from RM, $\delta(\text{RM}_{\text{ref}})$ is the standard deviation of the OFF positions, and $\delta(\text{RM}_{\text{ON}})$ is the tabulated uncertainty of the RM of the ON point.

Considering OMC-A as an example once more, I calculate the standard deviation in RM_{ref} for OMC-A to be 13.7 rad m^{-2} (using 12 OFF positions to calculate RM_{ref}). Thus, RM_{ref} in OMC-A is $1.4 \pm 13.7 \text{ rad m}^{-2}$.

I note that the uncertainties in the RMs tabulated in TSS09 and in the reference positions are the dominant source of error in my magnetic field calculation, and are the main reason that the uncertainties listed in Tables 3.1 to 3.7 are as large as they are. For instance, the tabulated value of RM_{ON} of Point 22 used in the example above is $23.5 \pm 9.5 \text{ rad m}^{-2}$, which results in large fractional errors in the derived magnetic field values. In the TSS09 catalog there are also points like Point 21 (see Table 3.1) with an RM_{ON} value of $-0.3 \pm 6.9 \text{ rad m}^{-2}$, which creates enormous relative uncertainty. This is discussed further in section 3.5.1.

Uncertainty in B_{LOS} From N_e

Uncertainties in the electron column density are caused by uncertainties in the chemical code input parameters, since the density, temperature, and UV field strength may not be well characterised.

To investigate how changes in density affect the electron abundance, I hold all other input parameters constant and change the input volume density, ($n(\text{HI} + \text{H}_2)$), by $\pm 1\%$, $\pm 2.5\%$, $\pm 5\%$, $\pm 10\%$, $\pm 20\%$, $\pm 30\%$, $\pm 40\%$, $\pm 50\%$ from the cloud fiducial input density, n_0 . René Plume then reruns the chemical code with the altered density and obtain a new value for the electron abundance. Consequently, I obtain the value of B_{LOS} for each point with the new electron abundances. I then calculate the B_{LOS} differences from the original B_{LOS} value. I denote these uncertainties in B_{LOS} as $\Delta B_{n(\text{HI} + \text{H}_2)}$.

Referring back to OMC-A as an example, Figure 3.6 demonstrates how B_{LOS} changes as the input density is varied. The top panel of Figure 3.6 shows B_{LOS} deviations for a selection of data points in OMC-A. The z-axis (ΔB) indicates changes in B_{LOS} from the fiducial value (obtained from the fiducial input density n_0). The x-axis ($\frac{\Delta n}{n_0}$) indicates the relative changes in the cloud initial (fiducial) density, and the y-axis indicates particular data points in OMC-A as mapped in Figure 3.7. While I have performed this error analysis for every point, I only display a few select points for clarity. The bottom left panel of Figure 3.6 represents variations in B_{LOS} for data points with $A_V > 1$, and the bottom right panel shows

the same for data points with $A_V < 1$. These figures show that B_{LOS} variations are largest in the regions with lower visual extinction. The main reason for this behavior is that in low A_V regions, the electron fraction is high and so changes in density result in relatively large changes in N_e which, in turn, affects B_{LOS} . On the other hand, in the high A_V regions, since we are looking through many cloud layers, changes in N_e are averaged over many layers.

The resultant uncertainties in B_{LOS} caused by changes in N_e are asymmetrical and, therefore, I report magnetic field values in the form of $B_{-\delta B}^{+\delta B}$, and in the case where the two δB are the same, in the form of $B \pm \delta B$.

I carry out a similar analysis for the input temperature by varying it by $\pm 5\%$, $\pm 10\%$, and $\pm 20\%$ from the cloud fiducial input temperature, T_0 , while holding the other parameters constant. Similarly I obtain the electron abundance and therefore the new magnetic field values for each point. Changes to the input temperature introduce fairly small variations to B_{LOS} . I denote these uncertainties as ΔB_T .

Uncertainty in B_{LOS} From Extinction and Position

Since we have an uncertainty in matching the position between the RM catalog points and the grid on which the extinction maps are calculated (see section 3.3.2), this translates into an error, $\Delta B_{\text{ext, coord}}$, in the assumed A_V . This arises because, while I take the A_V value that lies closest to the RM position, there may be more than one value of A_V in a 0.1 pc radius surrounding the RM point. To estimate the influence that this has on the derived magnetic fields, I calculate B_{LOS} for the maximum and minimum A_V that falls within a 0.1 pc radius around each RM position.

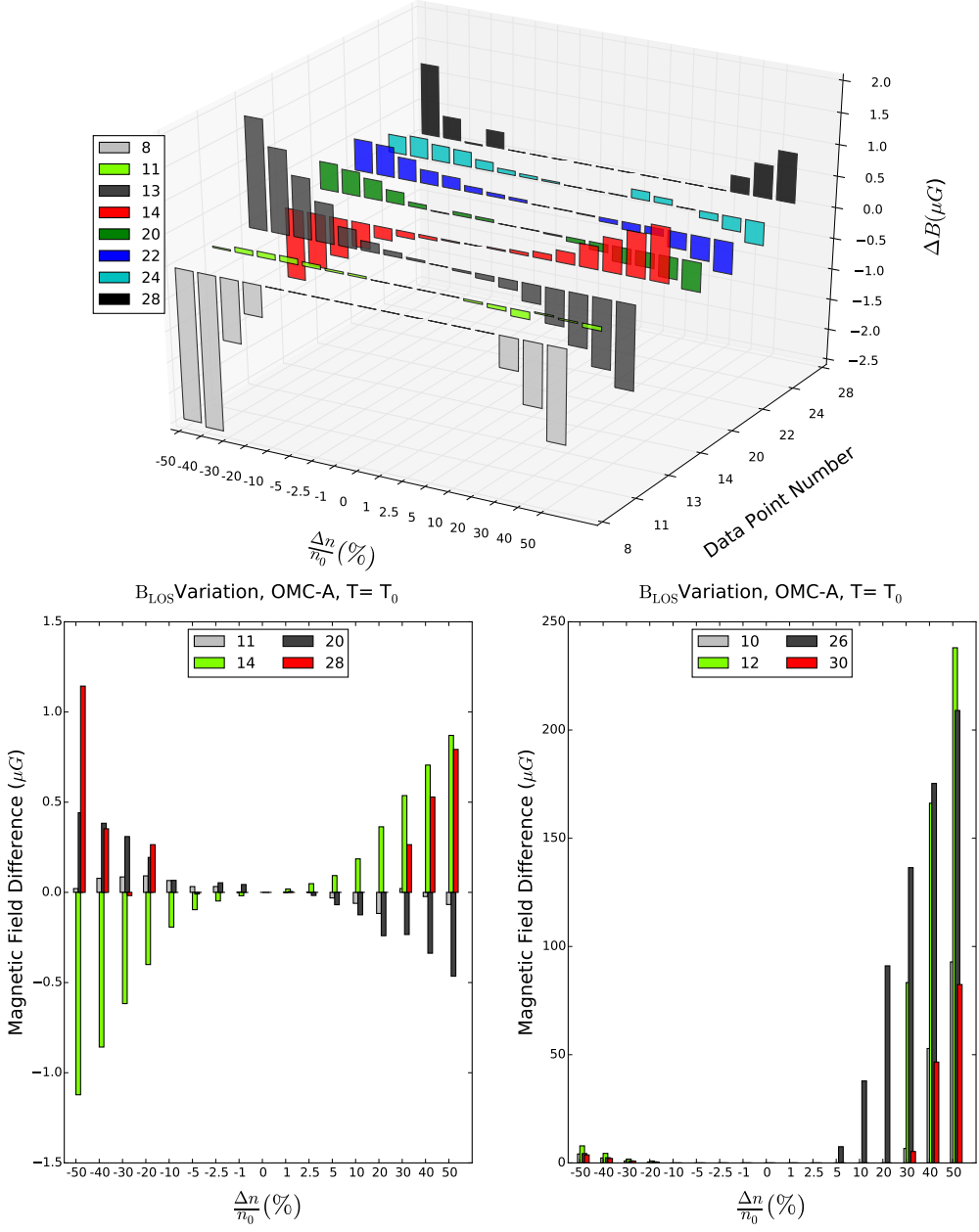


Figure 3.6: Uncertainties in B_{LOS} due to uncertainties in the input volume density of the chemical evolution code. **Top Panel:** B_{LOS} variation for a selection of positions in Orion A sampling regions with different A_V . The x-axis ($\frac{\Delta n}{n_0} (\%)$) indicates the relative (%) changes in input density to the chemical model. The y-axis labels the data points presented and corresponds to the positions labeled in Figure 3.7. The z-axis plots the change in the magnetic field strength and direction from that calculated for the fiducial density n_0 (10^4 cm^{-3}). The **bottom left panel** shows B_{LOS} uncertainties for points with $A_V < 1$. The **bottom right panel** shows uncertainties in B_{LOS} for a selection of points with $A_V > 1$.

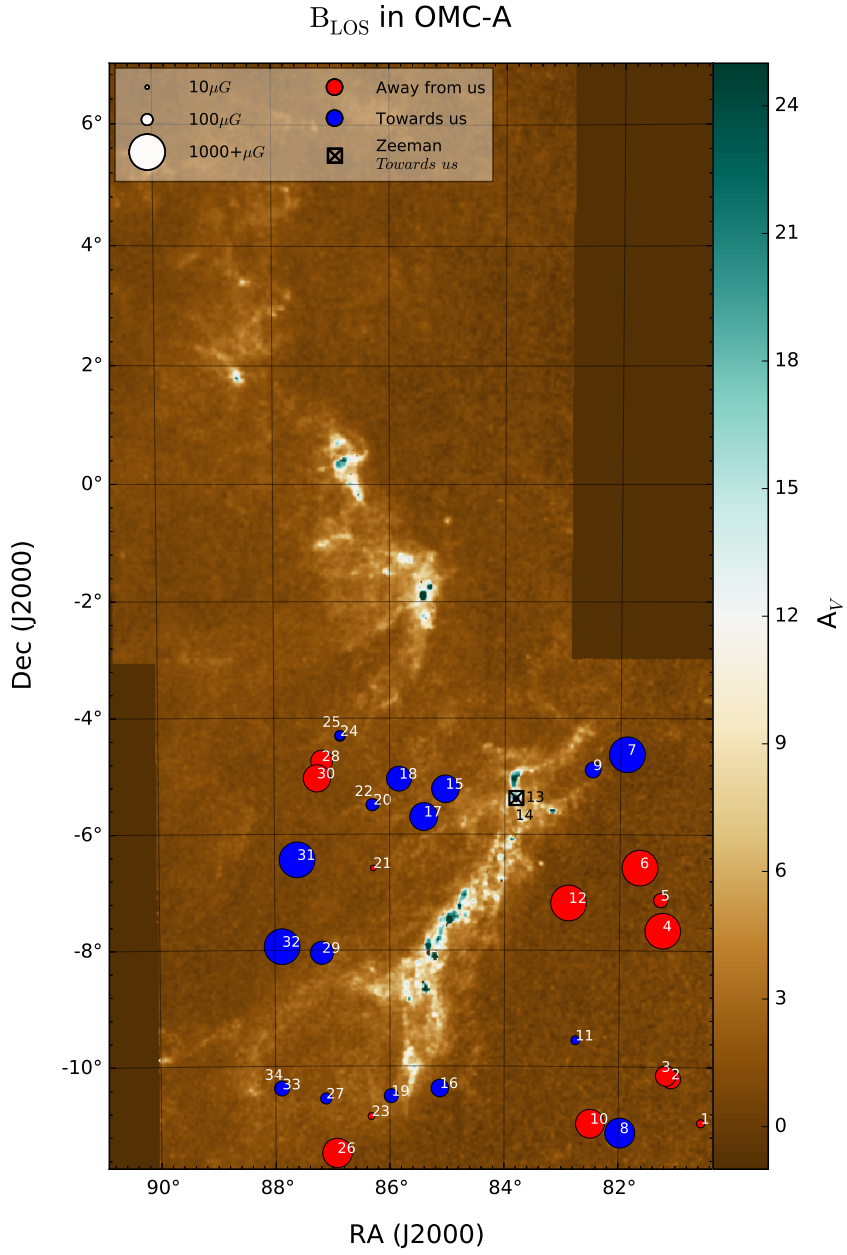


Figure 3.7: B_{LOS} in OMC-A. Blue (red) circles show magnetic fields toward us (away from us). The size of the circles indicate the magnitude of magnetic field. Black square shows the location of the available Zeeman measurements. Color image is the extinction map (A_V). The magnetic fields are dominantly towards us at the eastern side of this filamentary structure and away from us at its western side.

Total B_{LOS} Uncertainty

After finding the individual uncertainties, I can find the total uncertainty, by converting equation 3.18 into the following form:

$$\delta B_{\text{LOS}} = \left((\Delta B_{\text{RM}})^2 + (\Delta B_{\text{ext, coord}})^2 + (\Delta B_{n(\text{H}_1+\text{H}_2)})^2 + (\Delta B_T)^2 \right)^{1/2}, \quad (3.20)$$

where ΔB_{RM} is the error in B produced by the RM uncertainties for each data point in the TSS09 catalog along with the reference RM, $\Delta B_{\text{ext, coord}}$ is the error in B produced by the uncertainty in the assumed extinction value, $\Delta B_{n(\text{H}_1+\text{H}_2)}$ is the error in B produced by the uncertainties in the chemical code input density, and ΔB_T is the same due to uncertainties in the input temperature. I believe that I have been quite conservative in estimating the total B_{LOS} error and, therefore, the true error may indeed be smaller than those quoted in Tables 3.1, 3.3, 3.4, and 3.6.

3.4 Results

I used the method described above for each of the four MCs in my sample (OMC-A, OMC-B, PMC, and CMC). I compared the results to existing Zeeman measurements to verify the validity of the method. I discuss the results for each of these regions below.

3.4.1 Strength and Morphology of B_{LOS} in Orion A & B

The OMC is a well-studied, active star-forming region with relatively strong magnetic fields (Crutcher 1999; Crutcher et al. 2010). Some prominent regions in OMC are the Orion Nebula Cluster, L1641, NGC2026, and NGC2024 with distances of 388 ± 5 pc, 428 ± 10 pc, 388 ± 10 pc, and roughly 420 pc, respectively (Kounkel et al. 2017).

Orion A and B are the two distinct giant molecular clouds in the OMC complex. OMC-A

is located at $80^\circ < \alpha(J2000) < 88^\circ$ and $-12^\circ < \delta(J2000) < -4^\circ$, while OMC-B is located at $84^\circ < \alpha(J2000) < 95^\circ$ and $-4^\circ < \delta(J2000) < 4^\circ$.

For both regions, I use $n(HI+H_2) = 10^4 \text{ cm}^{-3}$ (Castets et al. 1990; Dutrey et al. 1993; Johnstone and Bally 1999*a,c*), $T = 25 \text{ K}$ (Mitchell et al. 2001; Johnstone and Bally 2006; Bally et al. 1991; Castets et al. 1990; Schnee et al. 2014; Buckle et al. 2012), and a UV field strength of $G_o = 10^4$ (where $G_o = 1$ Habing is the strength of the average interstellar UV field) as input to the chemical models.

Using the methodology described above, I calculate B_{LOS} for all the available RM points in OMC-A and B. These results are presented in Figures 3.7 and 3.8. Derived values of B_{LOS} for Orion A & B are provided in Tables 1 and 3. The reason for the large uncertainties was discussed in section 3.3.3 and is explored in more detail in section 3.5.1.

To examine the veracity of this method, I compare my derived magnetic field strengths to those determined from other well-known methods, such as Zeeman measurements. For these two regions several molecular Zeeman measurements are available (Troland et al. 1986, 1989; Crutcher, Roberts, Troland and Goss 1999; Crutcher 1999; Crutcher, Troland, Lazareff, Paubert and Kazès 1999; Crutcher et al. 1996; Verschuur 1996; Crutcher et al. 2010) and are graphically represented on Figures 6 and 7 as black squares.

I note that conventionally the negative sign represents magnetic field towards us in Zeeman measurements and away from us in RM studies. For consistency between discussions of RM and Zeeman measurements, I adopt the convention that $-B_{\text{LOS}}$ indicates a magnetic field directed away from the observer and a $+B_{\text{LOS}}$ indicates a magnetic field toward the observer.

There are a number of Zeeman measurements in OMC-A, most of which fall in the vicinity of a high-extinction region with approximate coordinates of $\alpha(J2000) \simeq 83.81^\circ$, $\delta(J2000) \simeq -5.37^\circ$. The magnetic fields inferred from these different studies have wildly different values and, often, large error bars; for example, $+360 \pm 80 \mu\text{G}$ (Falgarone et al. 2008; Crutcher 1999; Crutcher et al. 2010), $-79 \pm 99 \mu\text{G}$ (Crutcher et al. 1996), $-40 \pm 240 \mu\text{G}$ (Crutcher, Troland, Lazareff, Paubert and Kazès 1999; Crutcher et al. 2010), $+190 \pm 90 \mu\text{G}$ (Crutcher, Troland,

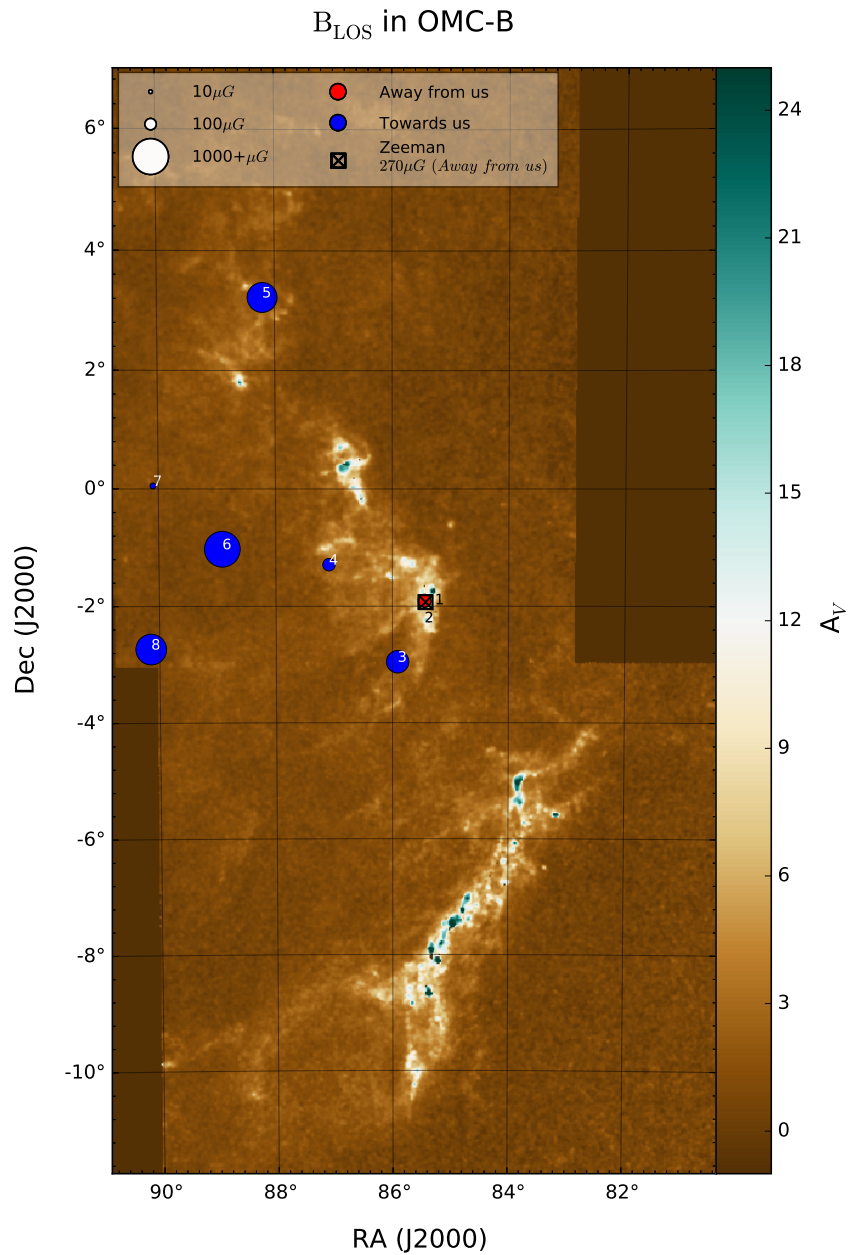


Figure 3.8: B_{LOS} in OMC-B. Blue (red) circles show magnetic fields toward us (away from us). The size of the circles indicate the magnitude of magnetic field. Black square shows the location of the available Zeeman measurements. Color image is the extinction map (A_V).

Lazareff, Paubert and Kazès 1999), and $-80 \pm 100 \mu\text{G}$ (Crutcher et al. 2010). These studies suggest that the magnetic field in this region (including error bars) might have any strength from $+440 \mu\text{G}$ to $-280 \mu\text{G}$. For this region, Pattle et al. (2017) finds a value of $6.6 \pm 4.7 \text{ mG}$ for B_{POS} using dust polarisation technique.

In comparison, using this technique I have two data points in this area (sources 13 and 14 in Table 3.1 and Figure 3.7) with magnetic field values of $-23 \pm 38 \mu\text{G}$ and $+15 \pm 36 \mu\text{G}$, respectively. Given the large error bars in both this technique and the Zeeman measurements, as well as the large dispersion in the Zeeman values, I find it promising that: a) my magnetic field strengths and directions fall within the range of those determined via Zeeman measurements, and b) that my error bars for these positions are, in fact, smaller than those for the Zeeman measurements. Thus, I suggest that there is qualitative agreement between my results and those from Zeeman measurements. Having said that, comparing the two must be done cautiously as we are possibly looking at different regions within the MC (see section 3.5.3).

Given that there are many more RM observations across the Galaxy than there are Zeeman measurements, this technique can also provide useful insight into the morphology of the line-of-sight magnetic field in MCs. For example, Figure 3.7 suggests that the magnetic field on the eastern side of OMC-A is predominantly positive (blue), whereas on the western side it is negative (red). This particular pattern has previously been observed (Heiles 1997), and interpreted as helical magnetic fields (e.g., Johnstone and Bally 1999*b*; Hoq et al. 2017; Matthews et al. 2001). I discuss this possibility in more detail in section 3.5.2.

The two available Zeeman measurements in OMC-B are in a high extinction area at $\alpha(J2000) \simeq 85.44^\circ$, $\delta(J2000) \simeq -1.93^\circ$, and have significantly different magnetic field strengths and error bars; for example, $-270 \pm 330 \mu\text{G}$ (Crutcher, Troland, Lazareff, Paubert and Kazès 1999) and $-87 \pm 5.5 \mu\text{G}$ (Crutcher, Roberts, Troland and Goss 1999). My measurements in this proximity are Points 1 and 2 (see Table 3.3 and Figure 3.8) with magnetic field values of $-119 \pm 25 \mu\text{G}$ and $-129 \pm 28 \mu\text{G}$ (i.e., both pointing away from us).

As with OMC-A, there is general agreement in both the direction and strength of magnetic field between the two Zeeman measurements and my own results. There are, however, fewer RM points in OMC-B with which to infer the large-scale morphology of the magnetic field.

3.4.2 California and Perseus

It is important to test this method in different environmental conditions besides the well-known region of Orion. Thus, I test my method in the PMC and CMC, which have lower density and ambient UV field strengths than Orion.

Strength and Morphology of B_{LOS} in the California Molecular Cloud

The CMC occupies a region of roughly $58^{\circ} < \alpha(J2000) < 70^{\circ}$ and $34^{\circ} < \delta(J2000) < 42^{\circ}$ (Lombardi et al. 2010). It is part of the Gould Belt and has modest star formation activity (Harvey et al. 2013). Lada et al. (2009) report a distance of 450 ± 23 pc to the cloud. The cloud extends around 80 pc and has a mass of around $10^5 M_{\odot}$.

Considering the results of Kong et al. (2015) and Lada et al. (2009) I take an initial volume density of $n(\text{HI} + \text{H}_2) = 450 \text{ cm}^{-3}$, a temperature of $T = 10 \text{ K}$, and UV field radiation strength of $G_{\odot} = 1.0$ Habing for the input to the chemical models. Using the same method described in section 3.3, I then calculate the magnetic field strength and direction in CMC. The results are shown in Figure 3.9 with their values listed in Table 3.4. My derived values for B_{LOS} in the CMC are not very sensitive to the uncertainties in coordinate and extinction values or to uncertainties in the chemical code input parameters, and their dominant source of uncertainty comes from RM uncertainties.

While there are no Zeeman measurements available for this region to compare with my results, Figure 3.9 does exhibit some interesting morphological characteristics; it shows that the magnetic fields on the eastern side of the CMC are pointing away from us, while on the western side they are pointing towards us. This morphology is similar to that seen in OMC-A, and might be an indication of helical magnetic field in this filamentary structure as well.

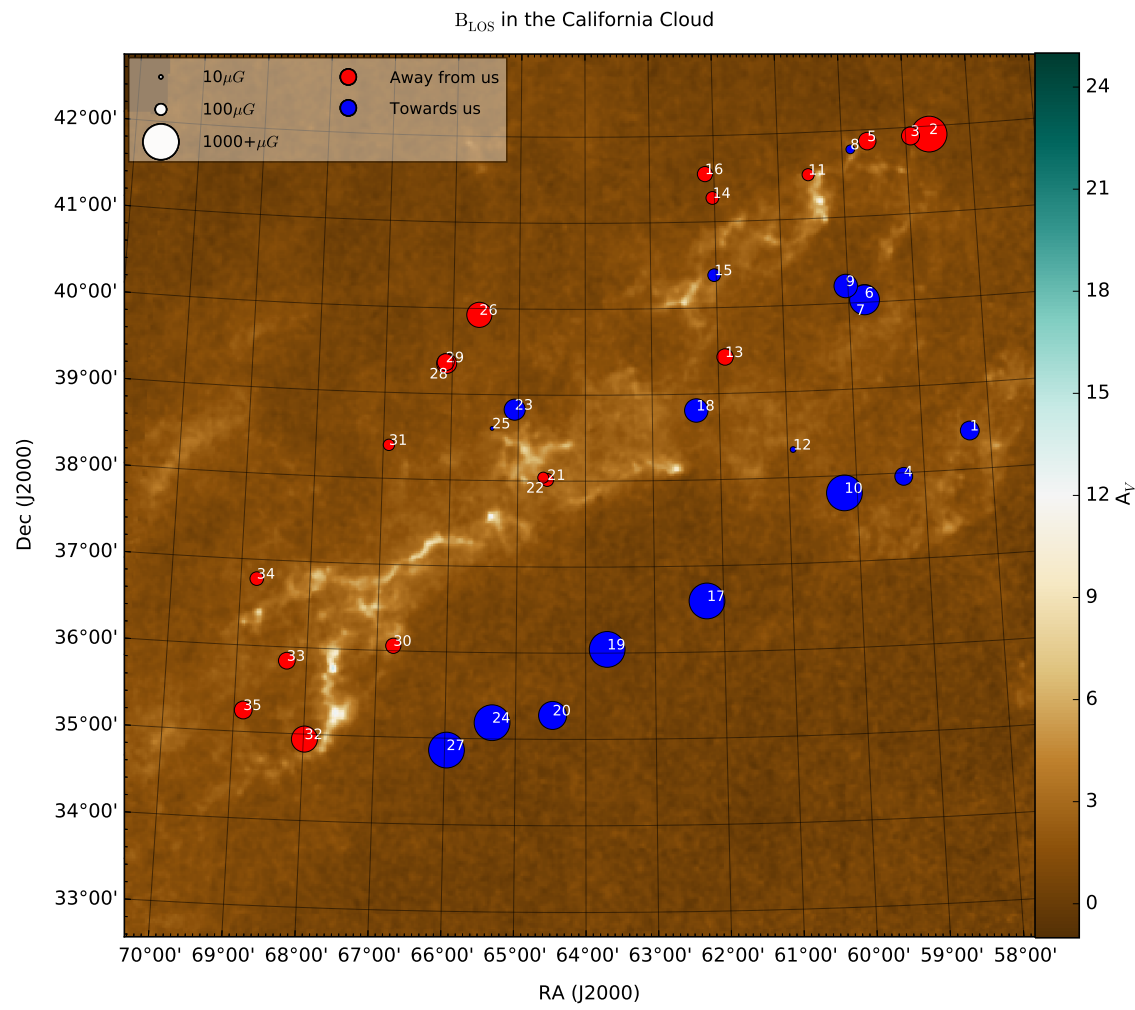


Figure 3.9: B_{LOS} in the California MC. Blue (red) circles show magnetic fields toward us (away from us). The size of the circles indicate the magnitude of magnetic field. Color image is the extinction map (A_V). The magnetic fields are dominantly towards us at the western side of this filamentary structure and away from us at its eastern side.

Strength and Morphology of B_{LOS} in the Perseus Molecular Cloud

The PMC is a well-known star-forming region at a position of $50^\circ < \alpha(J2000) < 58^\circ$ and $28^\circ < \delta(J2000) < 34^\circ$, and at a distance of about 300 pc from the Sun (Bally et al. 2008). To find the proper input physical parameters to use in the chemical code, I use results found in the literature. Bachiller and Cernicharo (1986) study different regions within Perseus and, for the globule L1455 (=B204, B206), they report a temperature of 12 K. In the position of the NH_3 peak they find a density of $n(\text{H}_2) \simeq 1.4 \times 10^4 \text{ cm}^{-3}$. Bachiller and Cernicharo (1984) mention that B1, has a mean density of $n \geq 10^3 \text{ cm}^{-3}$ and is connected to the rest of the complex with densities of $n \simeq 10^3 \text{ cm}^{-3}$. Considering this along with Table 3.2 presented in Bachiller and Cernicharo (1986), I choose 10^3 cm^{-3} for the average density and 12 K for the temperature. Additionally, I select a UV field radiation strength of $G_\circ = 1.0$ Habing.

There are several Zeeman measurements available in the well-known B1 molecular core in the PMC (Goodman et al. 1989; Crutcher et al. 1993; Verschuur 1996), which suggest small magnetic fields. For the B1 region ($\alpha(J2000) \simeq 51.32^\circ, \delta(J2000) \simeq 31.12^\circ$), Goodman et al. (1989) obtain a magnetic field of $+27 \pm 4 \mu\text{G}$, and Crutcher et al. (1993) report $+19.1 \pm 3.9 \mu\text{G}$. For the same position Verschuur (1996) finds a magnetic field of $+16.7 \pm 8.9 \mu\text{G}$ using the 1665 MHz OH line and $-6.2 \pm 8.5 \mu\text{G}$ using the 1667 OH line. The closest point to this location is Point 4 in Figure 3.5 and Table 3.6, with a value of $+32 \pm 101 \mu\text{G}$. My result is in agreement with all of these reported Zeeman measurements. The main source of uncertainty of the magnetic field strength using my method is due to uncertainties in the RMs in the TSS09 catalog.

Figure 3.5 seems to suggest that the magnetic fields on the southern side of the PMC are pointing away from us and that those on the northern side are pointing towards us, however, more data points would be required to draw any firm conclusions since there is a paucity of RMs on the southern side of the cloud.

3.5 Discussion

As mentioned above, the derived magnetic field strengths (see Tables 3.1, 3.3, 3.4, and 3.6) often have relatively large uncertainties and, in some cases, the error bars are larger than the tabulated value of B_{LOS} . As mentioned in section 3.3.3, the dominant source of errors in my method is the errors of the RMs as tabulated in TSS09.

3.5.1 Decreasing the Uncertainties in B_{LOS}

The RMs of the TSS09 were calculated using two frequencies in combination with the fractional depolarisation as a function of rotation measure. Errors in the calculated RM could be reduced by re-observing the same sources (in addition to more sources) with new generation radio telescopes such as the LOw-Frequency ARray (LOFAR). For example, in their Table 3.1, Van Eck et al. (2017) compare their RM results using LOFAR with the TSS09 catalog. While the absolute values are in good agreement, the RM uncertainties presented in Van Eck et al. (2017) (0.05 rad m^{-2}) are significantly smaller than those in TSS09 catalog (10 rad m^{-2}). These reductions in RM uncertainties can accordingly improve the error bars associated with my procedure. For example, for Point 4 in OMC-B in Table 3, if I were to hold all other values constant and change the RM uncertainty to 0.05 rad m^{-2} , the final B_{LOS} would be $122 \pm 50 \mu\text{G}$, instead of the currently tabulated $122 \pm 125 \mu\text{G}$. In addition, in this “new and improved” B_{LOS} value of $122 \pm 50 \mu\text{G}$, the largest source of error is now from RM_{ref} . Errors in RM_{ref} could be reduced by improved sensitivity RM observations which could provide additional RM_{OFF} data points to be used in the calculation of RM_{ref} . Since the error in RM_{ref} is a standard deviation, with additional points, Poisson statistics should decrease its error.

Even with the current uncertainties in RM_{ON} , I can improve the robustness of my results by removing from consideration any position that has an uncertainty greater than 100% of the calculated B_{LOS} value. Tables 2, 5, and 7 are subsets of Tables 1, 4, and 6 that contain

only the points with error bars less than 100% of the magnetic field strength. Although the uncertainty in the absolute value of B_{LOS} of any point may still be relatively high, the *direction* of the magnetic field for the points in these tables is fixed. Therefore, these data can still provide us with insight into the large-scale magnetic field morphology in MCs. This is discussed in section 3.5.2 below.

3.5.2 Magnetic Field Morphology: Evidence for Helical Fields?

In OMC-A, Figure 3.7, suggests that B_{LOS} on the east side of OMC-A tends to point away from us, whereas on the west side it tends to point towards us. This holds true even if I only use the B_{LOS} values listed in Table 3.2, which have error bars small enough that the magnetic field direction is fixed. In fact, my interpretation is more robust using the data in Table 3.2, since Points 21, 28, and 30 on the east side of the cloud and 11, and 16 on the west side of the cloud are removed. Removing these points strengthens the perceived large-scale pattern of the magnetic field by reducing the number of positions with opposing B_{LOS} directions.

This magnetic field configuration has previously been observed in OMC-A (Heiles 1997), and interpreted as a helical magnetic field wrapping around the cloud (Heiles 1987) or bending of the ambient magnetic field lines around the filamentary structure due to the Orion-Eridanus shocks. I will examine these morphologies in Chapter 4. Other observations have been indirectly interpreted as indications of a helical magnetic field structure (e.g., Johnstone and Bally 1999b; Hoq et al. 2017; Matthews et al. 2001; Contreras et al. 2013; Stutz and Gould 2016). For example, by using the Virial mass per length obtained by Fiege and Pudritz (2000a) for a cylindrical filament threaded by a helical magnetic field, Buckle et al. (2012) show that the integral shaped filament in OMC-A is too massive for thermal or turbulent support. Thus, they suggest that the mass and morphology of the integral shaped filament (a small region within the OMC-A map) is consistent with a Virial model of a filamentary cloud threaded by a helical magnetic field.

In the CMC (Figure 3.9) and PMC (Figure 3.5), a first glance at the data seems to suggest

the presence of a helical magnetic field. In the CMC this holds true even if I only use the data in Table 3.5 (with error bars less than 100% of the B_{LOS} value). In the PMC, if I only use the data in Table 3.7, on the north side of the cloud the remaining points are primarily towards us, but there are too few observations on the southern side of the cloud to truly infer anything about the magnetic field geometry.

The helical magnetic field geometry is also predicted or investigated by a number of numerical simulations or theoretical analysis (Shibata and Matsumoto 1991; Fiege and Pudritz 1999, 2000*a,b,c*; Schleicher and Stutz 2018; Nakamura et al. 1993; Matsumoto et al. 1994; Hanawa et al. 1993). Shibata and Matsumoto (1991) study the entire Orion Cloud Complex ($\simeq 100$ pc) and find in their simulations that helically twisted magnetic flux tubes are generated. In addition, Fiege and Pudritz (2000*a*) and Fiege and Pudritz (2000*b*) study the fragmentation length-scale, stability, density profile, and mass per length of filamentary MCs, and based on observational constraints, they suggest that many filamentary clouds are likely wrapped by helical magnetic fields.

Additional observations with improved sensitivity and an increased number of RM data points would be required to better map the B_{LOS} morphology in these MCs and confirm or reject the suggestion of helical magnetic field structure. Such observations should be possible with the new/next generation radio telescope facilities (e.g., LOFAR, SKA). In addition, simulations of MCs with the sizes and physical characteristics of the OMC-A and CMC are required to theoretically connect the results in this chapter to the presence of helical fields.

A visual comparison of my results with those of Planck (Planck Collaboration et al. (2016)) suggests that the data are consistent with a helical or toroidal field wrapping the cloud. I will investigate the 3D structure of the magnetic field in this region by comparing these two data sets in a more quantitative fashion in Chapter 4.

I should note that this technique utilises OFF positions that are distributed randomly, based on lowest extinction values, around each cloud. However, it is clear from Figures. 3.1 and 3.2 that the pattern of a sign change from one side of a cloud to another can sometimes be

seen in the raw RM data itself. Therefore, to investigate whether the observed magnetic field morphology is a result of large-scale Galactic effects or due to the cloud itself, I repeat my analysis this time choosing OFF positions specific to each side of the cloud. More precisely, to calculate magnetic fields on one side of the cloud, I choose OFF positions that are on the same side. For example, for OMC-A, to calculate the magnetic fields on the left side of the cloud where the RMs are predominantly blue (positive), I select OFF positions that are also on the left side of the cloud. I use the same technique for the right side of the cloud, where the RMs are predominantly red (negative).

I implement this method for OMC-A, CMC, and PMC and find that considering both sides of the cloud separately and obtaining RM_{ref} for each side results in a *maximum* change of 5.7 rad m^{-2} , 14.4 rad m^{-2} , and 26.3 rad m^{-2} from the original RM_{ref} for OMC-A, CMC, and PMC, respectively. For both OMC-A and CMC, this maximum change is within the original value of $\delta(\text{RM}_{\text{ref}})$. Therefore, for these two clouds the original and updated values of RM_{ref} are indistinguishable within the uncertainties. Consequently, the overall magnetic field morphology (i.e., direction reversals) in OMC-A and the CMC is preserved in my obtained maps, with very minor and negligible differences.

In the PMC, the changes in RM_{ref} obtained by using the two sides of the cloud separately are not within the uncertainties. Accordingly, the overall magnetic field morphology in PMC is not preserved and the resultant map does not suggest a magnetic field reversal from one side of the cloud to the other. However, since I do not suggest a particular morphology for this region due to a lack of points on the southern side of the cloud, this does not change my original conclusion.

I believe that the choice of the OFF positions for these clouds does not affect the overall derived magnetic field morphology. The clouds themselves are located at high Galactic latitudes at longitudes towards the Galactic anti-center, but are only 0.5 kpc away. Thus, the Galactic contribution to the RM along the lines of sight will be primarily from the halo, which has an electron density and magnetic field strength each of at least an order of magnitude

less than that for the disk, making the RM contribution at least two orders of magnitude less than what would be expected from a similar path length entirely through the disk. This does not, of course, exclude the possibility of reversals induced by more local phenomena (e.g., supernova remnants), but I have tried to minimise the possible effects of Galactic-scale structure through my choice of clouds.

I also note that using the bilateral method leads to higher standard deviations in RM_{ref} , that is, higher values of $\delta(\text{RM}_{\text{ref}})$, and therefore higher uncertainties in the resultant magnetic field strengths. This is entirely due to the fact that by restricting myself to half the area, I have fewer OFF positions with which to calculate RM_{ref} on each side of the cloud. Consequently, since the original method has smaller error bars and no appreciable difference in the derived overall magnetic field morphology, I believe that my original choice of reference points with random positions around each cloud is the optimum method to use.

It is very likely that in future studies, with more sensitivity, many more RM points will be available to choose from. A larger dataset would provide smaller statistical errors from a sample of location-specific OFF positions. Therefore, with a larger number of RM points to choose from, it may be preferable to produce RM_{ref} s on different sides of the clouds to ensure that one is subtracting out any large-scale contributions from the Galaxy.

3.5.3 Comparison with Previous Measurements: A Word of Caution

As indicated in Hull et al. (2017), the magnetic field strength and orientation may vary significantly as one moves from higher-extinction (small scale) regions to lower-extinction (larger-scale) regions. For this reason, comparisons between Zeeman measurements and my results must be made with caution, since the two might be probing B_{LOS} from different regions in the MCs. For example, in this technique I assume that B_{LOS} is constant in every cloud layer. Thus, in higher extinction regions where we are looking through many cloud layers, I am effectively measuring an average B_{LOS} along the line of sight (since I use the total electron

column density and RM in the MC along the line of sight). In contrast, Zeeman measurements using one particular molecular line tracer may be selectively probing specific regions/depths in the cloud. This may also be why different Zeeman measurements in the high-extinction regions have a large amount of scatter. If different measurements probe different layers, they may also be probing different magnetic field strengths in those layers. In regions with lower extinction, where we are looking through fewer cloud layers, the amount of “smearing” over the line-of-sight should be diminished and we should be more accurately probing the true value of B_{LOS} . Unfortunately, due to the difficulties inherent in the Zeeman measurement technique, there are few Zeeman measurements in the low-column-density regions of MCs against which to compare my results.

Figure 3.10 shows the average of the absolute values of B_{LOS} versus extinction, in bins that are 0.5 magnitudes wide in A_V . The error bars reflect the standard deviation of $|B_{\text{LOS}}|$ in each bin. The figure shows a decrease in $\langle |B_{\text{LOS}}| \rangle$ with A_V , a trend that seems different from that seen in the previous studies (e.g., Li et al. 2015; Tritsis et al. 2015) that explore the magnetic field strength as a function of column density. However, a closer look at Figure 1 of Li et al. (2015) shows that in the extinction range of the data points (1 to 4.5 mag), one cannot find a particular trend within their plotted uncertainties. For extinction magnitudes higher than 4.5 there are only four points available. These points are sources 13 and 14 in OMC-A with A_V of 19.56 mag and 21.47 mag with B_{LOS} of $-23 \pm 38 \mu\text{G}$ and $15 \pm 36 \mu\text{G}$, respectively. The points with A_V higher than 30 are sources 1 and 2 in OMC-B, with an extinction of 37.36 for both, and B_{LOS} of $-119 \pm 25 \mu\text{G}$ and $-129 \pm 28 \mu\text{G}$.

The interpretation of my results in Figure 3.10 should be treated with caution. Since we are looking through many different cloud layers in the highest A_V regions, and each layer may have a different value of B_{LOS} , I am essentially providing an average of B_{LOS} through the cloud. This averaging effect may artificially suppress the measured value of B_{LOS} in the highest-column-density regions, less than that in the low-column-density regions where there are fewer layers over which to average.

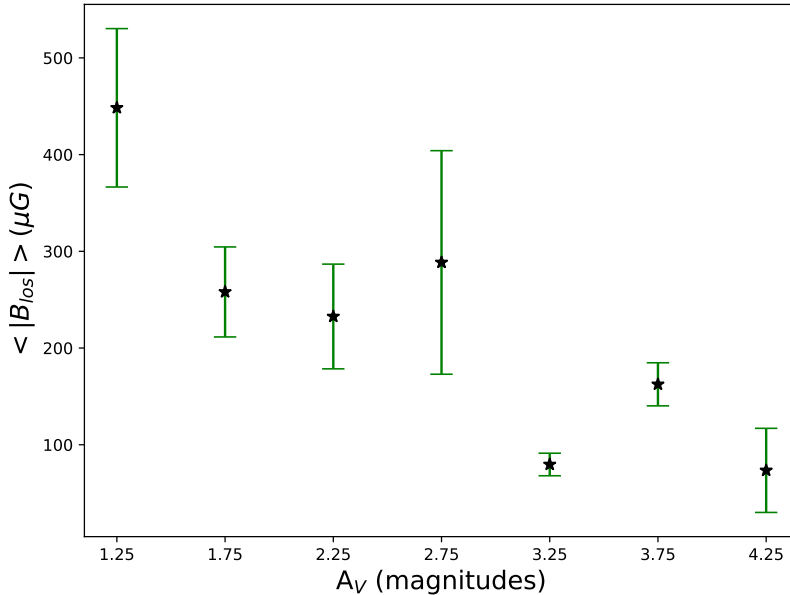


Figure 3.10: The average of absolute value of B_{LOS} versus extinction, in bins that are 0.5 magnitudes wide in A_V . The error bars reflect the standard deviation of B_{LOS} in each bin. In these data, the average B_{LOS} appears to decrease with A_V .

3.6 Conclusions

I present a new method to measure the line-of-sight magnetic field (B_{LOS}) in molecular clouds. This technique uses the rotation measures of polarised sources from the catalog of Taylor et al. (2009) that are located behind and nearby molecular clouds. Using these rotation measures, along with an estimate of electron density determined from extinction maps from Kainulainen et al. (2009) and a chemical model, I estimate B_{LOS} in and around molecular clouds.

I apply my method to four test clouds: the Orion A & B cloud complexes, the California molecular cloud, and the Perseus molecular cloud and find good agreement for B_{LOS} (both in magnitude and direction) with estimates from a limited number of Zeeman measurements in these same regions. For example, in Orion A, I calculate $B_{\text{LOS}} = -23 \pm 38 \mu\text{G}$ and $+15 \pm 36 \mu\text{G}$ at two positions near the Zeeman measurements. In the Orion B complex I also find two rotation measure near the reported Zeeman measurements with calculated

$B_{\text{LOS}} = -119 \pm 25 \mu\text{G}$ and $-129 \pm 28 \mu\text{G}$, respectively. In Perseus, my calculated B_{LOS} at a position nearest the Zeeman measurement is $+32 \pm 101 \mu\text{G}$.

The advantage of this method over the traditional Zeeman approach is that we can use the plethora of rotation measures made across the Galaxy to also map the line-of-sight morphology of the magnetic field over large scales in molecular clouds. Using this technique, I find that the large-scale morphology of B_{LOS} in the Orion A complex and the California cloud is suggestive of helical fields wrapping these clouds. Combined with plane-of-the-sky maps of the magnetic field strength and morphology from dust polarisation maps, this technique provides a way to determine the true three-dimensional structure of the magnetic fields in and around molecular clouds.

I believe that my method holds great promise for future studies of the large-scale magnetic field morphology in molecular clouds for two reasons. First, the magnetic field strengths and directions I calculate are in good qualitative agreement with Zeeman measurements. Second, the inference of helical magnetic field geometries holds true even when I only consider positions with error bars small enough that the *direction* of B_{LOS} is fixed.

Table 3.1: Orion A B_{LOS} values. Point numbers are as mapped in Figure 3.7. Negative values indicate magnetic fields pointed away from the observer and positive values are towards the observer. δB s indicate the upper and lower limit uncertainties.

Point Number	RA (°J2000)	Dec (°J2000)	A_V (mag)	RM_{ON} (rad m $^{-2}$)	RM_{MC} (rad m $^{-2}$)	B (μG)	$+\delta B$ (μG)	$-\delta B$ (μG)
1	80.56	-10.96	0.78	0.0	-1.4	-52	883	883
2	81.08	-10.20	1.62	-25.7	-27.1	-284	315	323
3	81.18	-10.15	1.30	-21.3	-22.7	-330	307	307
4	81.25	-7.66	0.99	-41.6	-43.0	-991	620	620
5	81.29	-7.13	1.30	-9.6	-11.0	-159	413	413
6	81.65	-6.57	0.86	-33.1	-34.5	-1035	537	620
7	81.89	-4.62	0.85	76.0	74.6	2327	896	965
8	81.97	-11.14	0.94	29.4	28.0	700	517	463
9	82.48	-4.89	0.90	8.5	7.1	196	558	558
10	82.49	-10.98	0.85	-19.6	-21.0	-647	874	889
11	82.76	-9.55	1.64	7.4	6.0	62	248	223
12	82.89	-7.18	0.83	-36.3	-37.7	-1233	657	612
13	83.81	-5.39	19.56	-13.5	-14.9	-23	38	38
14	83.82	-5.38	21.47	10.9	9.5	15	36	36
15	85.03	-5.22	2.09	81.0	79.6	595	215	215
16	85.13	-10.38	1.81	28.1	26.7	242	265	265
17	85.41	-5.70	1.62	58.9	57.5	607	168	168
18	85.84	-5.04	1.58	45.9	44.5	483	275	275
19	85.98	-10.51	2.43	26.3	24.9	154	121	121
20	86.28	-5.49	3.11	24.1	22.7	104	114	114
21	86.29	-6.58	1.29	-0.3	-1.7	-25	301	301
22	86.31	-5.49	2.84	23.5	22.1	113	119	119
23	86.32	-10.86	1.96	-3.1	-4.5	-37	220	220
24	86.86	-4.30	2.05	13.5	12.1	93	167	167
25	86.86	-4.30	2.05	10.6	9.2	71	157	157
26	86.92	-11.49	0.77	-16.3	-17.7	-676	867	841
27	87.12	-10.56	1.31	8.2	6.8	98	295	295
28	87.18	-4.74	1.15	-19.6	-21.0	-370	456	455
29	87.18	-8.05	1.66	42.6	41.2	418	308	308
30	87.26	-5.04	0.85	-17.4	-18.8	-578	927	926
31	87.61	-6.44	0.91	95.6	94.2	2553	695	698
32	87.88	-7.94	0.77	103.6	102.2	3928	1135	1675
33	87.88	-10.39	2.32	13.3	11.9	78	163	163
34	87.89	-10.38	2.32	28.5	27.1	177	102	102

Table 3.2: Orion A B_{LOS} values, considering only the points that do not change direction within the estimated uncertainties. Point numbers are as mapped in Figure 3.7. Negative values indicate magnetic fields pointed away from the observer and positive values are towards the observer. δB s indicate the upper and lower limit uncertainties.

Point Number	RA (°J2000)	Dec (°J2000)	A _V (mag)	RM _{ON} (rad m ⁻²)	RM _{MC} (rad m ⁻²)	B (μ G)	+ δB (μ G)	- δB (μ G)
3	81.18	-10.15	1.30	-21.3	-22.7	-330	307	307
4	81.25	-7.66	0.99	-41.6	-43.0	-991	620	620
6	81.65	-6.57	0.86	-33.1	-34.5	-1035	537	620
7	81.89	-4.62	0.85	76.0	74.6	2327	896	965
8	81.97	-11.14	0.94	29.4	28.0	700	517	463
12	82.89	-7.18	0.83	-36.3	-37.7	-1233	657	612
15	85.03	-5.22	2.09	81.0	79.6	595	215	215
17	85.41	-5.70	1.62	58.9	57.5	607	168	168
18	85.84	-5.04	1.58	45.9	44.5	483	275	275
19	85.98	-10.51	2.43	26.3	24.9	154	121	121
29	87.18	-8.05	1.66	42.6	41.2	418	308	308
31	87.61	-6.44	0.91	95.6	94.2	2553	695	698
32	87.88	-7.94	0.77	103.6	102.2	3928	1135	1675
34	87.89	-10.38	2.32	28.5	27.1	177	102	102

Table 3.3: Orion B B_{LOS} values. Point numbers are as mapped in Figure 3.8. Negative values indicate magnetic fields pointed away from the observer and positive values are towards the observer. δB s indicate the upper and lower limit uncertainties.

Point Number	RA (°J2000)	Dec (°J2000)	A _V (mag)	RM _{ON} (rad m ⁻²)	RM _{MC} (rad m ⁻²)	B (μ G)	+ δB (μ G)	- δB (μ G)
1	85.44	-1.92	37.36	-44.1	-76.4	-119	25	25
2	85.45	-1.91	37.36	-50.1	-82.4	-129	28	28
3	85.91	-2.95	2.03	82.6	50.3	393	199	199
4	87.09	-1.29	2.84	56.0	23.7	122	125	125
5	88.21	3.22	1.50	91.1	58.8	699	268	268
6	88.92	-1.02	1.50	152.4	120.1	1423	268	263
7	90.09	0.05	1.19	33.9	1.6	27	437	437
8	90.15	-2.74	0.82	53.8	21.5	736	642	670

Table 3.4: California B_{LOS} values. Point numbers are as mapped in Figure 3.9. Negative values indicate magnetic fields pointed away from the observer and positive values are towards the observer. δB s indicate the upper and lower limit uncertainties.

Point Number	RA ($^{\circ}$ J2000)	Dec ($^{\circ}$ J2000)	A_V (mag)	RM_{ON} (rad m^{-2})	RM_{MC} (rad m^{-2})	B (μG)	$+\delta B$ (μG)	$-\delta B$ (μG)
1	58.30	38.45	2.52	46.6	42.6	278	141	141
2	58.63	41.91	0.90	-56.5	-60.5	-2106	1070	1070
3	58.92	41.90	1.10	-7.5	-11.5	-255	539	539
4	59.31	37.96	2.66	44.5	40.5	249	147	147
5	59.60	41.87	1.81	-20.2	-24.2	-241	213	213
6	59.75	40.05	1.02	24.9	20.9	541	615	615
7	59.76	40.03	0.94	26.5	22.5	697	881	881
8	59.87	41.78	2.45	12.9	8.9	60	228	228
9	60.03	40.20	1.24	28.1	24.1	431	404	404
10	60.19	37.80	1.16	73.0	69.0	1373	355	355
11	60.54	41.51	2.88	-16.5	-20.5	-116	130	131
12	60.92	38.33	2.06	7.1	3.1	26	255	255
13	61.89	39.42	0.98	-3.4	-7.4	-210	701	701
14	62.03	41.28	1.16	-2.4	-6.4	-129	637	637
15	62.03	40.38	2.35	21.8	17.8	126	144	144
16	62.14	41.56	0.98	-2.4	-6.4	-180	669	669
17	62.24	36.59	0.93	59.1	55.1	1761	827	826
18	62.34	38.81	2.07	56.0	52.0	430	138	138
19	63.69	36.04	0.69	55.4	51.4	4160	3259	3438
20	64.47	35.28	1.16	34.8	30.8	614	394	394
21	64.57	38.01	3.55	-24.2	-28.2	-131	119	119
22	64.62	38.04	3.05	-13.7	-17.7	-94	175	175
23	65.06	38.83	1.37	27.3	23.3	348	384	384
24	65.33	35.19	0.78	31.5	27.5	1402	1799	1799
25	65.39	38.61	1.73	5.1	1.1	11	259	259
26	65.61	39.93	1.08	-17.4	-21.4	-495	656	656
27	65.97	34.86	0.78	41.0	37.0	1925	1257	1257
28	66.09	39.35	1.76	-26.4	-30.4	-313	189	190
29	66.10	39.37	1.76	-18.0	-22.0	-226	286	286
30	66.77	36.06	2.32	-21.2	-25.2	-181	214	214
31	66.92	38.39	1.47	-3.6	-7.6	-102	360	360
32	67.98	34.94	1.69	-44.4	-48.4	-529	240	240
33	68.28	35.84	2.17	-24.2	-28.2	-220	171	171
34	68.77	36.78	2.12	-14.0	-18.0	-145	227	227
35	68.87	35.25	1.63	-17.6	-21.6	-248	268	268

Table 3.5: California B_{LOS} values, considering only the points that do not change direction within the estimated uncertainties. Point numbers are as mapped in Figure 3.9. Negative values indicate magnetic fields pointed away from the observer and positive values are towards the observer. δB s indicate the upper and lower limit uncertainties.

Point Number	RA (°J2000)	Dec (°J2000)	A_V (mag)	RM_{ON} (rad m^{-2})	RM_{MC} (rad m^{-2})	B (μG)	$+\delta B$ (μG)	$-\delta B$ (μG)
1	58.30	38.45	2.52	46.6	42.6	278	141	141
2	58.63	41.91	0.90	-56.5	-60.5	-2106	1070	1070
4	59.31	37.96	2.66	44.5	40.5	249	147	147
5	59.60	41.87	1.81	-20.2	-24.2	-241	213	213
9	60.03	40.20	1.24	28.1	24.1	431	404	404
10	60.19	37.80	1.16	73.0	69.0	1373	355	355
17	62.24	36.59	0.93	59.1	55.1	1761	827	826
18	62.34	38.81	2.07	56.0	52.0	430	138	138
19	63.69	36.04	0.69	55.4	51.4	4160	3259	3438
20	64.47	35.28	1.16	34.8	30.8	614	394	394
21	64.57	38.01	3.55	-24.2	-28.2	-131	119	119
27	65.97	34.86	0.78	41.0	37.0	1925	1257	1257
28	66.09	39.35	1.76	-26.4	-30.4	-313	189	190
32	67.98	34.94	1.69	-44.4	-48.4	-529	240	240
33	68.28	35.84	2.17	-24.2	-28.2	-220	171	171

Table 3.6: Perseus B_{LOS} values. Point numbers are as mapped in Figure 3.5. Negative values indicate magnetic fields pointed away from the observer and positive values are towards the observer. δB s indicate the upper and lower limit uncertainties.

Point Number	RA ($^{\circ}$ J2000)	Dec ($^{\circ}$ J2000)	A_V (mag)	RM_{ON} (rad m^{-2})	RM_{MC} (rad m^{-2})	B (μG)	$+\delta B$ (μG)	$-\delta B$ (μG)
1	50.01	29.69	2.62	59.2	28.1	194	176	176
2	50.01	31.13	1.27	89.6	58.5	1229	457	624
3	50.15	30.72	3.50	40.1	9.0	47	128	116
4	51.29	31.48	2.34	35.1	4.0	32	101	101
5	51.80	29.02	1.75	26.2	-4.9	-57	268	269
6	51.91	31.40	2.87	15.1	-16.0	-100	157	158
7	52.03	29.44	1.16	18.9	-12.2	-310	530	537
8	52.15	29.37	2.32	24.8	-6.3	-50	103	106
9	52.17	30.83	4.21	60.2	29.1	134	67	67
10	52.54	30.55	3.75	-8.3	-39.4	-196	109	109
11	52.54	28.65	1.37	6.5	-24.6	-441	339	338
12	52.61	30.06	0.64	28.1	-3.0	-238	1351	1363
13	52.92	28.68	1.89	19.9	-11.2	-118	246	253
14	53.17	31.86	1.50	67.4	36.3	557	488	359
15	53.57	31.20	4.09	28.2	-2.9	-13	88	88
16	53.88	30.54	2.11	22.2	-8.9	-80	146	147
17	54.13	32.31	1.03	34.3	3.2	113	435	443
18	54.41	32.13	0.92	175.4	144.3	7160	1121	4585
19	54.46	31.25	2.42	110.8	79.7	605	207	211
20	54.47	30.93	3.08	48.7	17.6	103	83	81
21	54.91	32.91	2.03	126.8	95.7	904	291	256
22	55.04	32.15	2.69	200.0	168.9	1137	466	103
23	55.52	30.34	1.25	19.2	-11.9	-257	473	475
24	55.81	31.25	3.47	39.9	8.8	46	94	94

Table 3.7: Perseus B_{LOS} values, considering only the points that do not change direction within the estimated uncertainties. Point numbers are as mapped in Figure 3.5. Negative values indicate magnetic fields pointed away from the observer and positive values are towards the observer. δB s indicate the upper and lower limit uncertainties.

Point Number	RA ($^{\circ}\text{J}2000$)	Dec ($^{\circ}\text{J}2000$)	A_V (mag)	RM_{ON} (rad m^{-2})	RM_{MC} (rad m^{-2})	B (μG)	$+\delta B$ (μG)	$-\delta B$ (μG)
1	50.01	29.69	2.62	59.2	28.1	194	176	176
2	50.01	31.13	1.27	89.6	58.5	1229	457	624
9	52.17	30.83	4.21	60.2	29.1	134	67	67
10	52.54	30.55	3.75	-8.3	-39.4	-196	109	109
11	52.54	28.65	1.37	6.5	-24.6	-441	339	338
14	53.17	31.86	1.50	67.4	36.3	557	488	359
18	54.41	32.13	0.92	175.4	144.3	7160	1121	4585
19	54.46	31.25	2.42	110.8	79.7	605	207	211
20	54.47	30.93	3.08	48.7	17.6	103	83	81
21	54.91	32.91	2.03	126.8	95.7	904	291	256
22	55.04	32.15	2.69	200.0	168.9	1137	466	103

Chapter 4

The 3D Magnetic Field in Orion A

The contents of this chapter will be published as:

Tahani, M., Plume, R., Brown, J. C., Kainulainen, J., & Soler, J. (2019), ‘Bow Magnetic Morphology? 3D Magnetic Field Structure in Orion-A’, in prep

In this Chapter, I investigate the large-scale 3D magnetic field in Orion A (the entire southern complex). For this purpose I use Planck Collaboration et al. (2016, hereafter PXXXV) dust polarisation data and my B_{LOS} results (Tahani et al. 2018, here forward TPBK18). I discuss each of these datasets in Section 4.2 and describe my methodology to couple these two magnetic fields results in Section 4.3. Finally, I discuss our results and interpretation. The goals of Chapter 3 and this chapter are to provide a new method to obtain the large-scale structure of B_{LOS} around star-forming MCs using rotation measures and to describe a method to combine existing dust-polarisation measurements with B_{LOS} to investigate the 3D morphology of these fields. The intent is to show what can be done with the existing data, as well as set the stage for future, higher sensitivity RM catalogs - such as those which will be obtained by POSSUM¹ and VLASS².

¹<http://www.dunlap.utoronto.ca/~askap.org/possum/>

²<https://science.nrao.edu/science/surveys/vlass/vlass>

4.1 Introduction

Probing the three dimensional field morphology requires either combining the individual measurements (Zeeman splitting, Faraday rotation, and dust polarisation technique) or developing a new technique. Recently Chen et al. (2018) proposed obtaining the 3D magnetic field morphology using dust polarisation observations, based on the statistical properties of the observed polarisation fraction. Another technique to obtain the 3D magnetic field in star-forming regions involves combining dust polarisation data, Zeeman measurements, and ion-to-neutral molecular line width ratio measurements (Houde et al. 2002). However, due to a degeneracy between the inclination angle and the strength of B_{POS} and ambiguity in the direction of B_{POS} , Li and Houde (2008) and Houde (2011) suggested that this technique cannot be widely used. The method described in Chapter 3 allows for wider exploration of B_{LOS} . Future surveys, which will use next generation radio telescopes, hold the promise of even larger surveys and with much more sensitive measurements of Rotation Measures.

Three magnetic field morphologies that can explain the direction-change of B_{LOS} across filamentary structures observed in Chapter 3 are toroidal, helical, and bow morphologies. The *helical/toroidal* morphology has been investigated in a number of theoretical studies (e.g., Shibata and Matsumoto 1991; Nakamura et al. 1993; Hanawa et al. 1993; Matsumoto et al. 1994; Fiege and Pudritz 2000a,b; Schleicher and Stutz 2018; Reissl et al. 2018).

Heiles (1997) proposed an alternative explanation, which associates the magnetic reversal in Orion A to the Eridanus shock and its interaction with the dense MC. In this mechanism the magnetic fields bend around the Orion MC, as illustrated in Figure 4.1. The ambient Galactic B_{LOS} in this region is, in general, towards the observer and interacts with the superbubble, generating the reversal. Heiles (1997) suggests that a reversal in this region can be observed even without the presence of a MC, however, the existence of a MC in this region makes this reversal sharper. This proposal is strengthened based on Observations by Soler et al. (2018), who map B_{POS} lines in the Orion-Eridanus super-bubble and suggest that due to the large-scale shape of the magnetic field lines, B_{POS} is influenced by the Eridanus

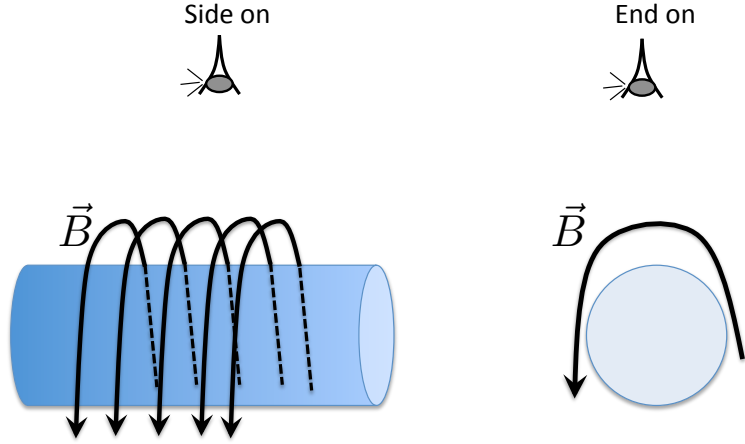


Figure 4.1: Wrapping of magnetic fields lines around a cylindrical filamentary structure (gray circle), as seen by the observer. This concept could provide an explanation for the observations seen in Orion A, interacting with the Orion-Eridanus superbubble. The magnetic field line is represented as the curved black line.

superbubble and interacts with it.

I refer to this morphology, regardless of how it is formed, as a *bow* morphology. This general morphology has been recently investigated in some theoretical studies (Gómez et al. 2018; Inoue et al. 2018; Reissl et al. 2018), as well as observational studies (Liu et al. 2018), and has been also referred to as a U-shape or a pinched field. A *toroidal* morphology is a specific case of helical morphology in which the helix pitch angle is taken to be zero. This has been recently investigated by Reissl et al. (2018). Therefore, the toroidal and helical morphologies are actually the same model.

Understanding the overall 3D magnetic field morphology, and consequently identifying which of these proposed magnetic configurations are responsible for the observed magnetic

field reversals, can potentially help us answer questions pertaining to the role of magnetic fields in star formation. For example, helical fields can allow for more mass accumulation in the filamentary structure by stabilizing the cloud against self gravity (Buckle et al. 2012). Additionally, since the magnetic fields must form closed loops, determining the 3D magnetic field morphology in, and around, these filaments can provide significant information regarding the influence that the surrounding environment has on the formation and evolution of filamentary structure.

4.2 Observations

For the parallel component of the magnetic field (B_{LOS}) I use the directions and magnitudes I found from Chapter 3. In this chapter I consider only the magnetic field around Orion A and use the B values with the smallest error bars in Chapter 3 (i.e. with errors $< 100\%$ so that the direction of the field is well determined). Figure 4.2 shows all the data points determined in Chapter 3. Points 3, 4, 6, 7, 8, 12, 15, 17, 18, 19, 29, 31, 32, and 34 in this figure have errors less than 100%. Points 4, 6, 12, 15, 17, 18, and 29, are considered in this study, since these are relatively close to the filament.

For the plane-of-sky component (B_{POS}), I use the PXXXV determination of the magnetic field orientation as projected on the plane of the sky. These magnetic field lines are determined from the thermal emission of interstellar dust observed by Planck³ at 353 GHz taken at an original resolution of $4'.8$ and then smoothed with a $15'$ FWHM Gaussian beam.

In their Table D.1., PXXXV report two average B_{POS} values for the entire Orion complex, using the two methods of Davis-Chandrasekhar-Fermi (DCF) and DCF plus the structure function (DCF+SF) method described by Hildebrand et al. (2009). Even though these values do not represent B_{POS} magnitude for each data point of TPBK18 Orion A map, the B_{POS}

³https://www.esa.int/Our_Activities/Space_Science/Planck

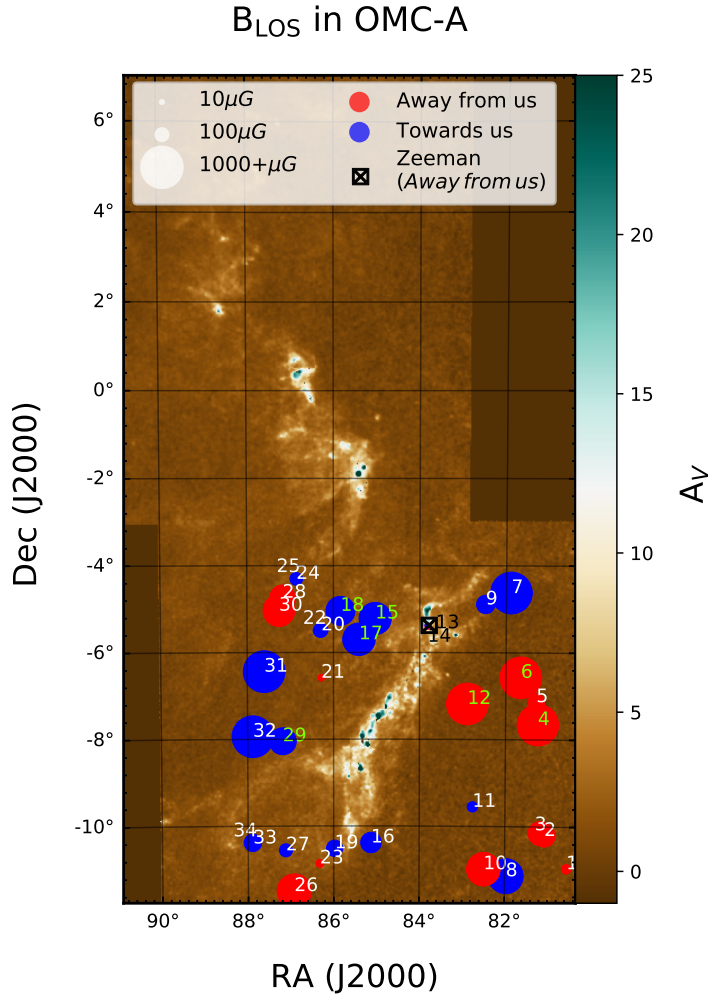


Figure 4.2: B_{LOS} in Orion A. Blue (red) circles show magnetic fields toward us (away from us). The size of the circles indicate the magnitude of magnetic field. Sources numbered in light green indicate the sources used for this study. Black square shows the location of the available Zeeman measurements. Color image is the extinction map (A_V). Points 3, 4, 6, 7, 8, 12, 15, 17, 18, 19, 29, 31, 32, and 34 in this figure have errors less than 100%. Points 4, 6, 12, 15, 17, 18, and 29 are considered in this study.

direction at each point is determined from the Stokes parameters at that point.

4.3 Methodology

To investigate the validity of the different interpretations, I first constructed 3D magnetic field vectors from the available observations. Then, I modeled expected magnetic field results based on the different proposed geometries and compared the values to the observations.

4.3.1 Constructing the 3D Magnetic Field Vectors

In order to construct 3D magnetic field vector estimates, we need to find a B_{POS} that can be combined with the B_{LOS} points from TPBK18. I do this by finding the closest PXXXV B_{POS} to the B_{LOS} points. If no B_{POS} value exists within $15'$ (the size of the smoothed Planck polarisation beam) of the B_{LOS} point, I discard that point from the analysis, which also means that the B_{LOS} data point is too far from the filament (points 3, 4, 8, 19 in Figure 4.2). Points 31 and 7 are also too far away from the filament axis. Therefore, I carry out this study with points numbered 6, 8, 12, 15, 17, 18, and 29, as indicated by light green numbers in Figure 4.2.

After finding the closest B_{POS} location, I calculate the orientation of B_{POS} and its strength using the PXXXV average value. To find the orientation, I first find the polarisation angle using:

$$\psi = \frac{1}{2} \arctan(-U, Q), \quad (4.1)$$

where ψ is the polarisation angle, and U and Q are the Stokes parameters obtained from Planck observations by dust thermal radiation. I add a $\pi/2$ to ψ to account for the fact that the magnetic field orientation is orthogonal to the polarisation angle as explained in Chapter 2. Thus, I define the magnetic angle $\phi = \psi_{eq} + \pi/2$, where ψ_{eq} is the polarisation angle found in the equatorial coordinate. The components of the magnetic field along the Right Ascension and Declination axis are $|B_{RA}| = |B_{\text{Planck}} \sin \phi|$ and $|B_{Dec}| = |B_{\text{Planck}} \cos \phi|$

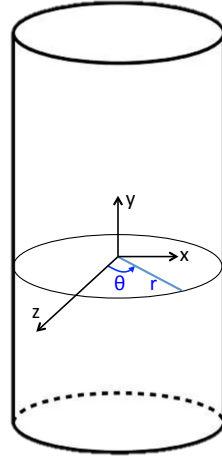


Figure 4.3: Geometry and coordinates for a filament. The x-axis is radial to the filament, and in the plane of the sky, y-axis is parallel to the long axis of the filament, and z-axis is radial, towards the observer.

respectively. I take the magnitude of each point to be fixed to that determined for the average of the entire region, $B_{Planck} = 38 \pm 14 \mu\text{G}$ (from Table D.1. in PXXXV).

To analyze the 3D geometry of the magnetic field with respect to the filament itself, I take the frame of reference such that the x-axis is radial to the filament, and in the plane of the sky, y-axis is parallel to the long axis of the filament, and z-axis is radial, towards the observer, as illustrated in Figure 4.3. We can then write the magnetic field vector at each point in this frame of reference as $\mathbf{B} = (B_x, B_y, B_z)$. Compared to the equatorial system, this new frame of reference is rotated by ξ , where ξ is the angle the filament's minor axis makes with decreasing RA axis, i.e. the orientation of the x-axis of the filament with respect to the East-West (Right Ascension) direction of the map measured in a clockwise direction as illustrated in Figure 4.4. In this system, $|B_x| = |B_{Planck} \cos(\xi + \phi)|$ and $|B_y| = |B_{Planck} \sin(\xi + \phi)|$, where ϕ is the magnetic angle in the plane of the sky. The equations are cast as absolute values because we do not yet have any information regarding the positive/negative signs of B_x and B_y which provide the direction of B_{POS} (i.e. the North-South orientation of the magnetic field). $B_z = B_{LOS}$ and does include the positive and negative signs of B_{LOS}.

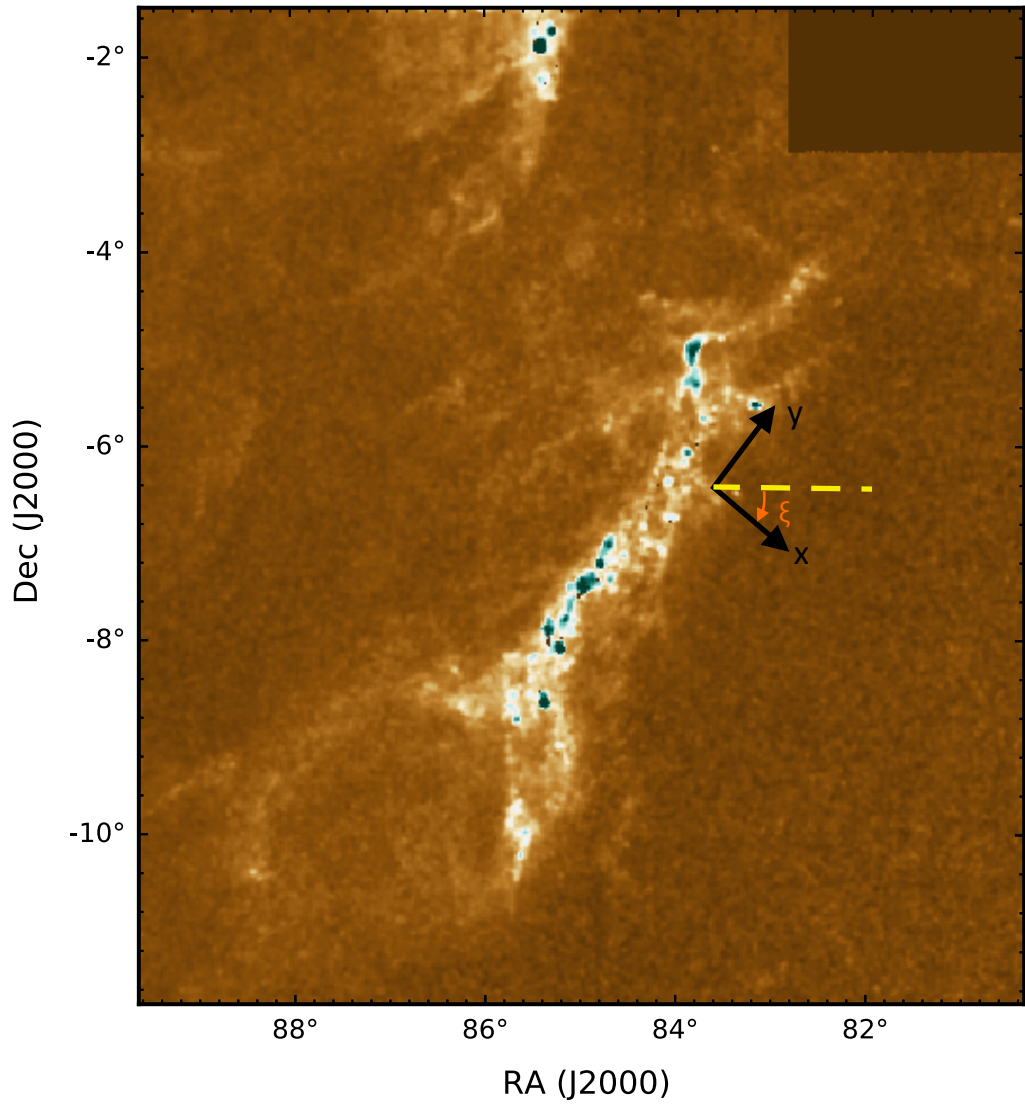


Figure 4.4: Coordinate system of a filament compared to the standard equatorial system. Compared to the equatorial system, the filament's frame of reference is rotated by ξ , where ξ is the angle the filament's minor axis makes with decreasing RA axis, i.e. the orientation of the x-axis of the filament with respect to the East-West (Right Ascension) direction of the map measured in a clockwise direction.

To construct the full 3D vectors, we need to account for the positive or negative signs of B_x and B_y , which give us the direction of BPOS, rather than just its angle. While the *orientation* of BPOS can be identified from the Stokes parameters, the actual *direction* (+ or – along that orientation) cannot be determined. Figure 4.5 demonstrates the ratio of the observed magnetic field components (i.e. B_x , B_y , B_z) to the total estimated observed magnetic field strength ($B_{total} = \sqrt{B_x^2 + B_y^2 + B_z^2}$), in the Cartesian frame shown in Figure 4.3, as explained in Section 4.3.1. To distinguish between morphologies, I compare these observed magnetic field strengths to those predicted by my three models as described in sections below.

4.3.2 Modeling a Toroidal and a Helical 3D Magnetic Field

I model a filament with a simple toroidal or a helical magnetic field using the following set of equations:

$$\begin{aligned} B_x &= \frac{B_0 R \cos(\theta)}{r^\alpha} = \frac{B_0 R z}{(x^2 + z^2)^{\frac{\alpha+1}{2}}}, \\ B_y &= \frac{B_1 R}{r^\alpha} = \frac{B_1 R}{(x^2 + z^2)^{\frac{\alpha}{2}}}, \\ B_z &= \frac{-B_0 R \sin(\theta)}{r^\alpha} = \frac{-B_0 R x}{(x^2 + z^2)^{\frac{\alpha+1}{2}}}, \end{aligned} \quad (4.2)$$

where the x, y, and z directions follow the convention set in Section 4.3.1 and Figure 4.3. R is a scaling factor with units of [length] $^\alpha$ and $r = \sqrt{x^2 + z^2}$ - the radial distance from the filament mid-plane in the X-Z plane (i.e. perpendicular to the long axis). B_0 and B_1 carry information about the strength of the toroidal and poloidal components of magnetic field respectively. The parameter α reflects the rate at which the magnetic field strength decreases with distance from the filament.

To have a purely toroidal magnetic field, or a helix with a small pitch angle, B_1 needs to be either zero or very small compared to B_0 . In these equations, $\frac{x}{(x^2+z^2)^{1/2}}$ and $\frac{z}{(x^2+z^2)^{1/2}}$ replace $\sin \phi$ and $\cos \phi$.

R arises from the relation between the strength of the magnetic field and its distance

from the filament, in order to make the units of both sides of this relation identical (in units of magnetic strength). Since R is a free parameter of the total strength of the magnetic field, it is carried along similarly into each of the x, y , and z components.

To understand the rationale behind the magnetic strength decreasing with $1/r^\alpha$, I consider a) the observed density profile for the Orion A filament, b) the relation between magnetic field and MC density, and c) the necessity to keep the magnetic field divergence-free. The relationship between the magnetic field strength and the gas density has been investigated both theoretically and observationally. Theoretically, Tritsis et al. (2015) find that $B(\rho) \propto \rho^{1/2}$ is preferred, where $B(\rho)$ is the magnetic field as a function of the mass volume density and ρ is the mass volume density. Observationally, Crutcher et al. (2010) propose a ratio of $B(\rho) \propto \rho^{2/3}$ for when the magnetic energy is small compared to the effects of gravity. In these models I consider both $B(\rho) \propto \rho^{1/2}$ and $B(\rho) \propto \rho^{2/3}$. The density profile of the Orion A filament has also been studied both observationally and theoretically and is proposed to have a plummer-like form (Salji et al. 2015). The standard Plummer profile is described by:

$$\rho(r) = \frac{\rho_c}{[1 + (r/r_{flat})^2]^{p/2}}, \quad (4.3)$$

where ρ_c is the central density of the filament, r is the distance (radius) from the filament axis, and r_{flat} is the characteristic radius defining the central region, where the density profile flattens. The exponent p is observationally determined and sets the density drop-off rate.

However, I use the more recently defined density profile suggested by Stutz and Gould (2016, see their equation 5), where they suggest that $\rho(r) \propto r^{-13/8}$. This density profile not only fits the observations, it also keeps the magnetic field divergence-free (i.e. $\frac{\partial B_x}{\partial x} + \frac{\partial B_y}{\partial y} + \frac{\partial B_z}{\partial z} = 0$ in Equation 4.2). Combining $B(\rho)$ with $\rho(r)$, I obtain a relation for $B(r)$ in which the magnetic field strength decreases as $1/r^\alpha$, where α can be either $13/16$ or $13/12$ depending on whether I use the Tritsis et al. (2015) or the Crutcher et al. (2010) relations.

4.3.3 Modeling a Bow Magnetic Field Morphology

The simplest divergence-free magnetic field relation one can use to describe a bow morphology is:

$$\begin{aligned} B_x &= B_1, \\ B_y &= B_2, \\ B_z &= B_0 \frac{x}{R'}, \end{aligned} \tag{4.4}$$

B_0 , B_1 , and B_2 are free parameters with positive values which illustrate the strength of magnetic field. R' is a free parameter with a unit of length to ensure that the relation for the z-component of magnetic field in equation 4.4 at both sides have the same units. I take the R' value to be close to half of the distance of point 17 from the filament axis, which is equal to the integration distance (see Section 4.3.4). B_x and B_y remain constant and in the direction of the ambient magnetic field, whereas B_z reverses in direction from one side of the filament to the other.

This set of equations is the simplest form that represents a reversal of B_z across the filament, from $+x$ to $-x$ (from one side of the filament to the other), and is divergence-free at the same time. To have a divergence-free field, B_x and B_y remain constant in the direction of the ambient magnetic field, whereas B_z reverses in direction from one side of the filament to the other. Therefore, B_z varies with x to represent this change of direction across the filament. In addition, we need to keep in mind that these equations represent single magnetic field lines. If we follow one field line as it wraps around a filament, we will see that the z-component (towards the observer) of the field is zero directly in front of, and behind, the filament. As we increase the radial distance from the filament (x-direction), the z-component will become larger and will, eventually, reach 100% of the magnetic field strength when the field line is pointed directly towards the observer. Thus, this relation of B_z with x also represents the wrapping of the field lines around the filament. Due to this increase in B_z strength and the fact that these equations do not necessarily form closed loops, I only use these equation to represent the magnetic field strength in a regions close to the filament. Therefore, I assume

this region is where the filament interacts with the Orion-Eridanus superbubble and that it encompasses all of the data points indicated in light green on Figure 4.2.

Based on the hypothesis proposed by Heiles (1997), I assume that the magnetic field values from the observations represent the field lines that do not penetrate the dense filamentary structure and therefore they actually represent the ambient field lines and thus I do not expect them to increase as we get closer to the filament. Therefore, I make the following assumptions: 1) in the above set of equations for the bow model, the overall magnetic field strength does not decrease with distance and 2) $B_1 = B_2$ represents the ambient magnetic field. I only explore different ratios of B_0 and B_1 (see Section 4.5).

If we forgo the $\nabla \cdot \mathbf{B} = 0$ requirement, we can use the equations provided by Reissl et al. (2018), which illustrates the bow morphology in a different manner:

$$\begin{aligned} B_x &= \frac{B_0(x, z)}{1 + U^2(x, z)}, \\ B_y &= 0, \\ B_z &= \frac{B_0(x, z)U(x, z)}{1 + U^2(x, z)}, \end{aligned} \tag{4.5}$$

with

$$\begin{aligned} U(x, z) &= -5x(2 - z)^2 e^{-8x^2}, \\ B_0(x, z) &= \frac{B_0}{(1 + (r/r_{flat})^2)^{-0.6\beta}}; \quad r = \sqrt{x^2 + z^2}. \end{aligned} \tag{4.6}$$

r_{flat} is the characteristic radius of the plummer-like density profile where the profile becomes flat close to the center of the filamentary structure. The parameter β controls the slope of the density at the outer regions. Reissl et al. (2018) use $\beta = 1.6$, which is the average value of β from Arzoumanian et al. (2011) density profile. B_0 controls the total strength of the magnetic field.

4.3.4 3D Magnetic Fields: Observed versus Modeled

Since the observed magnetic field values are all averaged along the line of sight (LOS), I first find the average magnetic field values along the LOS for each component in each of the models separately using

$$\langle B_i \rangle (x/L) = \frac{\int_{-\frac{L}{2}}^{+\frac{L}{2}} B_i(x, z) dz}{L}, \quad (4.7)$$

where L is the integration length along the LOS and i indicates x, y, or z components. Therefore, $\langle B_i \rangle (x/L)$ is the average value of the x, y, or z component of the magnetic field at a radial distance of x from the filament long axis (the y-axis), and averaged over the line-of-sight distance of L. $B_i(x, z)$ is the magnetic field components from each models in equations 4.2, 4.4, and 4.5. Thus, equation 4.7 provides $\langle B_x \rangle$, $\langle B_y \rangle$, and $\langle B_z \rangle$ as a function of x (perpendicular distance to the filament axis) and L (integration path). I explore these averages as a function of x/L to avoid the need to convert x and L to real distances.

To compare the models with the observed values, I first associate the major axis of the cylinder with the filamentary structure. This axis represents a line connecting the sky coordinates of (RA, Dec) = (82.3°, -4.15°) and (88.0°, -10.8°). I then find the perpendicular distance of each of the light green labeled points in Figure 4.2 from this line (i.e the distance from the filament axis).

I take the integration distance (L) to be half of the distance of the point 17 from the filament axis, because I assume this distance represents the MC's thickness along the LOS. One should note that we do not require the actual integration distance in finding the observed B_{LOS} values since I use the column density values in Chapter 3 instead of the volume densities. Information about the line-of-sight integration distance is already embedded in the column densities.

Additionally, in order to compare the models to each other and to the observed data, after finding the averages along the LOS, I find the ratio of each component to the total (averaged along the LOS) magnetic field in each model and in the observational data, i.e.

$(\frac{\langle B_x \rangle}{\langle B_{total} \rangle}, \frac{\langle B_y \rangle}{\langle B_{total} \rangle}, \frac{\langle B_z \rangle}{\langle B_{total} \rangle})$, where $B_{total} = \sqrt{\langle B_x \rangle^2 + \langle B_y \rangle^2 + \langle B_z \rangle^2}$, in each model.

These represent the ratios that should be observed ideally without experimental uncertainties and systematic observing biases.

We can then compare the observed magnitudes of the field components with those of the models in order to determine which model is most consistent with the observed data. I perform this analysis in Section 4.4. For this purpose, I need to investigate the χ^2 values for each model using different values for the free parameters.

To find the χ^2 values, I use the following relation for each component of the magnetic field.

$$\chi_j^2 = \sum_{i=1}^N \frac{\left(\text{observed } \frac{\langle B_j \rangle}{\langle B_{tot} \rangle} - \text{modeled } \frac{\langle B_j \rangle}{\langle B_{tot} \rangle} \right)_i^2}{\sigma_i^2}, \quad (4.8)$$

where j can be x , y , or z . N is the number of observational points in the study (in this case $N = 7$). The observed $\frac{\langle B_j \rangle}{\langle B_{tot} \rangle}$ is the observed values of each component of magnetic field to the total magnetic field as plotted in Figure 4.5. The modeled $\frac{\langle B_j \rangle}{\langle B_{tot} \rangle}$ is the average along the LOS of each model as explained in Section 4.3.4. I should note that the observational uncertainties are taken into account when finding the χ^2 values. In cases like the helical model where the free parameters of R and B_1/B_0 do not cancel out after taking the ratios, I calculate the χ^2 over a range of free parameters.

4.4 Results of Modeling

Using the methodology described in Section 4.3, I find the 3D vectors. Figure 4.6 shows the $\mathbf{B} = (B_x, B_y, B_z)$ vectors for the points in Figure 4.2. The blue (red) colors show the vectors with their LOS component towards (away from) the observer. The figure shows that B_z values dominate. As discussed in Section 4.3.1, to plot the 3D vectors one also needs to have a direction for \mathbf{B}_{POS} . In this figure I assume that the direction of the field lines on one side of

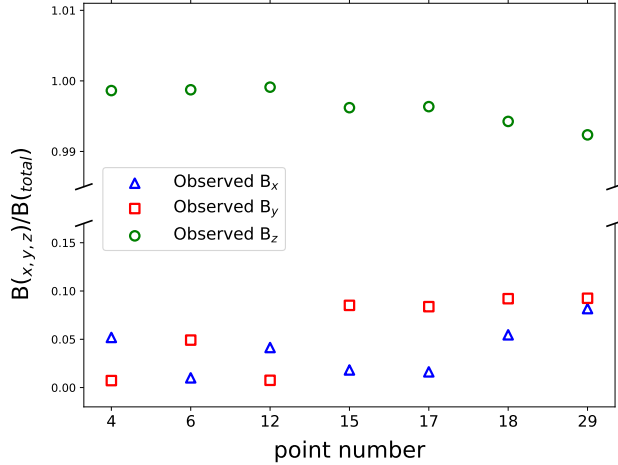


Figure 4.5: Observed B_x , B_y , and B_z using the frame system depicted in Figure 4.3 as well as B_{POS} and B_{LOS} values obtained by PXXXV and Chapter 3, respectively. The y-axis shows the ratio of each component of magnetic field to the total value and the x-axis refers to the numbered data points labeled in Figure 4.2.

the filament point towards the filament, and point away from the filament on the other side (i.e. that the plane-of-sky component of the magnetic field does not change direction across the filament). This assumption is reasonable since magnetic fields must be divergence free, resulting in field lines that are continuous and form closed paths. Additionally, to map the 3D vectors in Figure 4.6, since the observed values of B_{LOS} and B_{POS} are averaged along the entire line-of-sight, I make the simplifying assumption that the observed magnetic field arises from a single depth that I take to be the mid-plane of the Orion A filament.

To distinguish between morphologies, I carry out the analysis described in Section 4.3.4 and compare the observed magnetic field strengths to those predicted by my three models. Figure 4.5 demonstrates the ratio of the observed magnetic field components (i.e. B_x , B_y , B_z) to the total estimated observed magnetic field strength ($B_{\text{total}} = \sqrt{B_x^2 + B_y^2 + B_z^2}$), in the Cartesian frame shown in Figure 4.3, as explained in Section 4.3.1. Subsequently, I study the result from each model to compare them with these observed values.

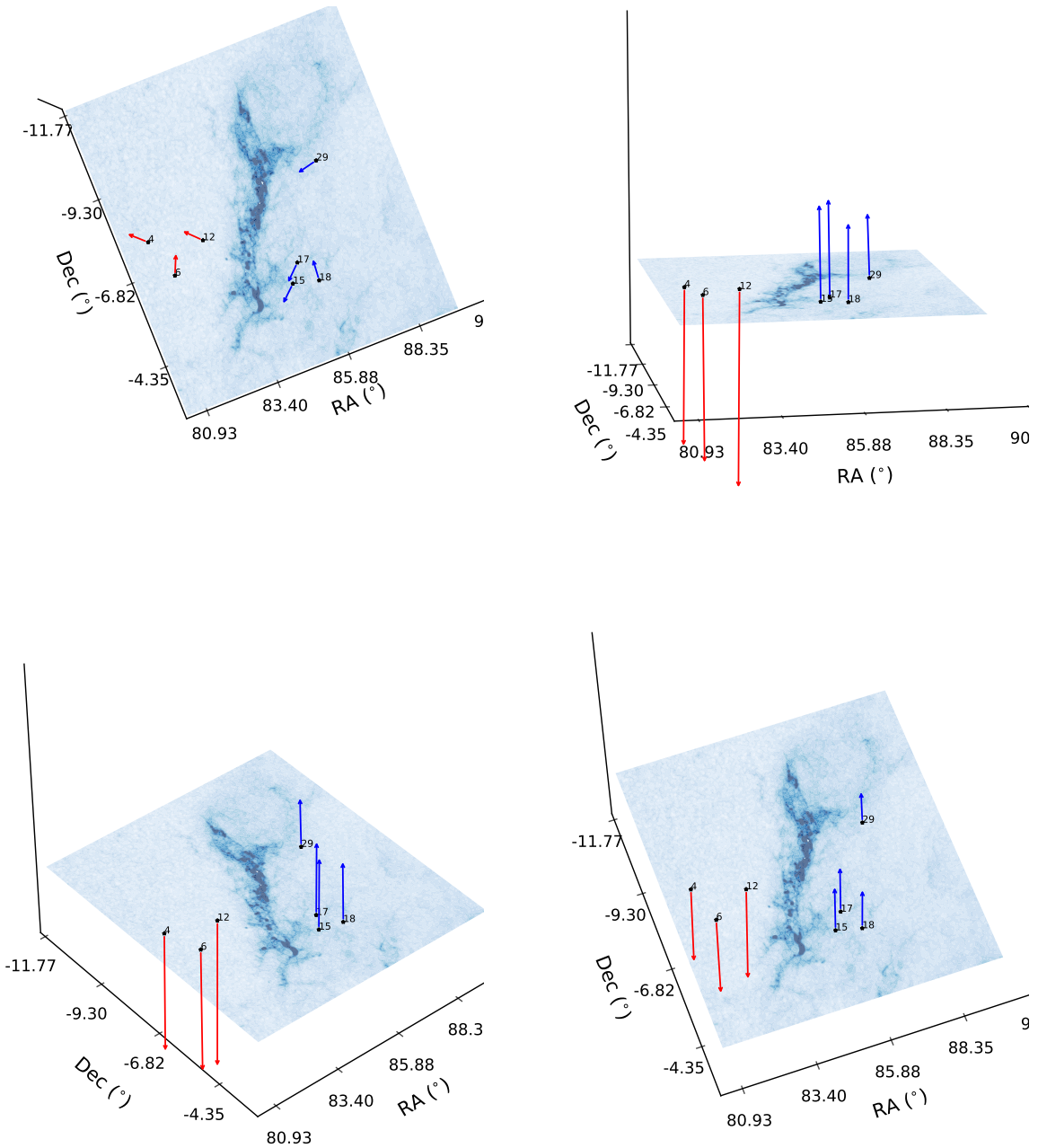


Figure 4.6: B_{LOS} result from Chapter 3 combined with PXXXV B_{POS} in the Orion A for a possible permutation of B_x and B_y direction. The blue (red) color shows the full 3D vectors that their LOS component is towards (away from) the observer. The different panels show the same results as seen from different viewing angles.

4.4.1 The Toroidal Morphology

I investigate the Toroidal model using equation 4.2 and setting $B_1 = 0$ (i.e. a helix with zero pitch angle). When I consider the ratios of each component of the magnetic field to the total averaged magnetic field value, the free parameters R and B_0 cancel out and do not contribute to the final results.

The top row of Figure 4.7 shows the output of the toroidal model for the two different assumptions of the relationship between magnetic field strength and density: $\alpha = 13/16$ (left) and $13/12$ (right). The data points represent the observed values, and the lines depict the model results as described in Section 4.3.4. The blue, red, and green colors illustrate the x , y , and z components, respectively.

The top row of Figure 4.7 suggests that, while the toroidal model fits the z -components of the magnetic field, the modeled x - and y -components do not match the data. The obtained χ^2 values for each component ($\chi_x^2, \chi_y^2, \chi_z^2$) with $\alpha = 13/16$ and $13/12$ are $(0.142, 0.064, 0.001)$ and $(0.141, 0.064, 0.001)$, respectively.

4.4.2 The Helical Morphology

To study the helical model, I use equation 4.2, where B_1 has a small, but non-zero, value compared to B_0 which models a helix with a small pitch angle. The pitch angle of the helix can be parameterised by the ratio of B_1/B_0 . Increasing this ratio increases the pitch angle.

For the helical morphology, after taking the averages along the LOS (see Section 4.3.4) B_1 and B_0 do not cancel out but, instead, remain as free parameters. Therefore, to examine this morphology I explore different B_1/B_0 values and find χ^2 for each combination of these parameters. In this study I calculate the χ^2 for B_1/B_0 from 0.01 to 0.5 in step sizes of 0.01. A sample of B_1/B_0 ratios with their χ^2 result is shown in Table 4.1.

To find the lowest value of χ^2 I consider the sum of the χ^2 for all the components (i.e. $\chi_x^2 + \chi_y^2 + \chi_z^2$). I also pay particular attention to the y -component, since it sets the toroidal model apart from the helical one. The lowest χ^2 occurs for $B_1/B_0 = 0.05$ (both with $\alpha =$

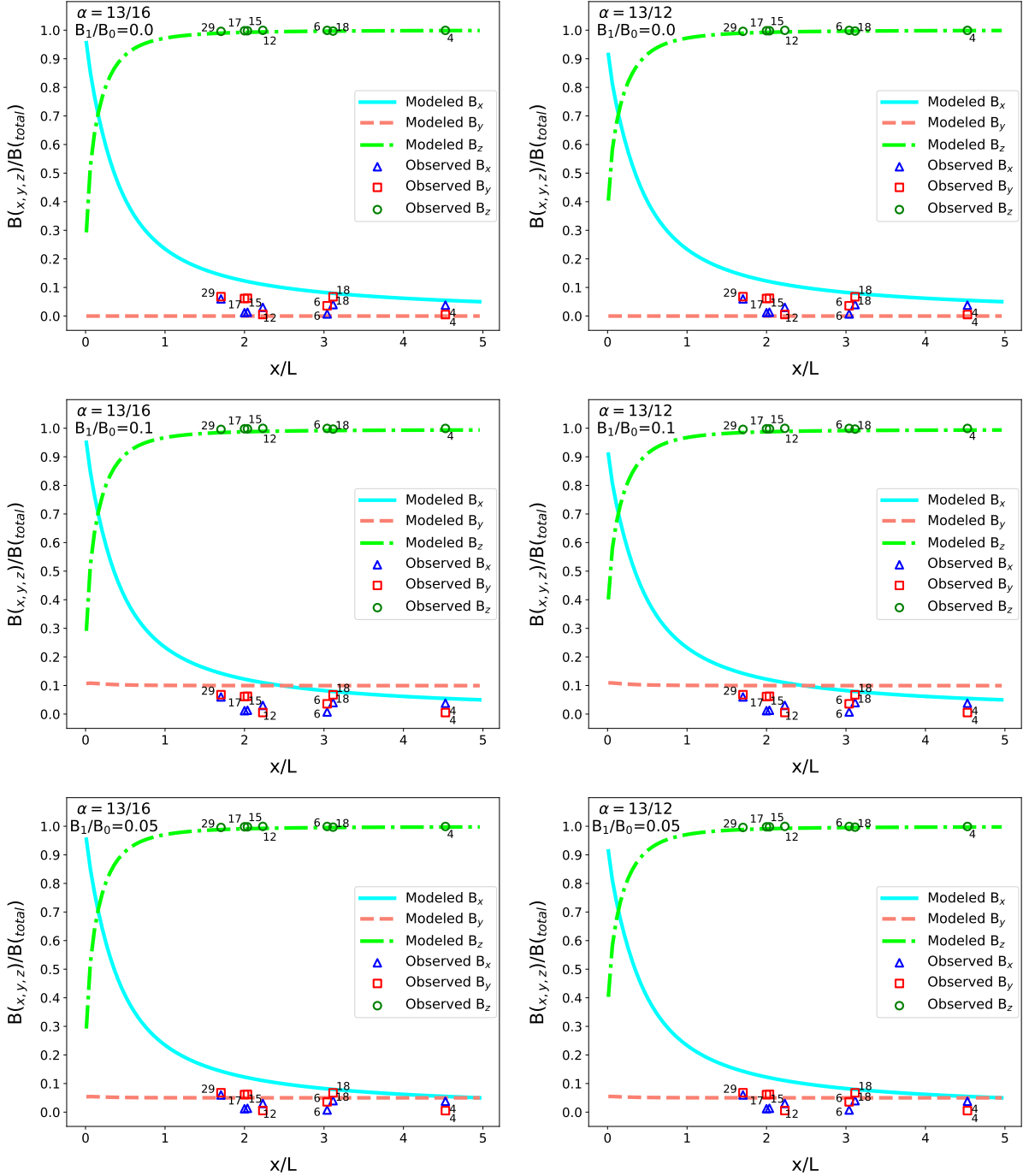


Figure 4.7: Best fit tests for modeled toroidal and helical fields. The magnetic fields are averaged along the LOS. X is the perpendicular distance from the filamentary structure, and L is the integration distance. The parameters show the two α values explained in Section 4.3.2 and different B_1/B_0 ratios from equation 4.2. In each plot the observed data points closest to the modeled values are shown as the observed values in the plot.

B_1/B_0	χ_x^2	χ_y^2	χ_z^2
0.03	0.14340	0.01640	0.00048
0.04	0.14328	0.01206	0.00054
0.05	0.14312	0.01147	0.00062
0.06	0.14293	0.01461	0.00074
0.07	0.14270	0.02146	0.00089
0.08	0.14244	0.03200	0.00108
0.09	0.14215	0.04620	0.00133
0.10	0.14182	0.06403	0.00163
0.11	0.14146	0.08545	0.00200
0.12	0.14107	0.11042	0.00245

Table 4.1: χ^2 values for a helical field with different values of the free parameters, with $\alpha = 13/16$. χ_y^2 and χ_z^2 show the most noticeable changes with changes of the B_1/B_0 ratios.

$13/16$ and $13/12$), with $(\chi_x^2, \chi_y^2, \chi_z^2) = (0.143, 0.011, 0.001)$ for $\alpha = 13/16$ and $\alpha = 13/12$. The two bottom rows of Figure 4.7 represent the modeled helical morphology for $\alpha = 13/16$ (left) and $13/12$ (right). The middle, and the bottom rows show B_1/B_0 value of 0.1 and 0.05, respectively. The bottom panel, showing the best-fit model with $B_1/B_0 = 0.05$, shows that even though the y-component fits the data better than the toroidal, the x-component is still not a good fit.

4.4.3 The Bow Morphology

To model the bow magnetic morphology, I use equations 4.4 and 4.5 separately. I then find the ratio of each magnetic field component to the total magnetic field, for each model, as explained in Section 4.3.4. Since the free parameters of B_1 , B_0 , and R' do not cancel out, I therefore explore different values of B_0/B_1 and R' . Initially I take R' arbitrarily to be equal to the integration distance, i.e. half of the perpendicular distance of point 17 from the filament axis. I then explore the influence of different values of R' , as indicated in Table 4.2. In addition, in equation 4.4, I assume $B_2 = B_1$, so that the x and y components of the magnetic field are equal.

To find the set of parameters that produce the smallest χ^2 results and therefore fit the data best, I explore a range of R' and B_1/B_0 values. Since the observed B_{LOS} values are

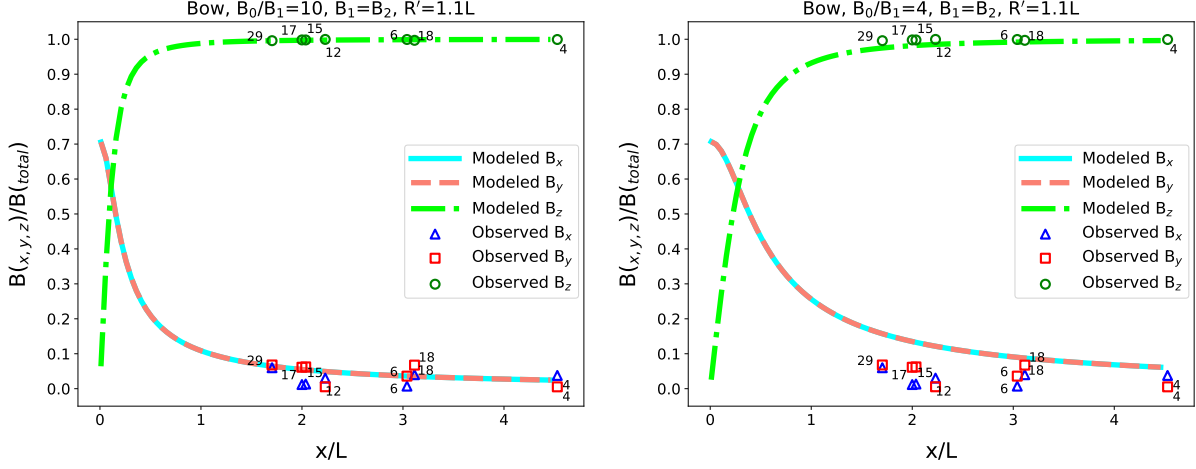


Figure 4.8: Best fit tests of bow magnetic morphology. The magnetic fields are averaged along the LOS. X is the perpendicular distance from the filamentary structure, and L is the integration distance. The parameters show different B_1/B_0 ratios from equation 4.4.

higher than the Planck B_{POS} average strength, I start from $B_1/B_0=4$ and calculate the χ^2 for various R' values up to $B_1/B_0=15$, with step-size of 1. I take this range of parameters because I find that they fit the data better visually. In this range of B_1/B_0 , I explore the R' values from half of the integration distance ($0.5L$) up to $1.8L$, with step-size of 0.1. Figure 4.8 shows the results for this bow model for two sets of free parameters, the left panel represents a set of parameters that produce the smallest χ^2 result. The best-fit model is for $B_0/B_1 = 10$ and $R' = 1.1L$ with $(\chi_x^2, \chi_y^2, \chi_z^2) = (0.018, 0.008, 3e-5)$.

To explore the bow model further, I consider equation 4.5, as described in Section 4.3.3. For this purpose I modify the equations slightly to represent a more general form and to be compatible with my filament setup. I regard $U(x,z)$ in equation 4.6 as:

$$U(x, z) = b_R x (c_R - z)^2 \exp(a_R x^2), \quad (4.9)$$

where a_R , b_R , and c_R are free parameters. Figure 4.9 shows the results for [$r_{flat} = 0.5L$, $a_R = \frac{-8}{(10L)^2}$, $b_R = \frac{-5}{(0.7L)^2}$, and $c_R = 3L$] and for [$r_{flat} = 0.5L$, $a_R = \frac{-8}{(13L)^2}$, $b_R = \frac{-5}{L^2}$, and $c_R = 3L$]. To explore a range of free parameters, I take a_R , b_R , and c_R in form of $\frac{-8}{(aL)^2}$, $\frac{-5}{(bL)^2}$, and $c_R = cL$, and subsequently explore different a , b , and c values in ranges of (start, end,

B_1/B_0	$R' (\times L)$	χ_x^2	χ_y^2	χ_z^2
4.0	0.5	0.02514	0.00901	5.5337e-05
4.0	0.6	0.04053	0.01394	0.00017
4.0	0.7	0.06026	0.02326	0.00041
4.0	1.7	0.47068	0.33440	0.02169
4.0	1.8	0.52989	0.38432	0.02715
5.0	0.5	0.01415	0.00854	1.8022e-05
5.0	0.6	0.02259	0.00856	4.2778e-05
5.0	0.7	0.03385	0.01144	0.00011
5.0	0.8	0.04791	0.01715	0.00025
6.0	0.5	0.00931	0.01072	1.9688e-05
6.0	0.6	0.01415	0.00854	1.8022e-05
6.0	0.7	0.02098	0.00836	3.5993e-05
6.0	0.8	0.02979	0.01016	8.3354e-05
7.0	0.6	0.00988	0.01029	1.8580e-05
7.0	0.7	0.01415	0.00854	1.8022e-05
7.0	0.8	0.01989	0.00826	3.1869e-05
7.0	0.9	0.02707	0.00945	6.6201e-05
7.0	1.0	0.03569	0.01208	0.00013
8.0	0.6	0.00763	0.01257	2.5217e-05
8.0	0.7	0.01033	0.00999	1.7912e-05
8.0	0.8	0.01415	0.00854	1.8022e-05
8.0	0.9	0.01909	0.00822	2.9150e-05
8.0	1.0	0.02514	0.00901	5.5337e-05
9.0	0.8	0.01070	0.00977	1.7496e-05
9.0	0.9	0.01415	0.00854	1.8022e-05
9.0	1.0	0.01849	0.00820	2.7247e-05
9.0	1.1	0.02370	0.00874	4.7994e-05
9.0	1.2	0.02979	0.01016	8.3354e-05
10.0	0.9	0.01100	0.00961	1.7232e-05
10.0	1.0	0.01415	0.00854	1.8022e-05
10.0	1.1	0.01801	0.00819	2.5855e-05
10.0	1.2	0.02259	0.00856	4.2778e-05

Table 4.2: χ^2 values for a bow field as shown in equation 4.4 with different values of the free parameters of B_0/B_1 and R' .

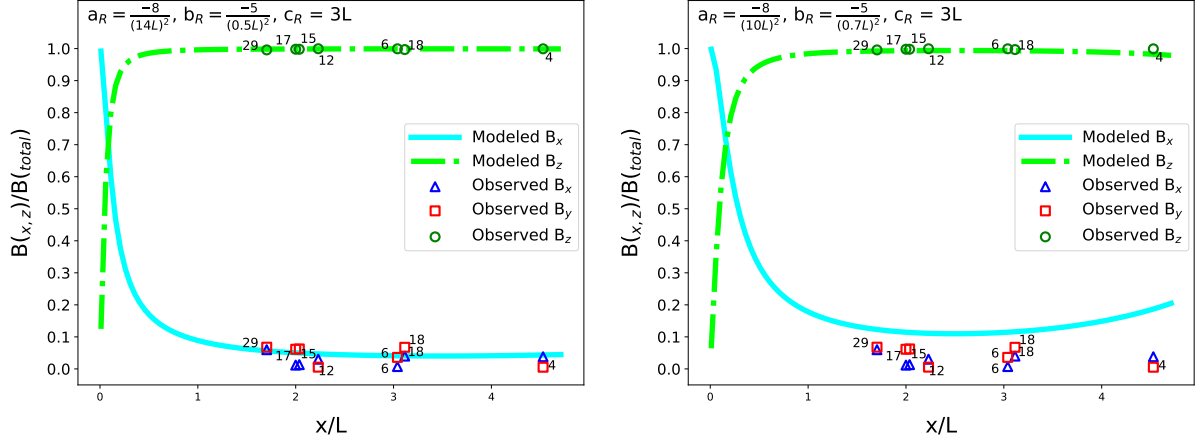


Figure 4.9: Bow magnetic morphology from Equation 4.4. The magnetic fields are averaged along the LOS. X is the perpendicular distance from the filamentary structure, and L is the integration distance.

step-size) = (7, 14, 0.5), (0.1, 1, 0.1), and (1, 10, 1), respectively. A wide range of parameters provide relatively small χ^2 results. Since the B_y component is taken to be zero in this case, the χ_y^2 remains constant and equal to 0.052, which is lower than that of the Toroidal model, and higher than those of both the helical and bow models (the latter using equation 4.4). I find that a few sets of parameters produce the lowest χ^2 result. For example $a = 9.5$, $b = 0.6$, and $c = 6$ (i.e. $a_R = \frac{-8}{(10L)^2}$, $b_R = \frac{-5}{(0.2L)^2}$, and $c_R = 2L$) or $a = 10$, $b = 0.2$, and $c = 2$ produce χ^2 result of $(\chi_x^2, \chi_y^2, \chi_z^2) = (0.004, 0.052, 6e-05)$.

Finally, I should note that in equations 4.5 and 4.6, the density is that of a plummer-like profile to relate magnetic strength to r in $B_0(x, z)$. An alternative approach is to use the earlier proposed relation between the magnetic strength and r (see Section 4.3.2) of

$$B_0(x, z) = \frac{B_0}{(x^2 + z^2)^{\frac{\alpha}{2}}}. \quad (4.10)$$

However, even with this density profile, equation 4.5 for a bow model is not divergence-free. I find that using the two different density profile does not provide noticeably different results.

4.5 Discussion

In this section, I will first discuss the possibility that my magnetic field strengths may be overestimated and how this may affect my results. I will then propose the most likely magnetic field morphology for Orion A based on the modeling.

4.5.1 Modified Magnetic Field Strengths

PXXXV provide a magnetic field value which is averaged over the entire Orion region (see Appendix D, Table D1), whereas TPBK18 provide the field values for very specific points. Since the average value of B_{LOS} is generally much larger compared to the B_{POS} value found in PXXXV, I consider the possibility of systematic biases between the two observing techniques. For this I consider an alternative situation where the B_{LOS} and B_{POS} values are modified by their observational uncertainties (σ) to reduce the difference between the two. This means I lower B_{LOS} by σ_{LOS} and raise B_{POS} by σ_{POS} . Figure 4.10 shows the resultant magnetic field components considering these modified strength values.

For a toroidal field, I find the lowest χ^2 value to be (0.063, 0.129, 0.001) for the x, y, and z components. Similar to Section 4.4.1, the y-component or the x-component of the magnetic field does not produce a good match to the data. For a helical field I find that the lowest χ^2 value belongs to $B_1/B_0 = 0.12$, for both $\alpha = 13/16$ and $\alpha = 13/12$ with χ^2 values of (0.062, 0.021, 0.001). Figure 4.11 shows the toroidal and helical fits with the modified magnetic field strengths.

For a bow field, I find that the lowest χ^2 values are (0.063, 0.020, 0.001) for $B_0/B_1=8$ and $R' = 2L$ (or $B_0/B_1=6$ and $R' = 1.5L$). Figure 4.12 and 4.13 illustrate the bow morphology fitting these modified magnetic strengths using equations 4.4 and 4.5, respectively. Comparing the y-components of the χ^2 values between the toroidal and helical morphologies, I propose that the toroidal morphology is, again, less probable than the helical morphology. However, the χ^2 values for all three x, y, and z components are very similar for the bow and helical

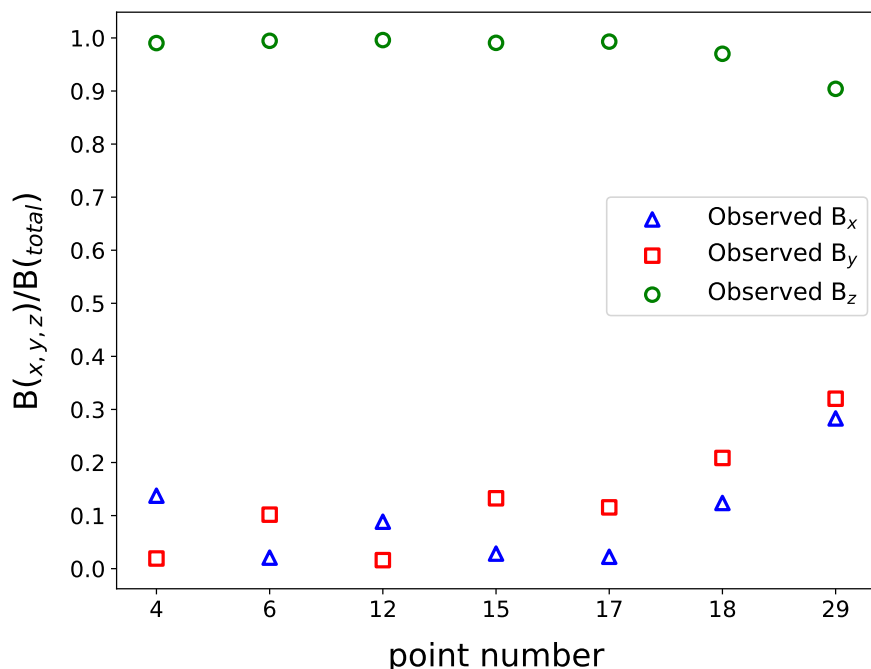


Figure 4.10: Observed B_{POS} and B_{LOS} values as obtained by PXXXV and Chapter 3 respectively, while considering uncertainties so that the $|B_{\text{LOS}}|$ values are the smallest possible values and $|B_{\text{POS}}|$ are the largest one possible within their uncertainties. The y-axis shows the ratio of each component of magnetic field to the total value and the x-axis shows the point numbers as shown in Figure 4.2. x, y, z refer to the frame system illustrated in Figure 4.3.

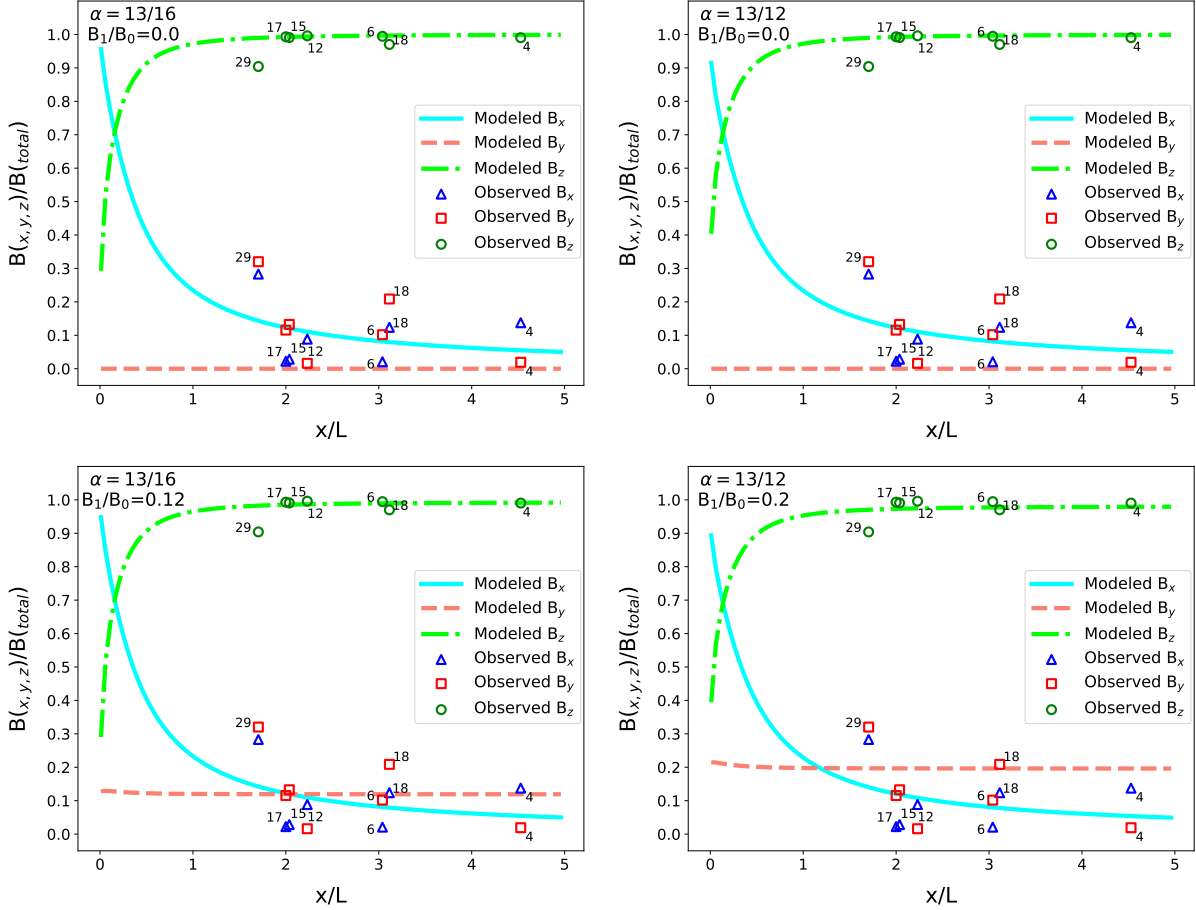


Figure 4.11: Best fit test of modeled toroidal and helical fields with modified observation values. The magnetic fields are averaged along the LOS. X is the perpendicular distance from the filamentary structure, and L is the integration distance. The parameters show the two α values explained in Section 4.3.2 and different B_1/B_0 ratios from equation 4.2. In each plot the observed data points are shown. The observed values are taken within their uncertainty range in a way that results to smallest magnitude difference between the observed B_{POS} and B_{LOS} .

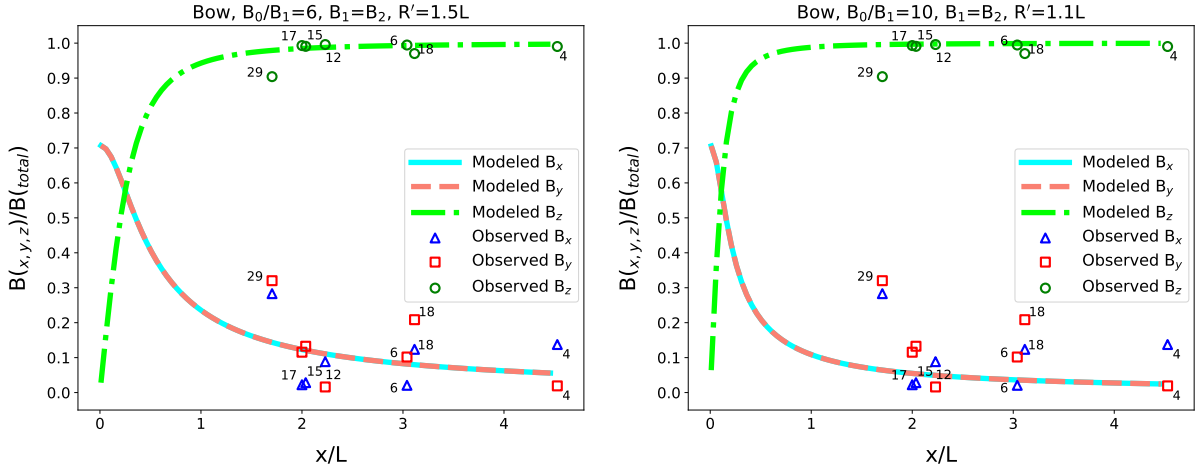


Figure 4.12: Bow magnetic morphology. The magnetic fields are averaged along the LOS. X is the perpendicular distance from the filamentary structure, and L is the integration distance and cancels out when I take the ratios. The parameters show different B_1/B_0 ratios from equation 4.4. The observed values are taken within their uncertainty range in a way that results to smallest magnitude difference between the observed B_{POS} and B_{LOS} .

field morphologies.

In this case, where I have modified the magnetic field strengths, I again find that the toroidal model is the worst fit to the data. Additionally, I find that none of the models fit the data as well as they did before. This is mainly because the modified magnetic field strengths show much more variation/scatter than they did before and, in consequence, there is no model using an ordered magnetic field morphology that could fit these data. Given that the maps do show an ordered field (both in the B_{POS} and B_{LOS} directions) this suggests that modifying the magnetic fields in this way is probably not appropriate.

4.5.2 Tilted Models for Orion A

The models of equations 4.2, 4.4, and 4.5 represent a filament that is assumed to be lying in the plane of the sky without being tilted away from, or towards, the observer. However, recent observations by Großschedl et al. (2018) show that the Orion A filamentary structure is inclined along the LOS with respect to the observer.

If we consider a tilted filament, the equations representing the models will not change

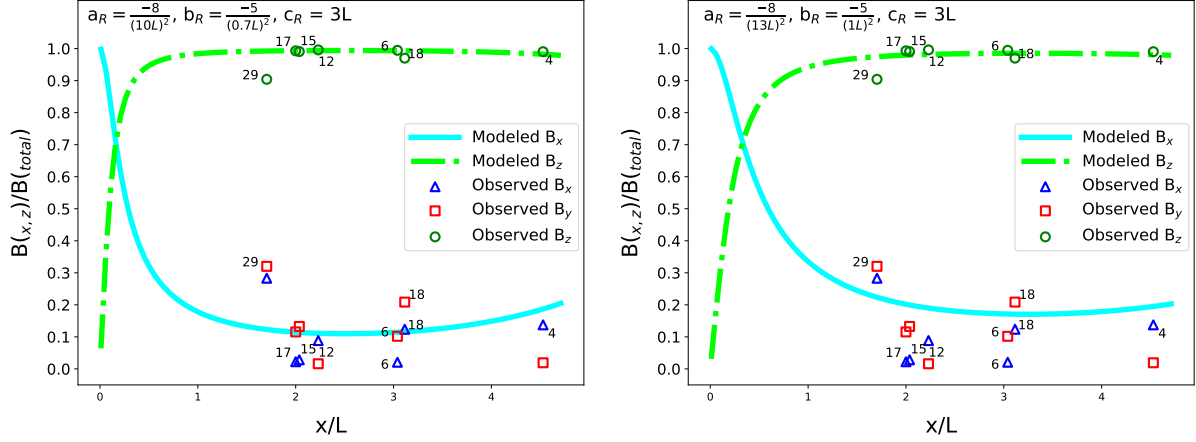


Figure 4.13: Bow magnetic morphology. The magnetic fields are averaged along the LOS. X is the perpendicular distance from the filamentary structure, and L is the integration distance. The observed values are taken within their uncertainty range in a way that results to smallest magnitude difference between the observed B_{POS} and B_{LOS} .

since the frame of reference is adjusted to the filament as illustrated in Figure 4.3. However, when we take the average of each magnetic field component along the line-of-sight, we have to adjust dz in equation 4.7, such that this dz is the line-of-sight path length from the observer's point of view and not in the filament's reference frame.

I suggest that in this study of magnetic morphologies, I do not need to consider inclination of the Orion A region along the line-of-sight. This is because of the fact that in the study by Großschedl et al. (2018), the part of the Orion A region that contains Orion KL has a close-to-zero tilt. In particular, the region that contains L1641-N in Orion A, which is very close to 6 of the 7 data points taken in my analysis, has zero inclination in Figure 3 of Großschedl et al. (2018).

4.5.3 Selecting the Best Magnetic Field Morphology

To compare the toroidal and helical models I only need to compare the χ^2 values of the two models with each other. This is because these two models are, in fact, a single model with different parameters (one with $B_1/B_0 = 0$ and the other with $B_1/B_0 = 0.05$). Therefore, based on the χ^2 values in Section 4.4, I suggest that a helical morphology fits the data better

than a toroidal one. Since it is the y-component that sets the toroidal and helical models apart, comparing the y-component in the top panel of Figure 4.7 with the bottom-left panel illustrates that a helical model (with $B_1/B_0 = 0.05$) is a better fit for the data.

To compare the bow morphology to the helical/toroidal morphology, I first compare the left panel of Figure 4.8 and left panel of Figure 4.9 with the helical and toroidal models in Figure 4.7. These figures suggest that both of the two bow models fit the data better than the toroidal or the helical models. The χ^2 values for the bow model - (0.018, 0.008, 3e-5) for equation 4.4 and (0.004, 0.052, 6e-5) for equation 4.5 - are also significantly lower than the helical χ^2 value of (0.143, 0.011, 0.001).

However, to compare different models one cannot simply compare their χ^2 values. To compare the bow morphology to a toroidal one, since they represent two different models, I compare their probability values (i.e. p-values). P-values allow one to compare different models by providing the probability for a statistical relevant model. The probability value provides the likelihood that a hypotheses (toroidal, helical, and bow) is true (Sivia and Skilling 2006). In statistical analysis, p-values are normally used to reject a null hypothesis. If we assume that they represent a Gaussian distribution, it is a measure to understand whether the result from the hypothesis is closer to the peak of the distribution or its tail. To find the p-values, we need the χ^2 values and the degrees of freedom of the model. For the helical and toroidal I take one degree of freedom (which is the free parameter of B_1/B_0) for the first bow model I take two degrees of freedom (B_0/B_1 , and R') for the second bow model I take three degrees of freedom (a_R , b_R , and c_R).

The Reissl et al. (2018) model ($\chi^2 = (0.004, 0.052, 6e-5)$ with three Degrees of Freedom (DOF) and therefore p-values = (0.999, 0.996, 0.999)) and my simple bow model ($\chi^2 = (0.018, 0.008, 2e-5)$ with two DOFs and p-value=(0.991, 0.996, 0.996)) have higher probability values compared to my best helical case ($\chi^2 = (0.143, 0.011, 0.001)$, with one DOF and therefore p-value = (0.705, 0.914, 0.980)). Based on these p-values none of the models can be ruled out. However, by combination of considering figures 4.7, 4.8, and 4.9 and these p-values it is

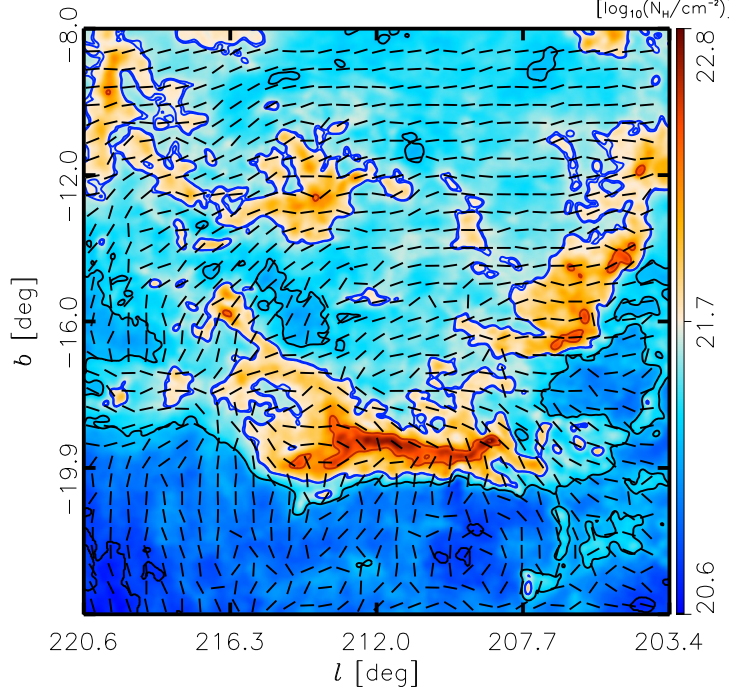


Figure 4.14: Plane-of-sky component of magnetic field in Orion as obtained by Planck observations. The lines show B_{POS} lines, the color coding shows the column density of the Orion region. (Figure 5 from Planck Collaboration et al. (2016))

likely that the bow morphology is more probable than either the helical or toroidal.

Additionally, as shown by the Planck results in Figure 4.14, the B_{POS} lines on one side of the Orion A filament are mostly perpendicular to the filament (representing a small pitch angle for a helical morphology) while, on the other side, they are more parallel to the filament. Therefore, if we assume a helical magnetic field morphology for the Orion A region, we would have to consider completely different pitch angles for the two sides of the filament which is not sensible. Therefore, this simple visual analysis of the B_{POS} orientation also seems to suggest that a bow morphology is a more natural fit to the data.

4.6 Modeling Conclusions

Comparing models with observations I find that a toroidal morphology is the least probable interpretation for the B_{LOS} direction-change around the Orion A filament, since it provides

the worst fit to the data (both in terms of the χ^2 and p-values). Furthermore, I suggest that the bow morphology is the most natural magnetic field morphology for the Orion A region. This conclusion is based on the following arguments:

1. The bow model has the lowest χ^2 values, the highest p-values and, visually, the best fit between the data and the models.
2. The Orion A region is not isolated and is likely impacted by the Orion-Eridanus superbubble. This association has led other authors to suggest a bow morphology for this region.
3. Different B_{POS} angles on the eastern side of the filament compared to the western side, which suggests that the data cannot be properly be modeled by a single helix with the same pitch angle on both sides of the filament.

The analysis in this chapter utilises the best rotation measure data currently available in the Orion A region. As such, it is limited to the number of available RM sources in the Taylor et al. catalog, as well as the sensitivity of those observations. This analysis is also limited by the fact that the Planck maps provide only one value for B_{POS} averaged across the entire region. It is difficult to truly reconstruct the 3D geometry of the magnetic field based on these limited observations.

Future RM catalogs from new generation surveys such as POSSUM and VLASS will allow for the detection of a higher number of B_{LOS} sources and with better sensitivity. Thus, these new catalogs will provide better-sampled maps of the large-scale B_{LOS} magnetic field with smaller errors. Combined with new and improved dust polarisation maps (from instruments like APEX, ALMA, BLASTPOL2), future applications of the techniques presented in this chapter will allow us to map and model the 3D magnetic field geometry with better accuracy.

Chapter 5

Magnetohydrodynamics Simulations

In order to continue investigating the 3D magnetic field morphology, I use MHD simulations. As described in Chapter 2, MHD studies help us approximately investigate the co-evolution of magnetic fields and the region of study. For the purpose of investigating the 3D magnetic field morphology of filamentary MCs, I use the simulation code FLASH 4.3¹. I simulate and study a filament with different initial input parameters, for both large-scale and small-scale filaments.

FLASH is a publicly available, multi-physics, multi-scale simulation code, which has been developed and used internationally. It was in part developed by the DOE NNSA-ASC OASCR Flash Center at the University of Chicago. The FLASH code has been developed, maintained, rigorously tested, and upgraded for the past 20 years. FLASH code has a built-in unit test framework combined with regression tests. These run nightly at the FLASH center to verify the code constantly.

FLASH has been used for the MHD and HD simulations of star clusters, MC formation and evolution, Galaxy evolution, and smaller-scale star formation (e.g., Klassen et al. 2014; Banerjee et al. 2004; Howard et al. 2018, 2017; Klassen et al. 2012; Seifried et al. 2012). Due to its high performance and continuously tested modules, I chose FLASH for my simulations.

To study the filaments in a theoretical setup and run FLASH, I take the following steps:

¹<http://flash.uchicago.edu/site/>

- Selecting the modules which FLASH will use to perform the computations (i.e. the *FLASH units*)
- Determining the input parameters
- Setting up FLASH and preparing the initial files
- Submitting the files to the computational Clusters
- Running FLASH

These steps will be described in detail below.

5.1 The FLASH Units

To study the evolution of molecular filaments, the FLASH units I include are: Gravity (Barnes–Hut tree), Polytrope equation of state, sink particles, and an MHD solver. Additionally, to reduce the required number of CPUs (Central Processing Units) and computing time, and to simultaneously have a high enough resolution to adequately investigate the regions of interest, I use Adaptive Mesh Refinement (AMR), which is included in FLASH in a package called PARAMESH (MacNeice et al. 2011).

5.1.1 Gravity

The gravity exerted in the simulation box for an isolated filament, is from the filament itself (i.e. self-gravity). To include the gravitational term in the MHD equations, the gravitational acceleration, $g(x)$, needs to be determined, meaning that we have to solve the Poisson equation for gravity (equation 2.19), or:

$$g(x) = -\nabla\Phi(x), \quad (5.1)$$

where $\Phi(x)$ is the gravitational potential. Therefore, FLASH solves the Poisson equation of gravity using a method based on a Barnes–Hut tree (Barnes and Hut 1986). The Barnes–Hut

tree solver in FLASH is developed by Wünsch et al. (2018).

In a traditional approach, the interaction force between all the particles (fluid elements in this case) is calculated, which is more accurate but is much more computationally expensive. In the tree approach, however, the particles (fluid elements) are grouped together, and it is these groups that communicate with each other and within the groups. To explain this, Barnes and Hut (1986) provide an analogy of the way humans interact with their immediate neighbour, people in nearby villages, further villages, cities, and countries at larger and larger distances. This hierarchical force calculation is known as the tree solver. In this way, Barnes and Hut (1986) approximate the force on each particle (fluid element here) using a recursive calculation.

5.1.2 Adaptive Mesh Refinement and Sink Particles

The simulation box is composed of smaller blocks. In AMR, these blocks can themselves be divided into smaller sub-blocks to allow for more accurate investigation of specific regions. The default AMR package in FLASH is PARAMESH (Macneice et al. 2000). The largest blocks are known as the *root-blocks* and the smaller ones are referred to as *child-blocks*, these child-blocks can themselves be divided into smaller blocks. The smallest block that is not divided into sub-blocks is known as a *leaf-block*. Each leaf-block is composed of cells such that one 3D block is composed of 2^3 cells. The process of dividing blocks to smaller ones is called *refining* and the new smaller blocks are known to be *refined*. In *de-refinement*, smaller blocks can become larger ones when such small details are no longer necessary or desired. The code is capable of local refinement and de-refinement of the computational grid during the simulations (Papoutsakis et al. 2018).

The FLASH user manual lists three rules for refining new blocks: 1) the child-blocks have to be $1/2$ as large as their parent block, 2) the child-blocks of a parent one must fill the volume of the parent-block and cannot exceed it or be smaller, and 3) the neighboring blocks (which share a border) cannot exceed a difference of more than one refinement level,

meaning that if a leaf-block has a refinement level of 2, its border-sharing leaf-blocks can have refinement levels of 1, 2, or 3. Figure 5.1 shows a simulation box with different levels of refinement and child-blocks. The cells are not depicted in this figure.

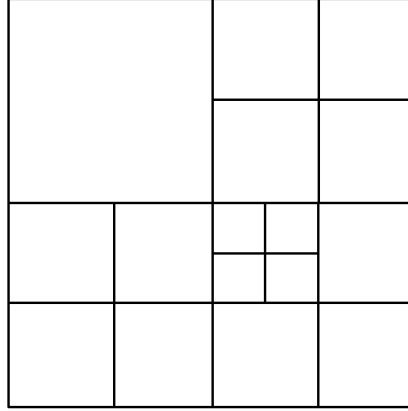


Figure 5.1: An illustration of the parent- and child-blocks with different levels of refinement for a 2D box. The neighboring blocks can have a maximum difference of one level of refinement.

For my simulations, I set the refinement level such that the box resolution, i.e. the size of the smallest cell, is 0.01 pc (a tenth of the filament width) for the small-scale filaments, and is 0.004 pc for the large-scale filaments. A higher resolution for the large-scale filament was employed to explore the formation of potential magnetic field reversals at different scales within the filaments themselves. The higher the refinement level is, the more computational time and power is needed. This resolution provides necessary information for forming *sink particles*.

Sink particles in the simulations, are used to model dense cores and stars. Substituting the formed cores and stars with *sink particles* (Federrath et al. 2010) enables us to avoid artificial fragmentation of these cores and stars. For this purpose, the Jeans length should be considered and resolved appropriately.

As the density increases, λ_J decreases. This, therefore, could lead to artificial fragmentation of the cores in the simulations. To avoid this problem, the Jeans length must be resolved with, i.e. contain, at least minimum of four grid cells (Truelove et al. 1997). For example, if the smallest cell size is 0.01 pc, the Jeans length should be at least 0.04 pc. This resolution

criterion also sets the density threshold (ρ_{thresh}) for formation of sink particles.

During the simulations, FLASH automatically refines the grid based on the Jeans length till it reaches the highest refinement level, or the smallest cell size set by the user. If this highest level is reached and the Jeans length reaches four cells, then the cores are replaced by sink particles to avoid their artificial fragmentation.

Other than the criterion mentioned above, FLASH checks for additional criteria, set by Federrath et al. (2010) and summarised by the FLASH user manual, which prevent the formation of false sink particles. FLASH first sets a spherical control volume around each cell that exceeds ρ_{thresh} and checks that the gas in this control volume:

- has the highest refinement level,
- has its velocity converging toward the center,
- is gravitationally bound,
- is gravitationally unstable,
- is not in the spherical control volume of other sink particles.

5.1.3 MHD Solver

In my simulations, I use ideal MHD - an approximation which has been widely used to study MCs (André et al. 2014) and particularly widely used in FLASH. In ideal MHD, the dissipation of the magnetic field is assumed to be negligible over the evolution timescale of the cloud (which is dominated by the free-fall time-scale of the cloud, duration which it gravitationally collapses and forms cores and stars). I use the Unsplit Staggered Mesh MHD solver (USM; Lee 2013) in FLASH to solve the MHD equations. This scheme splits the solution for smooth flows versus shock flows. The solution it provides has second-order accuracy for the smooth flows and first-order accuracy for shock flows in both space and time. The term *staggered mesh* reflects the fact that, in this solver, the magnetic field variables are

face-centered, meaning that they are assigned to the face of each cell instead of their center (cell-centered).

5.1.4 Equation of State

The Equation of State (EoS) connects the important “state” variables of a fluid - pressure, density, and temperature. For my simulations, I use the Polytrope unit, with an equation of state described by:

$$p \propto \rho^\gamma, \quad (5.2)$$

where ρ is the gas density, p is the thermal pressure, and γ is the ratio of specific heat at constant pressure to specific heat at constant volume. I use $\gamma = 1$, in my simulations, for an isothermal filament, with a temperature of 15 K, consistent with observations (e.g., André et al. 2010).

5.2 The Input Parameters

To study the co-evolution of the filamentary structures and magnetic fields, I consider both small- and large-scale filaments. Small-scale filaments can represent coherent shapes or structures such as the *fibers* of Hacar et al. (2013) and are typically of the order of 1 pc long. The large-scale filaments can be composed of these smaller sub-structures and represent the larger, star-forming molecular filaments such as Orion A. They are typically of order of tens of parsecs long. It is important to investigate the co-evolution of magnetic fields and filaments at different scales to see if, at any scale, their evolution results in the observed B_{LOS} direction change across the filaments.

For a small-scale filament, my simulation box size has a width of 0.8 pc along the y- and z-axes, a length of 2.4 pc along the x-axis, and a filament length of 1.6 pc, consistent with observations (Arzoumanian et al. 2011). For a large-scale filament, my simulation box is 16.7 pc wide along the y- and z-axes, and 50 pc long along the x-axis. This filament’s length

is 37 pc, based on the average length of filaments studied in Chapter 3. For both small and large filaments I use a Plummer-like density profile, a Kolmogorov turbulence spectrum, an initially homogeneous magnetic field, and the filament’s physical length. I also assume that the filament rotates as a solid-body. These parameters will be described in more detail in the sub-sections below.

5.2.1 Density Profile

For the total density of the filament, I use a Plummer-like radial density profile, which is consistent with observations of a number of filaments (e.g., Arzoumanian et al. 2011). Plummer-like density profiles have been used in observational (e.g., André et al. 2010; Gong et al. 2018) and theoretical studies (e.g., Smith, Glover and Klessen 2014; Kirk et al. 2015), to represent isothermal filaments. The standard Plummer profile is described in equation 4.3 in Chapter 4.

Observations by Arzoumanian et al. (2011) suggest an average value of 2 for the exponent parameter p and 0.033 pc for r_{flat} for equation 4.3. In addition, for $p = 2$, the derived Full Width Half Maximum (FWHM)² is $\sim 1.5 \times 2r_{flat} \sim 0.1$ pc, which is typically considered as the “width” of the filament (Arzoumanian et al. 2011). For my small-scale filaments, I use $\rho_c = 10^{-19} \text{ g cm}^{-3}$ or $2.6 \times 10^4 \text{ particles cm}^{-3}$, based on observations of the central column density and filament width by Arzoumanian et al. (2011). I also set a filament length of 1.6 pc and a width of 0.1 pc (using $p = 2$ and $r_{flat} = 0.033$ pc). For my large-scale filaments, I set $\rho_c = 3.9 \times 10^{-22} \text{ g cm}^{-3}$ or 100 particles per cm^3 . While this is ~ 10 times lower than the “typical” density in a molecular cloud, it was necessary to prevent the large filaments from immediately fragmenting and collapsing under gravity. I also set this filament’s length to be 37 pc with a width of 1.5 pc (using $p = 2$ and $r_{flat} = 0.5$ pc).

At both ends of the filament’s major axis (x-axis), I also force the density to decrease exponentially to prevent pressure jumps. This exponential tapering begins at $x = \pm L/3$,

²FWHM determines the distance between two points of a function where it reaches half its maximum value.

where at the center of the simulation box $x = y = z = 0$ and L is the length of the simulation box. Figure 5.2 illustrates a schematic sketch of these dimensions. For example, with a simulation box with a length of 2.4 pc, the tapering begins at $x = 2.4/3$ pc from the center. This value of $L/3$ was chosen to ensure that the box edges are not right at the ends of the filament. This way I can study the evolution of the field lines in the environment surrounding the filament without having to increase the box size and, thus, the computational time. Beyond this x-position, the exponential tapering of the filament is defined as

$$\rho_{tapered}(x[\text{pc}], r[\text{pc}]) = \rho(r) \exp\left(-\frac{x - \frac{L}{3}}{2r_{flat}}\right), \quad (5.3)$$

where the $\rho(r)$ is described in equation 4.3. The r_{flat} term comes into the equation so that the tapering at the filament ends matches that in the radial direction (i.e. from the Plummer profile).

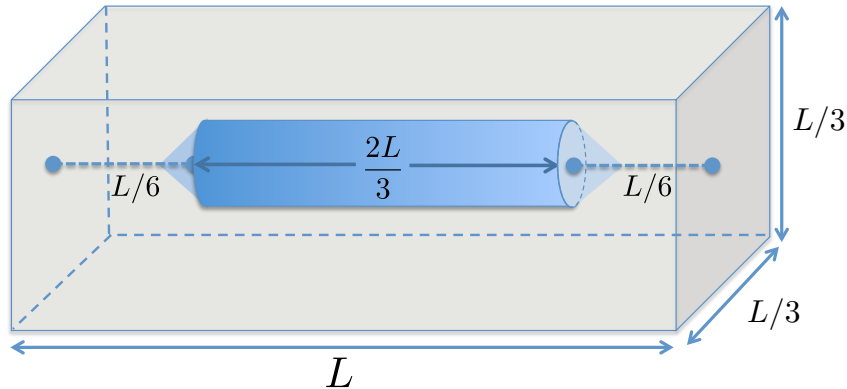


Figure 5.2: An illustration of the filament and its dimensions within the simulation box. To avoid pressure jumps an exponential tapering of the filament begins at $x = \pm L/3$, where L is the length of the simulation box.

To ensure that my density profiles and central densities are realistic, I calculate the Mass per Length ratio (M/L) for each filament to ensure that it is not significantly larger than the “critical value” for an isothermal cylinder. This “critical value” is the M/L ratio above which the filament begins to fragment and collapse due to self-gravity and can be calculated from

(Ostriker 1964)

$$M/L = \frac{2k_B T}{\mu_{mol} m_p G}, \quad (5.4)$$

where T is the temperature of the system, k_B is the Boltzmann constant ($k = 1.38064852 \times 10^{-23}$ J K $^{-1}$), μ_{mol} is the mean molecular weight of 2.3 (i.e. the mean number of protons of a particle in a molecular cloud - accounting for the H₂ and He abundances), and m_p is mass of a proton. For a filament with temperature of $T = 15$ K, the critical M/L is 1.61×10^{15} Kg m $^{-1}$ or 25 M $_{\odot}$ pc $^{-1}$ (M $_{\odot}$ = 1.989×10^{30} kg).

To calculate the mass of a simulated filament, I use

$$M = 2 \int_0^{width/2} \rho(r) 2\pi r L dr, \quad (5.5)$$

and substitute in my expression for the density profile $\rho(r)$. The resultant equation is

$$M/L = 2\rho_c \int_0^{width/2} \frac{2\pi r dr}{1 + (r/r_{flat})^2}. \quad (5.6)$$

For a small-scale filament with a central density of 10^{-19} g cm $^{-3}$, width of 0.1 pc, and a length of 1.6 pc, the mass per length is 5.9 M $_{\odot}$ pc $^{-1}$. For a large-scale filament, with a central density of 3.9×10^{-22} g cm $^{-3}$, width of 1.5 pc, and a length of 37 pc, its mass per length is 5.3 M $_{\odot}$ pc $^{-1}$. Both of these M/L ratios are smaller than the critical value meaning that they will not immediately begin to fragment and collapse to form cores at the beginning of the simulation. This prevents an unrealistically efficient star formation process. As the filament evolves, the M/L will also change. Eventually, regions of these filaments will exceed the critical M/L ratio and they will fragment, and collapse to form cores.

5.2.2 Turbulence

Turbulence refers to nonlinear random-like fluid motion and can be described by the typical picture of a turbulent energy cascade (Kolmogorov 1941; Richardson 1922), in which energy

is injected into the system via large eddies, these eddies break down into smaller and smaller eddies in a continuous process, until the smallest eddy length-scale is reached. The energy is then dissipated and transferred to the system (as heat) via these smallest eddies. A ditty by L.F. Richardson summarises the concept of the turbulence spectrum (Shu 1992):

*Large eddies have small eddies
 Which feed on their vorticity,
 Small eddies have smaller eddies
 and so on to viscosity.*

In my simulations, I use a Kolmogorov spectrum (Kolmogorov 1941) of turbulence to characterise the initial turbulence field. The Kolmogorov spectrum mathematically explains how energy is transferred from large scales to small scales and then decays away due to dissipation in the inertial subrange. In this range the effects of viscosity are insignificant (Valente 2013). This spectrum can be described by:

$$E(k) \propto k^{-\frac{5}{3}}, \quad (5.7)$$

where k is the turbulence wavenumber (with a value of $2\pi/\lambda$), and λ represents the length-scales of the turbulence eddies.

Observations by Larson (1981) show that the velocity dispersion in MCs can, indeed, be described by a Kolmogorov spectrum. This has been supported by Heyer and Brunt (2004) who examined the velocity field for 27 GMCs and proposed that, despite the differences in the environments and star formation activity in each cloud, the turbulence pattern is approximately universal as observed by Larson (1981).

To implement the Kolmogorov spectrum in my simulations, I need to choose the permitted range of length-scales for both the largest and smallest eddies. In other words, I need to find the maximum and minimum length-scales and, consequently, the wavenumbers for the cascade of energy. The highest and lowest values of k , typically referred to as turbulence modes,

subsequently limit the turbulence spectrum to be between what these values determine at the initial setup. After the first step, other turbulent modes (i.e wavenumbers) can be reached.

The largest turbulence length-scale, λ_{max} , corresponds to the smallest wavenumber (k_{min} ; i.e. $\frac{2\pi}{\lambda_{max}}$), and the smallest length-scale, λ_{min} , corresponds to the largest wavenumber (k_{max} ; i.e. $\frac{2\pi}{\lambda_{min}}$). To pick values of k_{min} and k_{max} for these simulations, I assume that λ_{max} is comparable to the filament width, otherwise we will produce large bulk motions. λ_{min} is chosen so that it encloses two of the smallest cells. This ensures that we do not cascade energy to scales smaller than the resolution of the simulation. This also satisfies the Nyquist theorem, where the smallest resolvable wavelength is $2\Delta x$, where Δx is the smallest cell-size.

When the average turbulent velocity, $\langle v_{turb}^2 \rangle^{0.5}$, is larger (smaller) than the sound speed in an environment, we refer to the turbulence as supersonic (subsonic). When they are comparable we refer to it as transonic turbulence. The sound speed is calculated from

$$c_s = \sqrt{\frac{k_B T}{\mu_{mol} m_p}}, \quad (5.8)$$

where k_B is the Boltzmann constant, μ_{mol} is the mean molecular weight of a particle in a molecular cloud, and m_p is the mass of a proton. Using this relation, the sound speed of a cloud, with a temperature of 15 K and μ_{mol} of 2.3, is 188 m s^{-1} .

For the small-scale filaments, the average initial fluid element velocity is 484 m s^{-1} . I calculate this velocity from $V = \sqrt{2KE/m}$, where I read the kinetic energy (KE) and the mass (m) of the filament from the simulation output file, at the first time step of a test simulation with the absence of filament rotation. For the large-scale filaments, the average velocity at the first time-step (determined in the same way) is 749 m s^{-1} . The higher turbulent velocity in the large-scale filament reflects the fact that larger filaments associated with massive star formation (like Orion A) have broader line-widths than the smaller filaments.

To implement turbulent gas motion in the simulated filaments, I use a turbulence code developed by Girichidis et al. (2011). In this code, a random velocity is created in Fourier space and is then transformed to real space. The code uses a random number generator from

the GNU Scientific Library (GSL)³ and for the Fourier transform it uses the fftw3 Library⁴. Additional input parameters to the code are: the type of turbulence spectrum (Kolmogrov), the simulation resolution (based on the highest level of refinement), k_{min} , and k_{max} . The code then produces a file containing the turbulence spectrum. This file is used as an input for my FLASH simulations.

5.2.3 Filament Rotation

Observational studies of the velocity fields in Perseus and Orion have found velocity gradients along the minor axis of these filaments (Uchida et al. 1991; Olmi and Testi 2002; Lee et al. 2014; Fernández-López et al. 2014). While some of these studies interpret this velocity gradient as a cloud-cloud collision (Duarte-Cabral et al. 2010), others interpret it as the filament rotation. For example, from their observations, Uchida et al. (1991) suggest that filaments in the Orion KL region (a small star-forming region within the Orion-A map) are rotating with speeds of $\sim 1 \text{ km s}^{-1}$, corresponding to a rotation frequency of $\sim 5 \times 10^{-14} \text{ Hz}$ for a filament with radius of 0.1 pc. Observations of the Serpens filament by Olmi and Testi (2002) suggest that this filament is rotating with an angular rotation of $4.1 \times 10^{-14} \text{ Hz}$.

Hypothetically, rotation can twist the frozen-in field lines and wrap them around the filament. Uchida et al. (1991) suggest that a toroidal component of the magnetic field, with a strength of $100 \mu\text{G}$, is continuously produced through its rotation in Orion KL. To account for this rotation in my simulations, I introduce solid body rotation of the cylindrical filaments. For the small-scale filaments, I use rotation frequencies of $7 \times 10^{-14} \text{ Hz}$, 10^{-12} Hz , 10^{-15} Hz , and zero. The value of $7 \times 10^{-14} \text{ Hz}$ is chosen to simulate filaments with rotation frequencies similar to those observed. The other frequencies are chosen to explore the effects of faster rotation, slower rotation, and no rotation on the evolution of magnetic field lines. For the large-scale filaments, I use a single rotation frequency of $5 \times 10^{-15} \text{ Hz}$. This value was chosen to simulate a large filament rotating with a speed of 1 km s^{-1} . Since the width of these

³<https://www.gnu.org/software/gsl/>

⁴<http://www.fftw.org/>

filaments (~ 1 pc) is about 10 times that of a small-scale filament, the rotation frequency is 10 times smaller.

5.3 Setting Up FLASH and Preparing the Input Files

The FLASH code can be obtained from the FLASH Center for Computational Science⁵. The code is accompanied by a user manual, which provides detailed description for unpacking, configuring, and using the FLASH code. Additional help can be quickly obtained through the FLASH mailing list.

The tools/modules required to configure FLASH are a Fortran 90 and a C Compiler, a copy of the Message-Passing Interface (MPI) library for running FLASH on a number of CPUs in parallel, a Hierarchical Data Format (HDF) for the output files, and a copy of the Python language to run the setup script. Additionally, a Makefile is required, which should be modified to meet the machine/system's requirements. Examples of Makefiles can be found in the ‘sites’ directory of FLASH. For each machine or cluster the appropriate paths for the MPI and HDF should be specified in the Makefile.

To *configure and compile* FLASH any FLASH source file can be modified to best fit the simulation purposes. If any changes in these files are made, FLASH has to be re-configured/re-compiled. There are certain files which always have to be modified when investigating a new problem. These files are in the FLASH simulation unit and are the Config, Simulation_data.F90, Simulation_init.F90, and Simulation_initBlock.F90 files. For my simulations, I modified the Config, Simulation_data.F90, Simulation_init.F90, and Simulation_initBlock.F90 files developed by Seifried and Walch (2015). These files, and my modifications to them, are described below.

The Config file is a plain text file which specifies the required FLASH units for the simulations and has information about runtime parameter definitions and library requirements. The simulation setup starts from the Config file. The units I have specified for my simulations

⁵<http://flash.uchicago.edu/site/>

in the Config file are Barnes-Hut tree for gravity, sink particles, Polytrope, and the USM MHD solver.

The Simulation_data module stores the data that are specific to the simulation unit. These data are the run-time physical parameters and ultimately will be saved in the output files. In fact, each FLASH unit has its own Unit_data Fortran module to store the data specific for that FLASH unit. All of the variables in this module have a “save” attribute to assure proper storage of the data for that particular variable. Examples of Simulation_data file are provided in the FLASH user manual. The initialization of all the data specified in the Simulation_data is done by the Simulation_init module.

The Simulation_initBlock file needs to be modified to describe the problem that one is trying to study. For example, in my simulations it sets the descriptions for density profiles, velocities, magnetic fields, and etc. This file, in fact, sets the initial conditions (and problem) for each block in the simulation grid. Therefore, the Grid unit calls the Simulation_init module to apply the initial conditions to each block. First the initial conditions are applied to the lowest refinement level (biggest block size), if additional refinement of that block is not needed, the grid unit calls the Simulation_initBlock to initialise the parameters for that block. If the block does require refinement, this process is repeated until the required refinement level is reached. The highest refinement level in my simulations was 0.01 pc for the small filament and 0.004 pc for the large filament. My modifications to the Simulation_initBlock file included scripts to add solid body rotation of the filament, and adjustments to account to the way the USM MHD solver works. Unlike other MHD solvers, the USM solver assigns magnetic field values to the face of the blocks and not their centers.

To *run* FLASH we need an input parameter file (flash.par), an input turbulence file, and a file for submitting the job to the cluster. An example of the flash.par file can be found in the user manual. It should have all the input parameters necessary for the Simulation_initBlock file, and should be present in the run directory. Creation of the turbulence file is explained in Section 5.2.2. This file produces random velocities for each block for the initial FLASH

simulation setup. I will explain the job script file in Section 5.4.

5.4 Computational Resources

FLASH simulations and, indeed, most MHD simulations are computationally intensive and to run them quickly and efficiently, one needs computer clusters so that the computations can be done in parallel. I used clusters associated with *Compute Canada*⁶. Compute Canada’s vision is to ‘make Canada a world leader in the use of advanced computing for discovery and innovation.’ Their team includes ‘more than 200 experts employed by 37 universities and research institutes across Canada’. Their regional organization partners include ACENET, Calcul Québec, Compute Ontario and WestGrid.

I initially used the *General Purpose Cluster*⁷ (GPC) at SciNet⁸. SciNet is Canada’s largest supercomputer center. At the beginning of 2018, the *GPC* started a decommissioning process and *Niagara*⁹ took over the *GPC* in April of 2018. At this time, I switched to the *Cedar* cluster¹⁰ on WestGrid Computing Facilities¹¹ as well as *Niagara* when required.

Running programs (hereafter called *jobs*) on a supercomputer cluster is not the same as running a job on a private desktop computer. In particular, they are not started the instant they are submitted. Instead, they have to wait for the right computational resources to become available. The decision regarding when, and on which CPUs, the job will run is made by a program called a *job scheduler*. A *job scheduler* allocates access to appropriate resources. To communicate with the *job scheduler* and therefore submit one of my simulations a *Batch job script* is required. This *job script* is a file that loads the required modules (e.g., HDF, gcc) before running the job, specifies the required run time, the number of CPUs to be used in parallel, and where the output should be saved. Two common job scheduler software are the

⁶<https://www.computecanada.ca/>

⁷https://support.scinet.utoronto.ca/education/staticpublic/GPC_Quickstart.7.html

⁸<https://www.scinethpc.ca/>

⁹https://docs.scinet.utoronto.ca/index.php/Niagara_Quickstart

¹⁰<https://www.westgrid.ca/support/systems/cedar>

¹¹<https://www.westgrid.ca/support/systems>

Slurm Workload Manager (Slurm) and the *Portable Batch System (PBS)*. *Cedar* and *Niagara* use *Slurm*, while the *GPC* uses *PBS*.

Since I use a resolution of 0.004 pc in my simulations of the large-scale filaments (as opposed to 0.01 pc for the small-scale filaments), the large-scale filaments require much more computational time. For example, simulations of small-scale filaments using 128 CPUs take four to maximum of 12 hours, depending on the initial parameters, to complete a run (which involves forming gravitationally bound cores and allowing the filament time to evolve beyond this stage). A large-scale filament using 128 CPUs, however, takes more than 14 days. This increased run time is mainly due to the longer time required for a large filaments to form cores and the fact that I use a much higher resolution in these simulations. Higher resolution means that, during a run, many more fluid blocks need to be followed and have their physical parameters computed.

In order to ensure that I did not submit jobs that would take an unreasonable amount of time to run, or never complete, prior to submitting jobs with the required resolution I submitted “test” jobs. These test jobs had lower resolution and significantly faster run times which allowed me to experiment with different grid criteria and to check that my modifications to the input files would not end in errors or endless loops. They also allowed me to quickly see how different input parameter and different magnetic field morphologies would affect the output. Once satisfied with my inputs, I would submit jobs with the full required resolution. Over, the course of my thesis, I submitted over 50 jobs to the computational clusters requiring over 400 hours of runtime.

5.5 Running FLASH - The Evolution of the Box

Once the input parameters have been selected, and the required files and modules have been created or modified, the simulations are ready to be run. In this section, I briefly describe the steps that FLASH takes to evolve one of my filaments by following a single fluid cell.

In the first time step, the cell has its physical parameters set by the input files (i.e. it has a density, an initial velocity due to turbulence and rotation, a temperature, a pressure, a magnetic field strength and orientation, and a mass). Then, the FLASH units selected in the Config file (i.e. *Gravity*, *Sink*, *USM MHD*, and *Polytrope*) govern the evolution of the cell.

Gravity governs the overall gravitational collapse of the filament by determining where the cell moves due to its external gravitational forces. If a group of adjacent cells have a density greater than a certain threshold density (combined with additional criteria as explained in Section 5.1.2), they will turn into an individual gravitationally bound core and *Sink* replaces this core with a “sink particle”. The sink particle will move in the simulation box according to external gravity and fluid motion, and its density and mass can continue to increase as it accretes matter.

At the same time that *Gravity* is moving/changing the cells due to gravitational forces, *USM MHD* evolves each cell and the overall system through the equations that describe an MHD fluid (i.e the continuity, momentum, energy conservation, and the induction equations) while satisfying a divergence-free magnetic field. These equations govern how the cell will move and its physical parameters will evolve due to magnetised fluid forces (pressure, velocity, magnetic fields, etc).

Thus, at the end of the first time step, the cell has moved due to the external forces imposed on it by a gravitational, magnetised, fluid. It’s density, mass, velocity, magnetic field, etc. have also been modified. However, the evolution of a cell does not occur in isolation. The FLASH physics solvers coordinate the changes of each cell with the changes of the surrounding cells. In this way, the code ensures that there are no discontinuities in the physical conditions from one cell to the next.

5.6 Results

Using FLASH and the input parameters that I have previously described, in this Section I simulate the evolution of both small and large-scale filaments with a range of rotation frequencies. The goal is to see if the magnetic field reversals observed around the MCs discussed in Chapter 3 can be explained by a helical morphology (as explored in Chapter 4) that would result from the wrapping of the field lines around a rotating filament. Although the magnetic field lines initially could be oriented in any direction with respect to the filament's axis, I explore only two scenarios. The first has the magnetic field lines oriented perpendicular to the long axis of the filament, and the second has the field lines oriented parallel to the long axis. These two orientations affect the behaviour of the fluid elements differently and result in different evolutionary paths. In the sections below, I explore the effects of these different magnetic field orientations on both the small and large scale filaments.

5.6.1 Visualising the Results

To visualise the FLASH HDF output files I use *VisIt*¹² and *The yt project*¹³ (*yt*) tool-kits. *VisIt* was originally developed by the Department of Energy (DOE) Advanced Simulation and Computing Initiative (ASCI) at Lawrence Livermore National Laboratory¹⁴ but is now an open source and interactive analysis tool. It can be used on a personal computer (desktop-sized projects) or on clusters for the analysis of large data-sets. *VisIt* allows for quick 2-D and 3-D visualization and analysis of the data. It can manipulate the data, change viewing angles, and even generate movies of a system's evolution. The *yt project* is an open-source python package for analysis and visualization of volumetric data. It was originally written by Mathew Turk in 2007 to analyze 3D grid-based astrophysical simulation data from his graduate thesis. It now has many co-developers¹⁵.

¹²<https://wci.llnl.gov/simulation/computer-codes/visit/>

¹³<https://yt-project.org/>

¹⁴<https://www.llnl.gov/>

¹⁵A list of members (co-developers) is available here: <https://github.com/yt-project/yt/blob/master/CREDITS>

I used *VisIt* for quick visualization and analysis of my simulation data. However, the figures in this chapter are mostly developed by *yt*, since it is better at producing publication quality images. Outside of *VisIt* and *yt*, I sometimes used FFmpeg¹⁶ and iMovie to make small movies of filament evolution.

5.6.2 Small-Scale Filaments

My small-scale filament is defined as being 1.6 pc long and 0.1 pc wide, with a Plummer-like density profile, using $p = 2$ and $\rho_c = 10^{-19} \text{ g cm}^{-3}$. The temperature is 15 K and the initial average turbulent velocity is 484 m s^{-1} . The magnetic field has a constant strength of $10 \mu\text{G}$. I also explore four different rotation frequencies: $7 \times 10^{-14} \text{ Hz}$, 10^{-12} Hz , 10^{-15} Hz , and 0 Hz (i.e., no rotation, for comparative analysis) to see if rotation speed can affect the magnetic field morphology and cause wrapping of the field lines.

Field Lines Perpendicular to the Filament Long Axis

Rotation frequency of $7 \times 10^{-14} \text{ Hz}$: This rotation frequency is based on actual observations of filament rotation and so should be the best test of “reality”. Since these simulations are in 3D, to analyze and plot the results in 2D, I view the filament with slices that cut through the filament orthogonal to the z-axis as illustrated in Figure 5.3. Figure 5.4 shows the density evolution of the filament with a slice at the center of the z-axis in the x-y plane.

The top panel of Figure 5.4 shows a map of the filament’s density at the start of the simulation (i.e. at time $T = 0$), with a slice orthogonal to $z = 0$. At the first time-step, the filament is perturbed by the initial turbulence spectrum and undergoes solid body rotation. The three other panels show how the filament’s density evolves after 0.16 Myr, 0.4 Myr, and 1.3 Myr. The filament initially expands along its minor axis, due to pressure, while collapsing along its major axis, due to gravity. At the end of the simulation, we can see that two cores are produced, one at each end of the filament, in agreement with previous studies (e.g., Pon

¹⁶FFmpeg is a multimedia framework, able to decode, encode, and transcode.

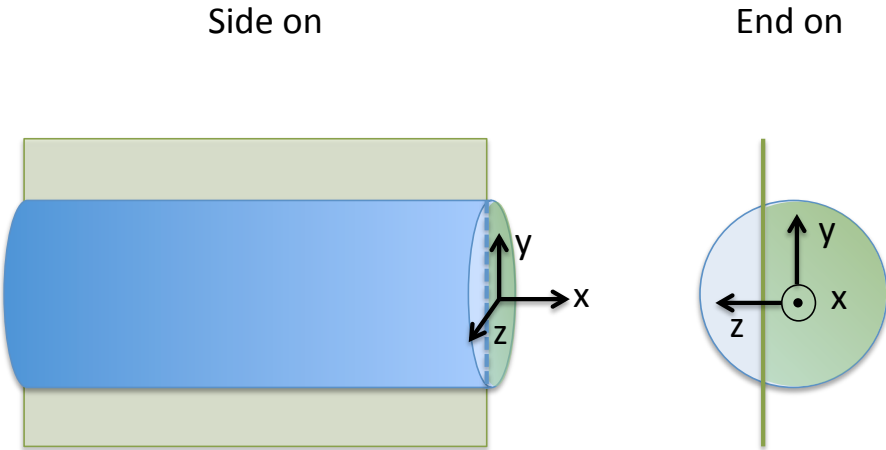


Figure 5.3: (Left) A side-on view of a filament with a slice in the x-y plane, orthogonal to z-axis which points towards the observer. The slice is illustrated by the beige rectangle. (Right) An end-on view of the filament, in the y-z plane. The green line shows the position of the slice seen in the left panel. The slice can be positioned at any point along the z-axis.

et al. 2011, 2012).

During the evolution of the filament, the magnetic field lines rearrange themselves from their initial perpendicular orientation because they are frozen into the moving fluid elements. To study the magnetic field evolution, including searching for evidence of magnetic field reversals, the B_z component of the field needs to be studied at different z-slices and at different times.

Figure 5.5 shows the B_z evolution in the vicinity of the filament with a slice at $z = 0.12$ pc from the filament's centre. Initially the magnetic field lines are in the y-direction and $B_z = 0$ (i.e. the field lines are perpendicular to the filament's long axis). However, due to rotation and the turbulent velocity spectrum, as well as pressure and gravity, the orientation of the field lines begin to change. This is reflected in the B_z component of the field.

As shown in the first panel of Figure 5.5, B_z has a mild reversal along the filament minor axis, where it mostly points in the negative direction at the top of the filament and in the positive direction at the bottom. It also shows a chaotic pattern because of the turbulence.

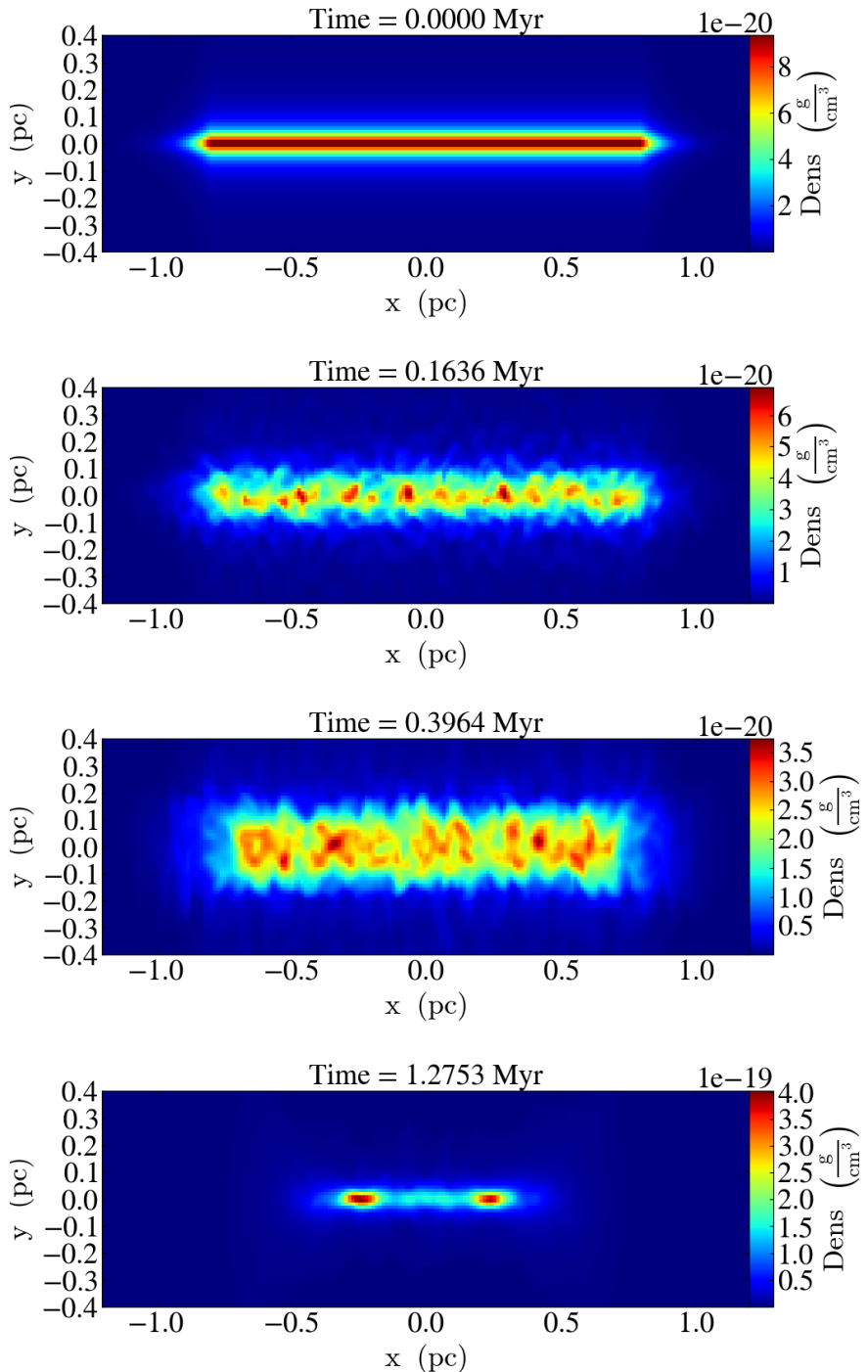


Figure 5.4: Evolution of the density for a small-scale filament with a magnetic field that is initially oriented perpendicular to the long axis (x-axis) of the filament. Each panel represents a slice in the x-y plane, viewed side-on, at $z = 0$ pc, through the centre of the filament. The filament's rotation rate is 7×10^{-14} Hz. Time is indicated at the top of each panel, in units of 10^6 years or Myr. Density is indicated by the color scales to the right of each panel.

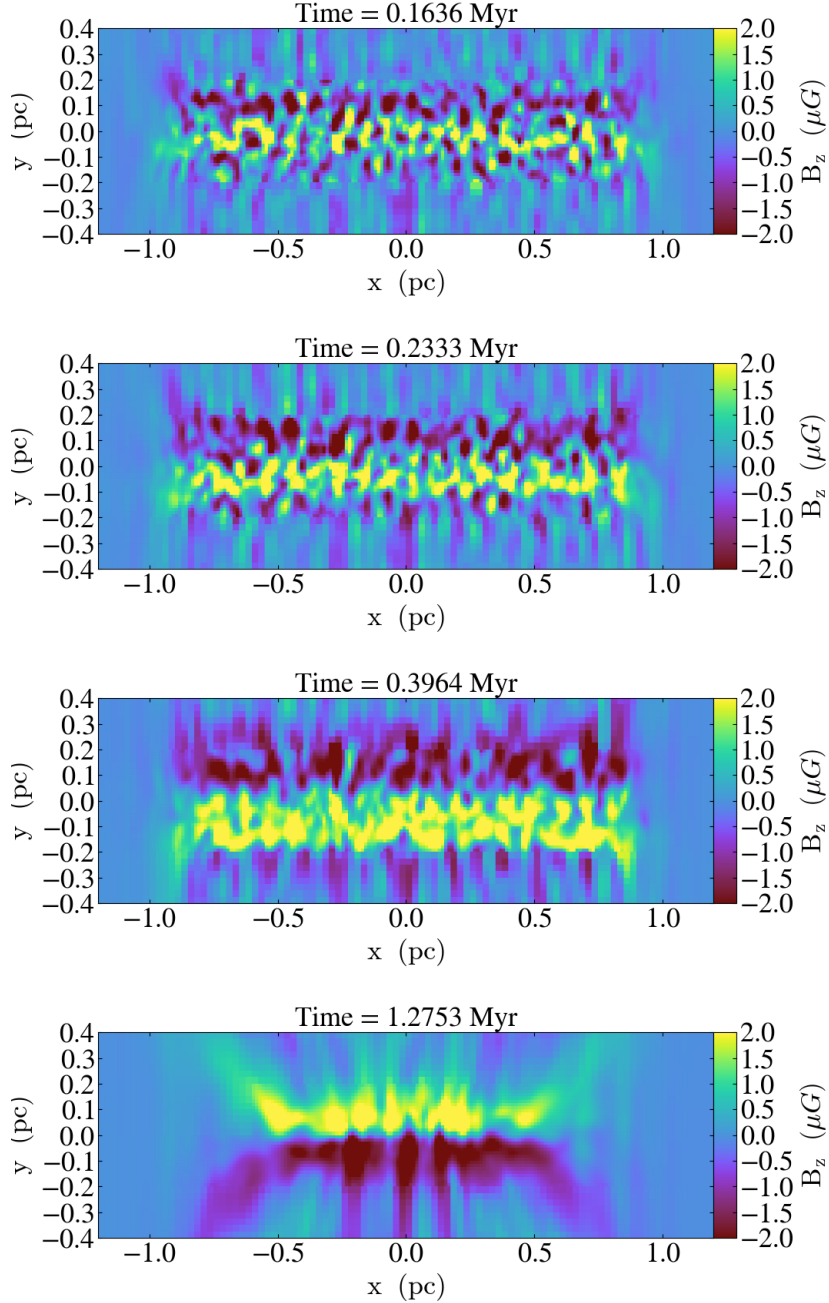


Figure 5.5: Evolution of the z-component of the magnetic field (B_z) for a small-scale filament with a magnetic field that is initially oriented perpendicular to the long axis (x-axis) of the filament. Each panel represents a slice in the x-y plane (i.e. viewed side-on) at $z=0.12$ pc. The filament's rotation rate is 7×10^{-14} Hz. Time is indicated at the top of each panel (in units of 10^6 years or Myr). The magnitude and direction of B_z is indicated by the color scales to the right of each panel. Note that B_z is negative at the top of the filament and positive at the bottom until after 0.4 Myr. In the fourth panel, this direction reverses.

This reversal becomes more pronounced as the filament evolves, as shown in the second and third panels of Figure 5.5.

This reversal in B_z is actually caused by a slight wrapping/bending of the field lines around the filament. This can be seen more clearly in Figure 5.6, which shows the filament in a slice orthogonal to the x-axis, looking at the filament end-on, at $T = 0.4$ Myr. The field lines, illustrated by the arrows, show a small amount of curving from the top of the filament to the bottom. Therefore, if we look at a particular z-slice, in a side-on view like in Figure 5.5, the z-component of the field at the top of the filament will have the opposite direction to that at the bottom. This curvature is likely due to the fact that the pressure initially causes the filament to expand along its minor (x and y) axes and the magnetic field lines get pushed out with it. Note, however, that this bending is in the same direction on both sides of the filament. Therefore, it does not represent an actual helical/toroidal morphology.

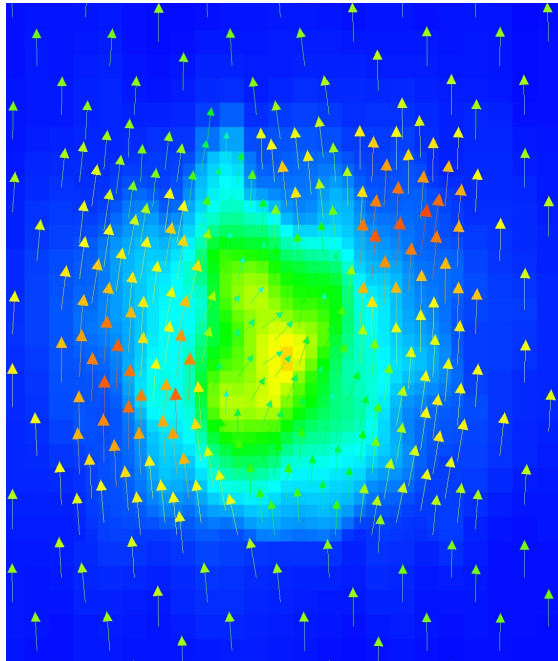


Figure 5.6: Morphology of the magnetic field (represented by arrows) of a small-scale filament with a magnetic field that is initially oriented perpendicular to the long axis (x-axis) of the filament. The filament's rotation rate is 7×10^{-14} Hz. This figure represents a slice in the y-z plane (i.e. viewed end-on) at $T = 0.4$ Myr. The field lines can be seen to curve slightly around the filament due to the pressure expansion of the filament.

As the filament continues to evolve and collapse due to gravity, the orientation of this B_z reversal changes. This can be seen in the bottom panel of Figure 5.5, where B_z now points in the positive direction at the top of the filament and in the negative direction at the bottom of the filament, with a slice in the x-y plane at $z = 0.12$ pc. This second reversal starts forming after $1.5 \times \tau_{ff}$ and is due to the filament's self-gravity becoming the dominant force in its evolution. This is demonstrated in Figure 5.7 which shows the filament in a slice orthogonal to the x-axis at $x = 0$ pc, looking at the filament end-on, at $T = 1.3$ Myr. In this figure the magnetic field lines display the classic "hourglass" morphology that is characteristic of gravitational collapse in a magnetically frozen fluid.

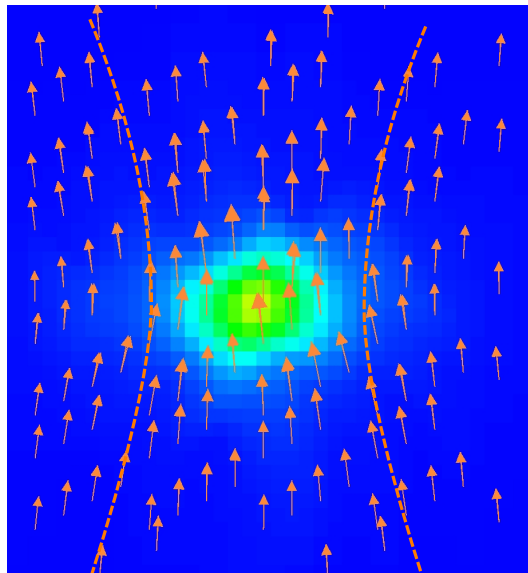


Figure 5.7: Morphology of the magnetic field (represented by arrows) of a small-scale filament with a magnetic field that is initially oriented perpendicular to the long axis (x-axis) of the filament. The filament's rotation rate is 7×10^{-14} Hz. This figure represents a slice in the y-z plane (i.e. viewed end-on) at $T = 1.3$ Myr. The field lines can be seen to pinch towards the centre forming the the classic "hourglass" morphology that is characteristic of gravitational collapse in a magnetically frozen fluid.

To further explore the magnetic field morphology at the end of the simulation, we can examine the filament at different z-slices. Figure 5.8 shows B_z , viewed at different positions along the $\pm z$ axis, at $T = 1.3$ Myr. As we move from the distant environment around the filament to regions closer to the filament itself, we see that the reversal in B_z maintains a

constant direction. In other words, as we move from $z = 0.29$ pc to $z = 0.13$ pc, we see that B_z is positive at the top and negative on the bottom of the filament. However, when we pass $z = 0$ and move away from the filament on the other side, we see that the B_z reversal has an opposite direction to that of $+z$ -layers. More specifically, as we move from $z = -0.13$ pc to $z = -0.29$ pc, we find that B_z is negative at the top and positive on the bottom of the filament. This change in pattern is completely consistent with an hourglass morphology.

This reversal in B_z , however, is only apparent when we examine *slices* of the filament. An observer from Earth, looking down the z -axis, only sees the magnetic field strength integrated along the line of sight. Since the hourglass pinching of the field lines is symmetrical, integrating along the line of sight would cause the B_z direction change to cancel out, and no reversal would be apparent. In any event, it is clear that with these initial parameters, the magnetic field lines do not get fully wrapped around the filament at any time during the simulation.

Rotation frequency of 10^{-12} Hz: To determine whether faster rotation would be able to wrap the field lines around the filament, I use a rotation rate of 10^{-12} Hz, roughly an order of magnitude faster than the previous case. At this rotation frequency, the filament immediately starts expanding and becomes less dense as the fluid elements escape the filament along the minor axes. The simulation then quickly aborts due to this radial escape of material. Figure 5.9 shows the filament at $T = 0.07$ Myr viewed end-on in a slice at $x = 0.31$ pc. As can be seen in this figure, the rapid expansion does cause a distortion of the field lines, which wrap around the filament. As in the case with a rotation of 7×10^{-14} Hz, this wrapping of the field lines is not in one uniform direction (i.e. they do not form a coherent torus around the filament). Therefore, even though we can see reversals in the z -component of the magnetic field by looking at different z -slices, we would not be able to see a reversal in B_z if we integrated along the line of sight.

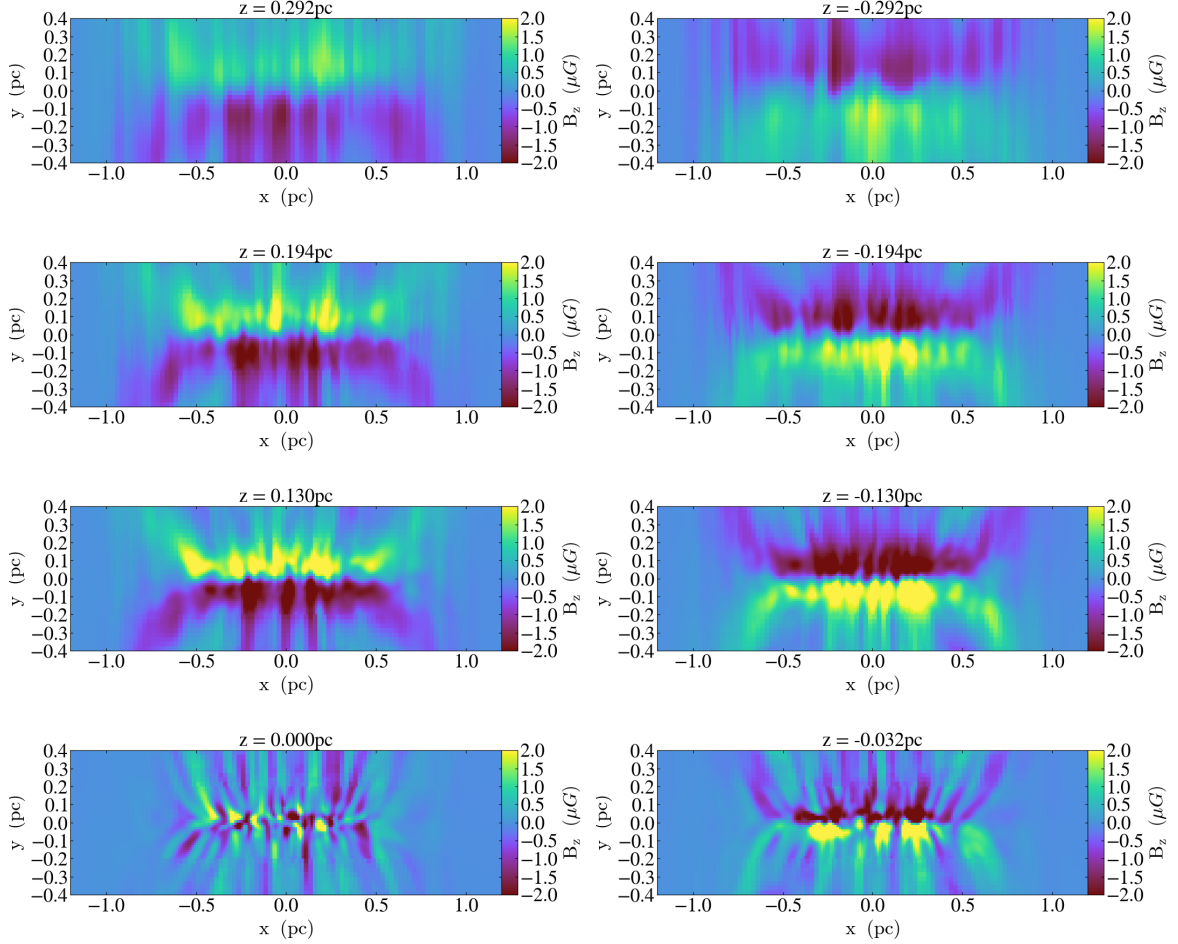


Figure 5.8: The z-component of the magnetic field (B_z) for a small-scale filament with a magnetic field that is initially oriented perpendicular to the long axis (x-axis) of the filament. Each panel represents a slice in the x-y plane (i.e. viewed side-on) at $T = 1.3$ Myr but at different “depths” through the filament along the z-axis. The filament’s rotation rate is 7×10^{-14} Hz. The z-position of each slice is indicated at the top of each panel where positive positions indicate the near side of the filament (with respect to the observer) and negative positions represent the far side of the filament. The magnitude and direction of B_z is indicated by the color scales to the right of each panel. Note that B_z changes direction as one moves from the near side to the far side, due to the hourglass shape of the magnetic field lines caused by gravitational collapse.

Rotation frequencies of 10^{-15} Hz and zero: To explore the effects of pressure on the filament evolution, I lower the rotational frequencies. I first use a rotation of 10^{-15} Hz, an order of magnitude slower than my initial case. I also tested the case where there was neither rotation nor turbulence, without changing any other initial parameters. For the 10^{-15} Hz rotation rate, both the initial curving of the field lines, as seen in Figure 5.6, and the later

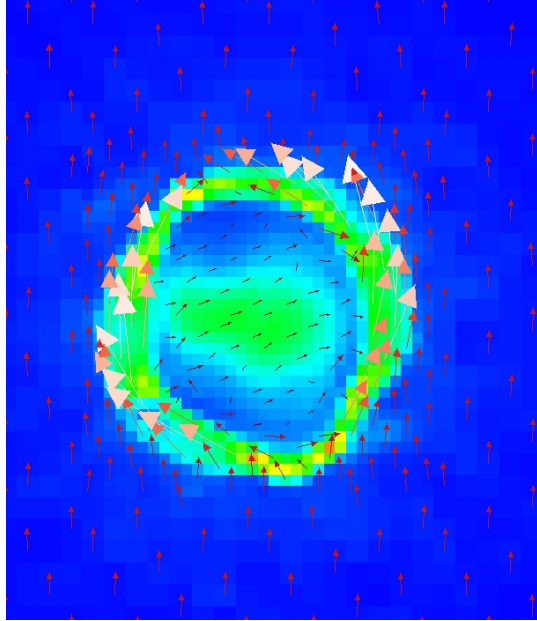


Figure 5.9: Morphology of the magnetic field, represented by arrows, of a small-scale filament with a magnetic field that is initially oriented perpendicular to the long axis (x-axis) of the filament. The filament's rotation rate is 10^{-12} Hz. This figure represents a slice in the y-z plane (i.e. viewed end-on) at $T = 0.07$ Myr. The field lines can be seen to curve slightly around the filament due to the rapid expansion (and eventual dispersal) of the filament.

hourglass shaped pinching of the field lines, as seen in Figure 5.7, occur. The amount of distortion of the field lines and the resulting magnitude of B_z is noticeably smaller than for the 7×10^{-14} Hz rotation rate. For the non-rotating filament with zero turbulence, while there are no small scale perturbations of the field lines (since there is no turbulence), the same large-scale distortions of the field lines occur, but with even weaker effects. This can be seen in Figure 5.10 which shows both a smoother distribution than seen in Figure 5.5 and the two different B_z reversals.

It is interesting to note that the first reversal in B_z , caused by the initial curving of the field lines around the filament (illustrated in Figure 5.6), is present in these simulations, both in the 10^{-15} Hz case and in the 0 Hz with the absence of turbulence. Therefore, I suggest that this first distortion of the field lines is, indeed, caused by the expansion of the filament due to pressure. As with the filament with a 7×10^{-14} Hz rotation rate, the second reversal in B_z occurs when the filament has evolved past the free-fall time and the magnetic field lines

display the classic hourglass shape when viewed end-on. This is again due to the filament's self-gravity becoming the dominant force in its evolution.

At no time in any of these simulations does the magnetic field become fully wrapped around the filament, regardless of the rotation rate. In fact, none of my simulations that begin with the magnetic field oriented perpendicular to the filament's long axis have been able to produce a toroidal or helical magnetic field. Next, I explore the results with a magnetic field initially oriented parallel to the long axis of the filament.

Field Lines Parallel to the Filament Long Axis

The initial parameters for these simulations are the same as before. The filament is defined as being 1.6 pc long and 0.1 pc wide, with a Plummer-like density profile, using $p = 2$ and $\rho_c = 10^{-19} \text{ g cm}^{-3}$. The temperature is 15 K and the initial average turbulent velocity is 484 m s^{-1} . The magnetic field has a constant strength of $10 \mu\text{G}$. I also explore three different rotation frequencies: $7 \times 10^{-14} \text{ Hz}$, 10^{-15} Hz , and 10^{-12} Hz . The only difference from the previous simulations is that the magnetic field is initially aligned *along* the long axis of the filament and I do not examine the case of zero rotation and zero turbulence.

Rotation frequencies of $7 \times 10^{-14} \text{ Hz}$ and 10^{-15} Hz : I first investigate the evolution of the filament with a rotation frequency of $7 \times 10^{-14} \text{ Hz}$, based on the observed rotation rates of filaments. I then reduce the rotation frequency to 10^{-15} Hz to study the effects of slower rotation. Both of these rotation rates result in very similar density evolution and magnetic field morphology and so I discuss them together.

Figure 5.11 shows the evolution of the density structure for the first 0.9 Myr, using a rotation of 10^{-15} Hz . Figure 5.12 shows the evolution of B_z in a 2D slice in the x-y plane (i.e. looking at the filament side-on) located at $z = 0.12 \text{ pc}$ from the filament's centre. The evolution of the density structure is similar to that of the case in which the magnetic field is oriented perpendicular to the long axis of the filament except that the gravitationally bound

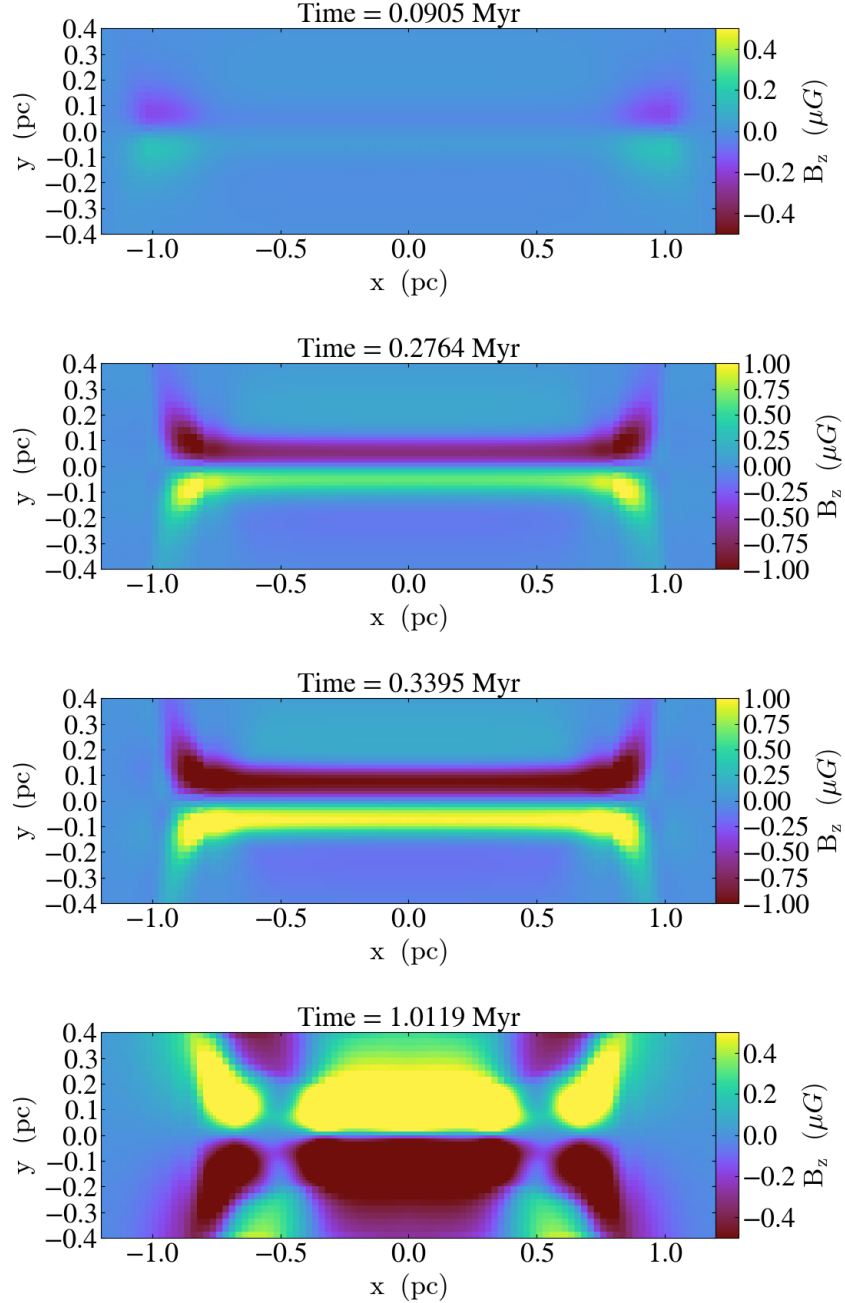


Figure 5.10: Evolution of the z -component of the magnetic field (B_z) for a small-scale filament with a magnetic field that is initially oriented perpendicular to the long axis (x-axis) of the filament, without the presence of initial turbulence or rotation. Each panel represents a slice in the x-y plane (i.e. viewed side-on) at $z = 0.12$ pc. The filament has zero rotation and zero turbulence. Time is indicated at the top of each panel (in units of 10^6 years or Myr). The magnitude and direction of B_z is indicated by the color scales to the right of each panel. Note that B_z is negative at the top of the filament and positive at the bottom until after 0.3 Myr, when this direction reverses.

cores form more quickly (i.e at 0.9 Myr instead of 1.3 Myr). The evolution of the magnetic field, however, is quite different. Figure 5.12 shows that the z-component of the magnetic field looks perturbed and chaotic at all times. No overall large-scale patterns form and no strong reversals in B_z are detected at any time, or in any region of the filament. An exception to this latter statement is, perhaps, a poorly organised pattern in which the left side of the filament seems to have more negative values for B_z , compared to the right side where B_z seems to be more positive.

Rotation frequency of 10^{-12} Hz: At high rotation frequency rates (10^{-12} Hz), the filament becomes distorted and expands almost immediately. This can be seen in Figure 5.13 which shows the density evolution of this filament over the first 0.15 Myr and illustrates this rapid expansion along the minor axes. Eventually, the filament vanishes due to this expansion.

During this rapid evolution, the magnetic field lines also become distorted. This can be best seen by looking at the filament in slices orthogonal to the x-axis (i.e. end-on). Figure 5.14, shows the filament at $T = 0.11$ Myr in slices at $x = 0.34$ pc (left panel) and $x = 0.31$ pc (right panel). This figure shows that the magnetic field morphology is complex and changes rapidly with position. The left panel, shows that the magnetic field lines at the edge of the filament generally have a counter-clockwise direction. This suggests that some degree of wrapping of the field lines into a toroidal/helical morphology is feasible. However, the right panel shows that, in an adjacent region, the orientation of the magnetic field changes direction completely, and the magnetic field lines at the edge of the filament now generally have a clockwise direction. Thus, this simulation does not produce an orderly wrapping of the magnetic field lines around the filament in such a way that a uniform torus or helix is created. Instead, it seems to produce wrapping of the field lines around individual sub-regions produced by the complex density structure. It certainly does not produce any kind of stable field since the filament itself rapidly disperses due to the high rotation rate.

Therefore, like in the case where the magnetic field is oriented perpendicular to the

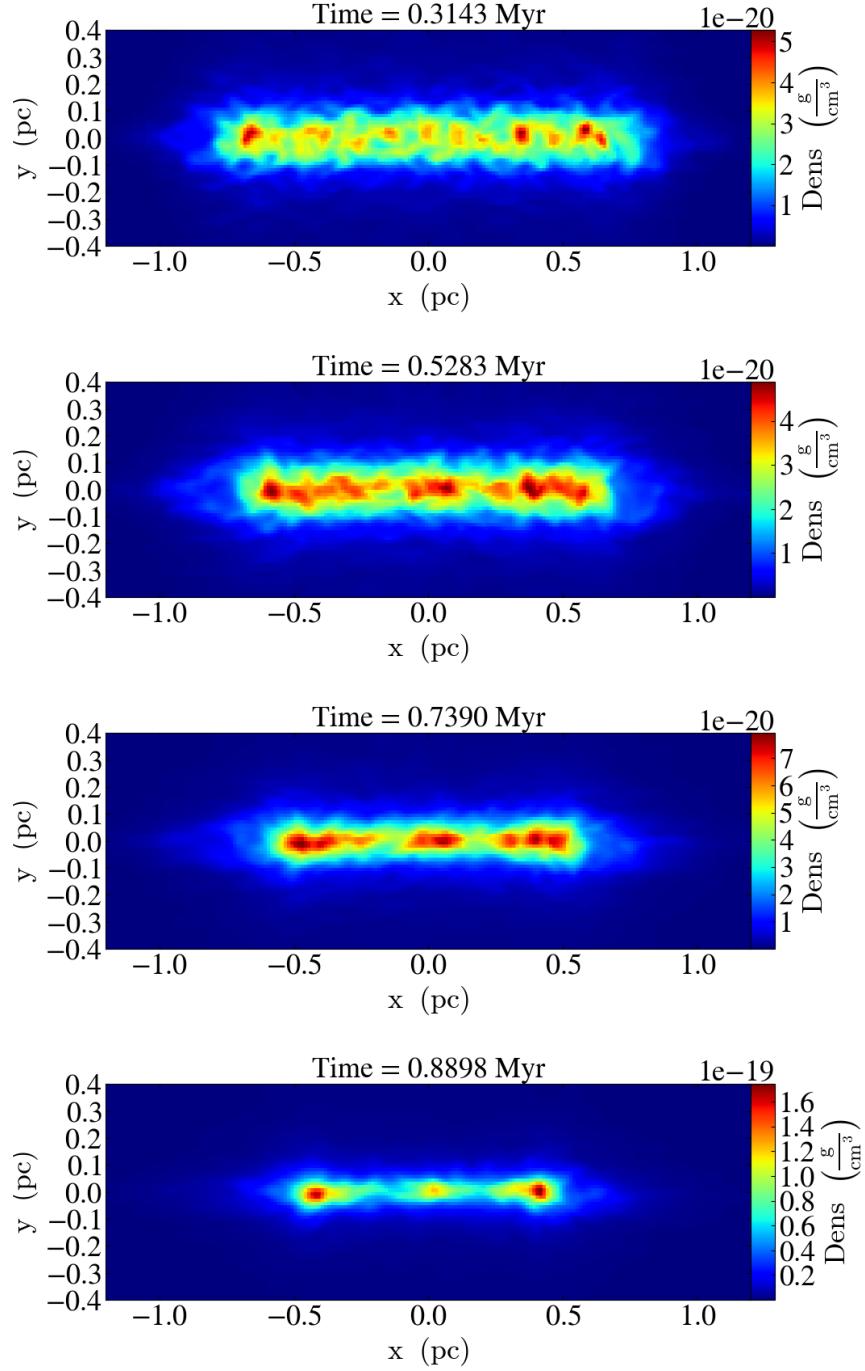


Figure 5.11: Evolution of the density for a small-scale filament with a magnetic field that is initially oriented parallel to the long axis (x-axis) of the filament. Each panel represents a slice in the x-y plane (i.e. viewed side-on) at $z = 0$ pc (i.e. through the centre of the filament). The filament's rotation rate is 10^{-15} Hz. Time is indicated at the top of each panel (in units of 10^6 years or Myr). Density is indicated by the color scales to the right of each panel.

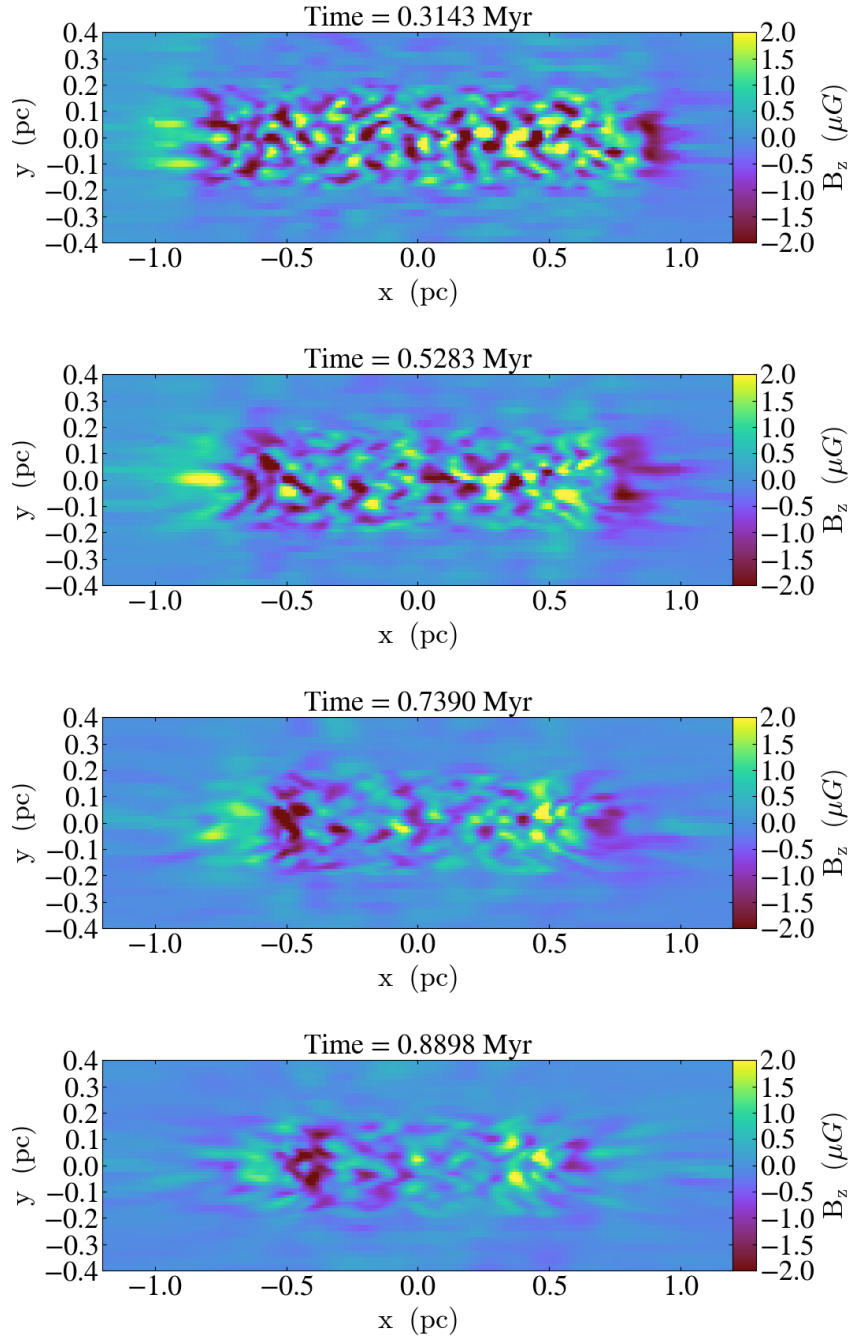


Figure 5.12: Evolution of the z-component of the magnetic field (B_z) for a small-scale filament with a magnetic field that is initially oriented parallel to the long axis (x-axis) of the filament. Each panel represents a slice in the x-y plane (i.e. viewed side-on) at $z=0.12$ pc. The filament's rotation rate is 10^{-15} Hz. Time is indicated at the top of each panel (in units of 10^6 years or Myr). The magnitude and direction of B_z is indicated by the color scales to the right of each panel.

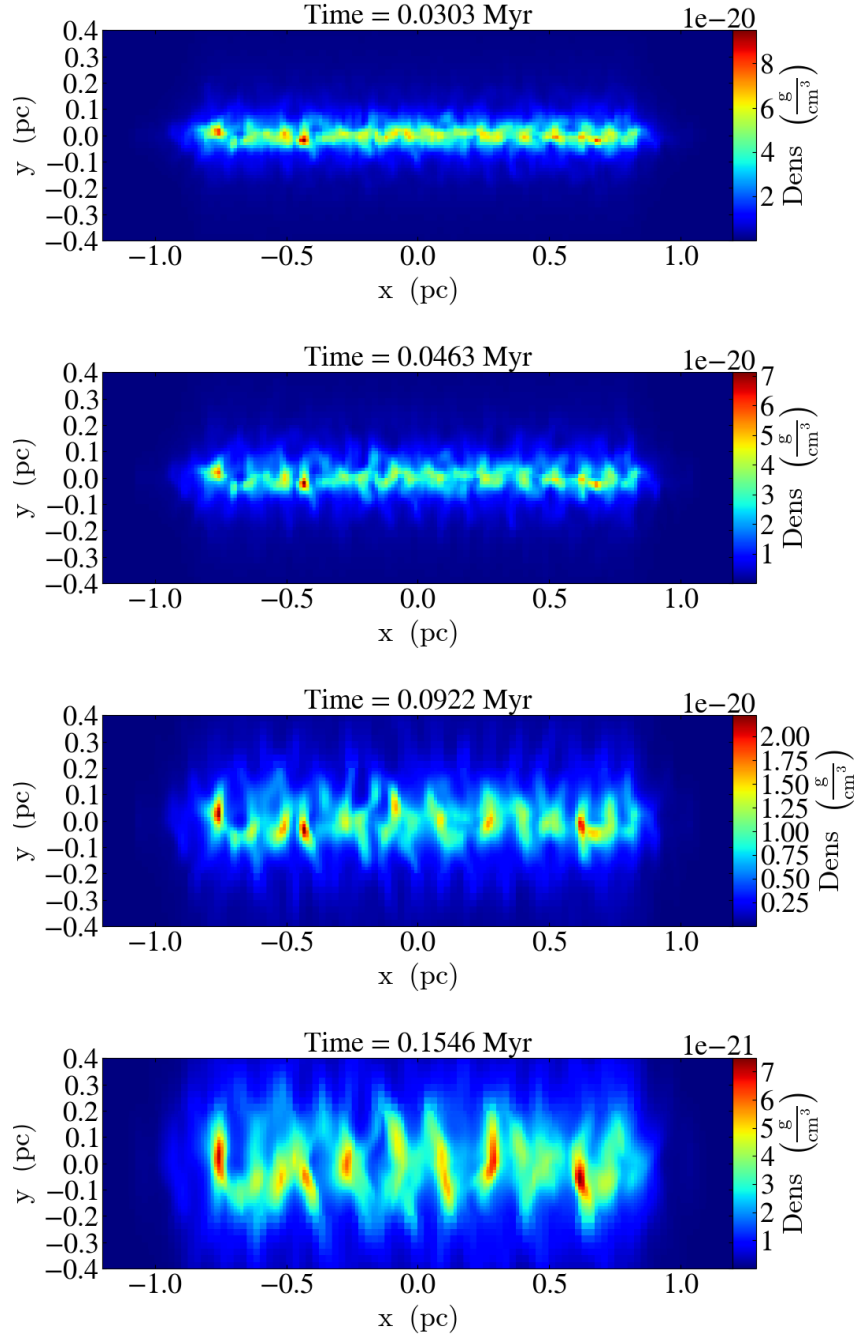


Figure 5.13: Evolution of the density for a small-scale filament with a magnetic field that is initially oriented parallel to the long axis (x-axis) of the filament. Each panel represents a slice in the x-y plane (i.e. viewed side-on) at $z=0$ pc (i.e. through the centre of the filament). The filament's rotation rate is 10^{-12} Hz. Time is indicated at the top of each panel (in units of 10^6 years or Myr). Density is indicated by the color scales to the right of each panel. The filament rapidly expands and disperses due to the high rotation rate.

long axis of the filament, in this case (where the magnetic field is oriented parallel to the long axis of the filament), my simulations are unable to produce an orderly and stable toroidal or helical magnetic field morphology. It is possible, however, that filaments with such small dimensions (i.e. 1 pc by 0.1 pc) are unable to produce these types of magnetic field morphologies. Therefore, in the next Section, I investigate the evolution of a large-scale filament resembling a real object - like Orion A.

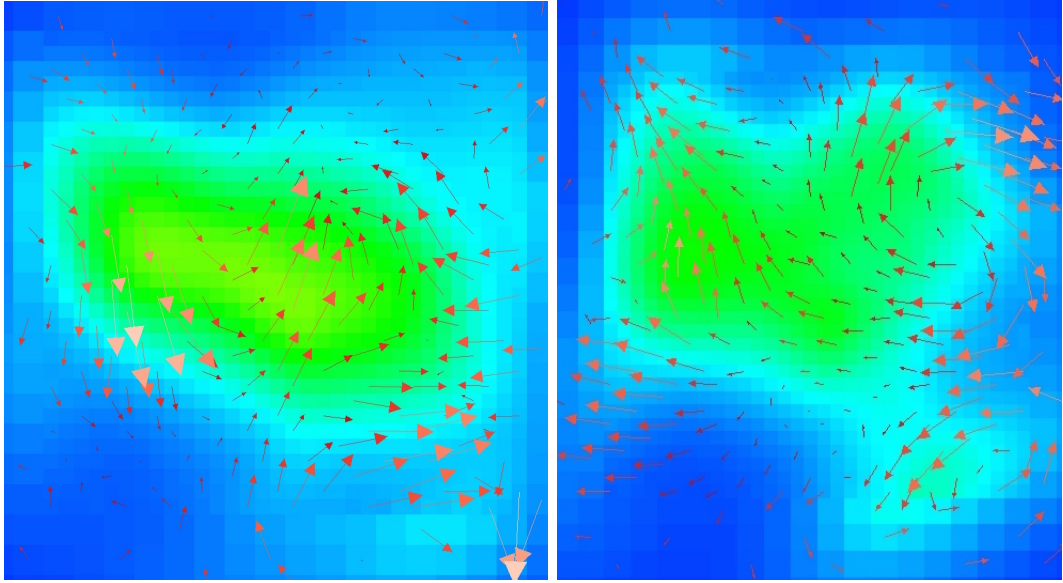


Figure 5.14: Morphology of the magnetic field (represented by arrows) of a small-scale filament with a magnetic field that is initially oriented parallel to the long axis (x-axis) of the filament. The filament's rotation rate is 10^{-12} Hz. The left panel represents a slice in the y-z plane (i.e. viewed end-on) at $x = 0.34$ pc and $T = 0.11$ Myr. The right panel is a similar slice at $x = 0.31$ pc and the same time. The magnetic field lines change from one slice to the next indicating a complex and rapidly changing morphology.

5.6.3 Large-Scale Filaments

My large-scale filament is defined as being 37 pc long and 1.5 pc wide. It also obeys a Plummer-like density profile, with $p = 2$ and $\rho_c = 3.9 \times 10^{-22} \text{ g cm}^{-3}$. The length of the simulation box is 50 pc and the width of the box is 16.7 pc. The temperature is 15 K and the initial average turbulent velocity is 749 m s^{-1} . The initial magnetic field is $10 \mu\text{G}$ and uniformly perpendicular to the filament. The rotation frequency is $5 \times 10^{-15} \text{ Hz}$. These

simulations take over two weeks to run. Therefore, due to time limitations, this is the only set of parameters I was able to investigate.

Figure 5.15 shows the density evolution of this filament in a slice in the x-y plane at $z = 0$ at four different times, up to a maximum of 0.3 Myr. While the filament can be seen to be collapsing during this time, no real density pattern forms. Instead, the density field seems “noisy” and chaotic. No gravitationally bound cores have formed by the end of the simulation, but that may be due to insufficient time. Unfortunately, after 10 days of actual computational time, my cluster time-allocation priority was significantly reduced, and this simulation was not able to be completed.

Figure 5.16 shows the evolution of the z-component of the magnetic field in slices in the x-y plane at $z = 0.1$ pc. Like the density structure, no pattern emerges in the magnetic field and it also look “noisy” and chaotic. In both cases, this lack of organised structure is probably due to the dominant role that turbulence plays in this filament. The initial average velocity of the fluid elements is 0.75 km s^{-1} which is $\sim 50\%$ larger than that of the small filaments in my simulations. Therefore, in this investigation of a single large-scale filament, I am also unable to produce an organised wrapping of the magnetic field lines around the filament or the observed reversal in the direction of the z-component of the field.

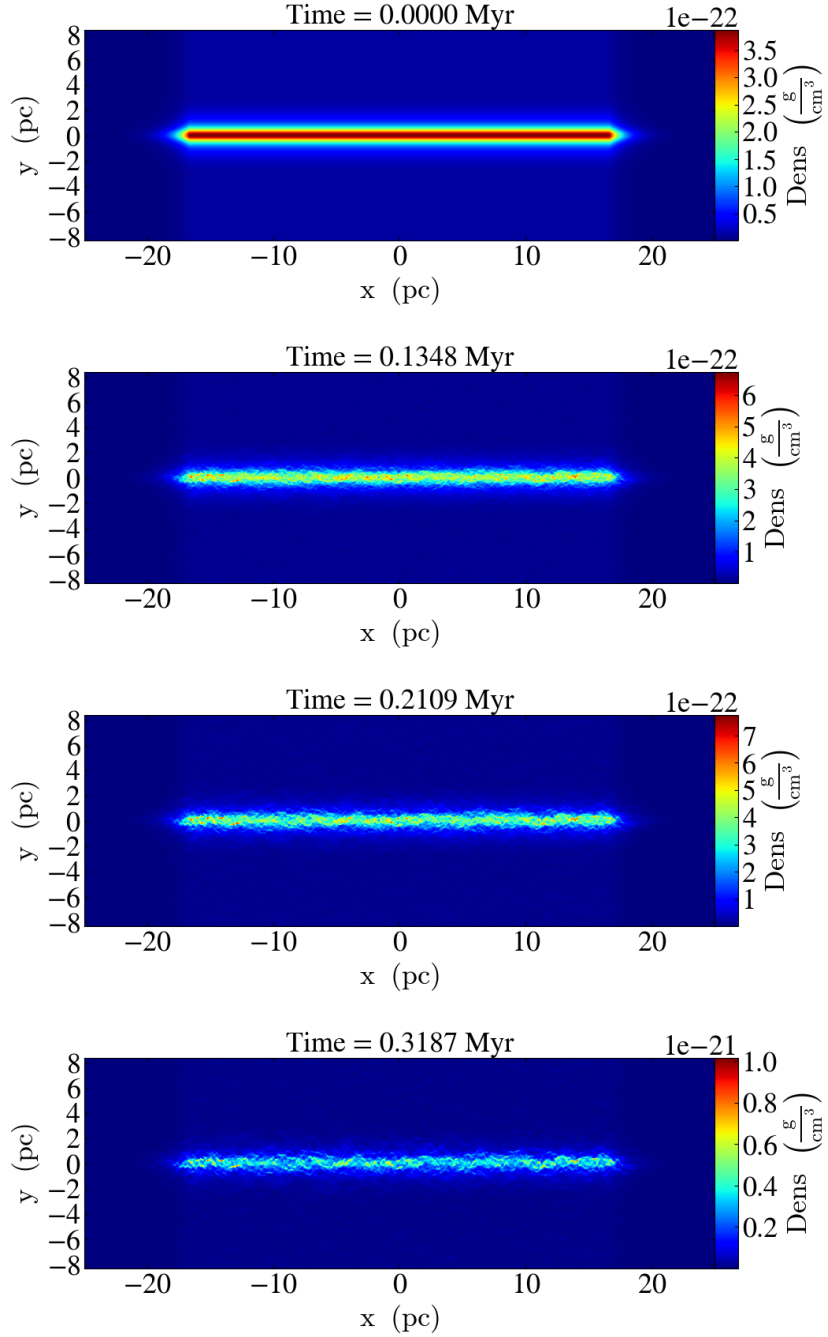


Figure 5.15: Evolution of the density for a large-scale filament with a magnetic field that is initially oriented perpendicular to the long axis (x-axis) of the filament. Each panel represents a slice in the x-y plane (i.e. viewed side-on) at $z = 0$ pc (i.e. through the centre of the filament). The filament's rotation rate is 5×10^{-15} Hz. Time is indicated at the top of each panel (in units of 10^6 years or Myr). Density is indicated by the color scales to the right of each panel. Simulation only runs to $T = 0.3$ Myr due to the priority of the job being reduced after 10 days of computational time.

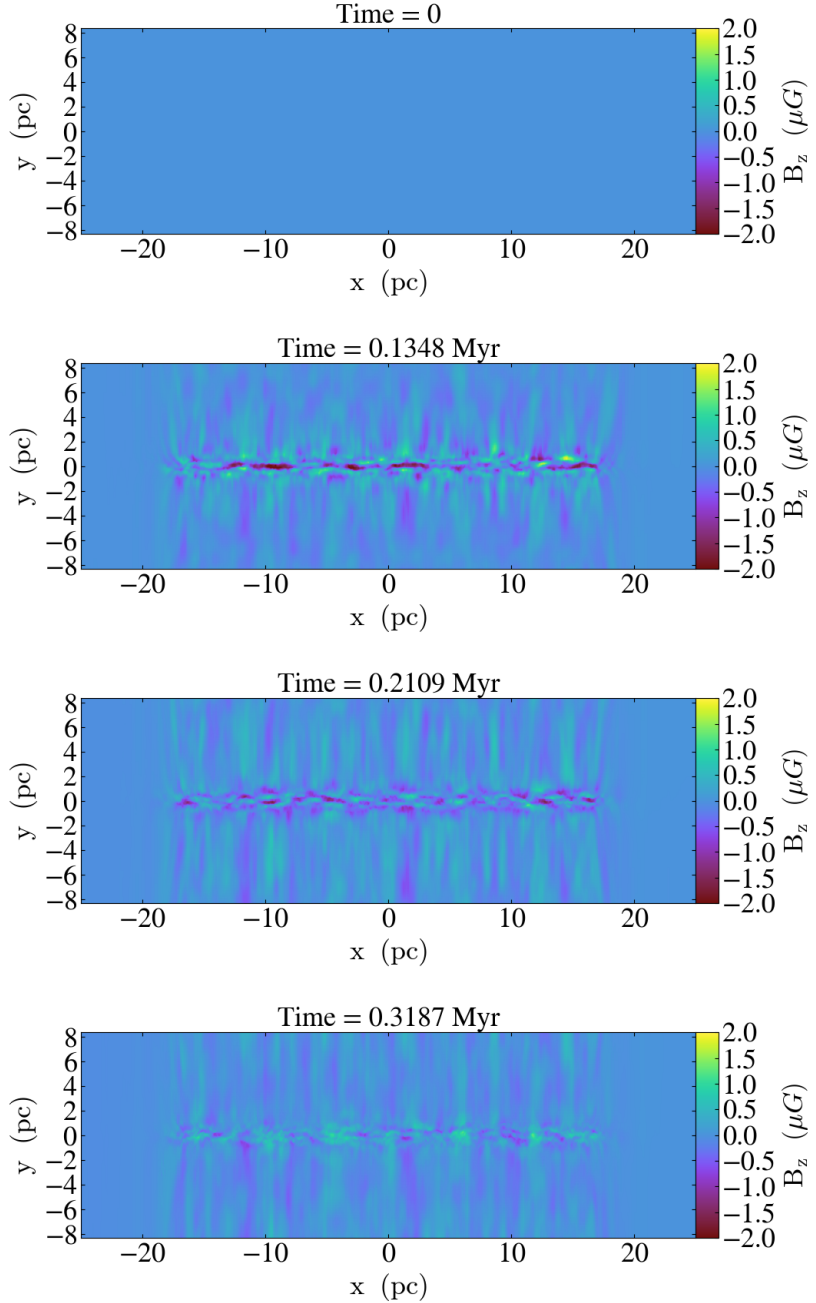


Figure 5.16: Evolution of the z-component of the magnetic field (B_z) for a large-scale filament with a magnetic field that is initially oriented perpendicular to the long axis (x-axis) of the filament. Each panel represents a slice in the x-y plane (i.e. viewed side-on) at $z = 0.1$ pc. The filament's rotation rate is 5×10^{-15} Hz. Time is indicated at the top of each panel (in units of 10^6 years or Myr). The magnitude and direction of B_z is indicated by the color scales to the right of each panel. Simulation only runs to $T = 0.3$ Myr due to the priority of the job being reduced after 10 days of computational time. Over this time, no organised pattern in B_z emerges.

5.7 Discussion

In this chapter I presented simulations of small- and large-scale filaments. For the small-scale filaments, I used magnetic field lines that were both perpendicular and parallel to the long axis of the filament and I explored different rotation rates. For the large-scale filament I was only able to examine one set of initial conditions: a single rotation rate and a magnetic field that was initially perpendicular to the filament.

I found that, for 1) the large-scale filament and for 2) the small-scale filament with magnetic field lines parallel to the filament's long axis, no organised, large-scale pattern in the magnetic field morphology emerged. In these cases, the magnetic field was chaotic in structure and its evolution was dominated either by turbulence or high rotation rates.

In the case of the small-scale filaments with the magnetic field oriented perpendicular to the long axis of the filament, two large-scale patterns emerge in the magnetic field morphology. At early times in the simulations, the magnetic fields become slightly curved around the edges of the filament due to pressure expansion. At later times, when gravity dominates causing the filament to collapse along its minor axis, the magnetic field lines become pinched into an hourglass shape. At both these times, 2D slices of the filament in the x-y plane (i.e. seen side on) reveal apparent reversals in the direction of the z-component of the magnetic field. However, since these magnetic field morphologies are symmetric on the front and back side of the filament, integrating the z-component of the magnetic field along the z-axis (i.e. along the line of sight to the observer) would result in a net B_z of zero.

Thus, none of my simulations were able to produce a coherent toroidal or helical structure for the magnetic field resulting from the field lines becoming wrapped around the filament. Nor, in fact, was I able to produce any kind of magnetic field morphology that would result in the observed reversals in B_z seen in the data in Chapter 3.

We can, perhaps, understand these results by considering how much wrapping of the field lines could be expected in my simulations. To do this, I compare the time-scales of the main mechanisms which govern the filament's evolution. These are: the free-fall time (τ_{ff}) due

to the filament's self-gravity, the time for one full rotation of the filament (T_{rot} ; rotation period), and the turbulence time-scale (t_{turb}). This comparison will help determine which of the mechanisms are likely to dominate the evolution of the magnetic field lines and, as a result, what magnetic field morphology could be expected by the end of the simulations.

The free-fall time (τ_{ff}) is the time that it takes the system to undergo gravitational collapse in the absence of pressure. It is used as a proxy for the time to form cores and stars. In a spherical cloud, τ_{ff} can be determined from:

$$\tau_{ff} = \sqrt{\frac{3}{32\pi G\rho}}, \quad (5.9)$$

where G is the gravitational constant and ρ is the volume density of the system. Assuming that the free-fall time along the minor axis of a filament approximates that of a sphere, for the small-scale filaments, with a central Plummer density of $10^{-19} \text{ g cm}^{-3}$, the τ_{ff} is found to be $6.7 \times 10^5 \text{ yr}$. For the large-scale filaments, with $\rho_c = 3.9 \times 10^{-22} \text{ g cm}^{-3}$, the τ_{ff} is found to be $1.1 \times 10^6 \text{ yr}$.

The rotation period of the filaments can be obtained from the rotation frequency, f_{rot} (i.e. $T_{rot} = \frac{1}{f_{rot}}$). For the rotation frequencies used in my simulations (i.e. $f_{rot} = 10^{-12} \text{ Hz}$, $7 \times 10^{-14} \text{ Hz}$, 10^{-15} Hz , and $5 \times 10^{-15} \text{ Hz}$), the rotation periods are $3.2 \times 10^4 \text{ yr}$, $4.5 \times 10^5 \text{ yr}$, $3.2 \times 10^7 \text{ yr}$ (for the small-scale filament), and $6.3 \times 10^6 \text{ yr}$ (for the large-scale filament).

The time that it takes the large eddies to undergo significant distortion is known as turbulence time-scale or the *eddy turnover time*. To calculate this turbulence time-scale, I use the following relationship

$$t_{turb} = \frac{\lambda_{max}}{v}, \quad (5.10)$$

where v is the average fluid element velocity and λ_{max} is the length-scale of the large eddies, i.e., the filament's width. For a small-scale filament with a width of 0.1 pc and a fluid element velocity of 484 m s^{-1} , t_{turb} is found to be $2.0 \times 10^5 \text{ yr}$. For a large-scale filament with a width of 1.49 pc and a fluid element velocity of 749 m s^{-1} , t_{turb} is found to be $1.9 \times 10^6 \text{ yr}$. I have

listed all the time-scales for both the small-scale and large-scale filaments in Table 5.1.

Filament	Time-scale [yr]	Free-fall	Rotation	Turbulence
Small-Scale		6.7×10^5	4.5×10^5	2.0×10^5
Large-Scale		1.1×10^6	6.3×10^6	1.9×10^6

Table 5.1: Time-scales of the main mechanisms governing the evolution of the field lines in both the small- and large-scale filaments. The numbers are for a small-scale filament of 0.1 pc wide, with rotation frequency of 7×10^{-14} Hz and average turbulence velocity of 484 m s^{-1} , and a large-scale filament of 1.5 pc wide, with rotation frequency of 5×10^{-15} Hz and average turbulence velocity of 749 m s^{-1} .

For a small-scale filament, the observed T_{rot} of 4.5×10^5 yr and the free-fall time (τ_{ff}) of 6.7×10^5 yr are comparable. Thus, in one free-fall time, the filament has had time to undergo one full rotation. This *might* be sufficient time to wrap the frozen-in field lines around the filament if there were no other fluid motions. The turbulence time-scale (t_{turb}) of 2.0×10^5 yr, however, is smaller than both the free-fall time and the rotation period. Thus, in one free-fall time and one rotation, the turbulence eddies have had time to become significantly distorted from their initial state. This suggests that the frozen-in field lines are more likely to form a perturbed morphology dominated by turbulence, rather than an ordered morphology dominated by rotation.

This is effectively what we see in my simulations. For the slower rotation rates, the magnetic field morphology is not dominated by rotation or gravity but, rather, by pressure expansion and turbulence. However, at later times, once the simulation exceeds the free-fall time the magnetic field morphology is dominated by gravity rather than by turbulence or rotation. Faster rotation, might allow the field lines to wrap around the filament more efficiently and quickly. But it is clear from my simulations that, rotation rates that are too high, cause the filament to break up and disperse. More investigation into rotation frequencies between 7×10^{-14} and 10^{-12} Hz are needed to see if there is a rotation rate that can dominate the evolution of the magnetic field morphology without causing destruction of the filament. It would also be useful to explore how stronger initial magnetic field strengths would affect

the evolution of its morphology.

For a large-scale filament, with T_{rot} of 6.3×10^6 yr, τ_{ff} of 1.1×10^6 yr, and t_{turb} of 1.9×10^6 yr, the rotation time-scale is longer than the free-fall time. As a result, during one free-fall time it does not even complete one full rotation. Thus, the large filaments probably do not have enough time for the field lines to wrap around it before it collapses. Clearly, however, a much wider exploration of parameter space is required to understand the evolution of these large filaments.

In conclusion, based on my simulations, it seems that it is not easy to produce toroidal or helical magnetic fields on pre-existing filaments via rotation. This result supports my conclusion in Chapter 4 that a bow-shaped morphology is a more natural interpretation of the observed magnetic field reversals seen in the data in Chapter 3.

Chapter 6

Summary and Conclusion

My PhD thesis, both theoretically and observationally, focuses on the role of magnetism in the evolution of dense filamentary structures. Theoretical models, along with observations, suggest that magnetic fields are dynamically important in the evolution of filamentary structures, based on their strength and orientation relative to the star-forming filamentary structures (eg., Planck Collaboration et al. 2016; Li et al. 2017; Seifried and Walch 2015). Determining the role of magnetism in star formation requires careful theoretical and observational investigation and constant efforts to develop novel observational techniques.

6.1 Summary

I proposed and demonstrated a new method to use Faraday rotation measurements in and around filamentary molecular clouds that are forming stars, to find the direction and magnitude of the component of magnetic field along the line of sight. I applied my proposed method in four relatively nearby regions: Orion A, Orion B, Perseus, and California. I used rotation measure data from the literature and adopted a simple approach based on relative measurements, to decouple the rotation measure contributions from the molecular clouds versus the Galaxy. I then used a chemical evolution code along with extinction maps of each cloud to find the electron column density of the molecular cloud at the position of each

rotation measure data. Combining the rotation measures produced by the molecular clouds and the electron column density, I calculated the line-of-sight magnetic field strength and direction. In the vicinity of available molecular Zeeman measurements in Orion A, Orion B, and Perseus, I found magnetic field values of $-23 \pm 38 \mu\text{G}$, $-129 \pm 28 \mu\text{G}$, and $32 \pm 101 \mu\text{G}$, respectively, which were in agreement with the molecular Zeeman measurements.

In California and Orion A regions, I found clear evidence that the magnetic fields at one side of these filamentary structures were pointing towards us and were pointing away from us at the other side. This change of magnetic field direction across filamentary structures had been previously detected in only the Orion A region (Heiles 1997) and had been investigated in theoretical and some indirect observational studies. While the magnetic fields in Perseus might seem to suggest the same behavior, not enough data were available to draw such conclusions. In Orion B, as well, there were not enough data available to infer such behavior.

Three magnetic field morphologies that are often proposed to explain this change of direction across filamentary structures are: toroidal, helical, and bow morphologies. To distinguish between these three morphologies, I constructed three dimensional vectors using my line-of-sight components of magnetic field and the plane-of-sky components from the Planck Collaboration et al. (2016). I then constructed models representing the three morphologies and compared the models with the observations. I suggest that the toroidal morphology is the least probable morphology and that the bow morphology is a natural interpretation to explain this direction change in Orion A.

To investigate these morphologies further, I theoretically studied the evolution of an already formed filament with parallel or perpendicular (to the filament long axis) initial magnetic fields, using an MHD simulation code. In these simulations I examined the influences of input parameters on the evolution of magnetic field lines, while keeping the effects of environment minimised. Exploring different initial parameters, such as filament rotation, allowed for investigating the possibility of formation of magnetic field reversals or helical fields around the filament. In these simulations I found that, at different sections of a filament

with an initially perpendicular magnetic field, the line-of-sight component of the magnetic field changed direction from one side of the filament to the other. This reversal, however, did not represent an actual wrapping of the field lines around the filament, nor did it generate a toroidal or helical field morphology. I conclude that toroidal or helical fields are not easily generated in a pre-existing filament due to rotation. This supports my conclusion that a bow-shaped morphology is the most natural explanation for the observed magnetic field reversals.

6.2 Major Contributions

In summary, my thesis consists of observational analysis, combining observational results with theoretical modeling, and MHD simulations of the co-evolution of magnetic fields and filamentary MCs. The major contributions of my thesis are as follows:

- Proposing a viable new method to detect the line-of-sight component of magnetic fields within filamentary molecular clouds.
- Mapping the line-of-sight component of the magnetic field in Orion A, Orion B, California, and Perseus molecular clouds using my new method. I found my observations to be consistent with available molecular Zeeman measurements. Additionally, I found clear evidence that the direction of the line-of-sight component of the magnetic field reversed from one side of the filamentary structure to the other in Orion-A and California.
- Determining that for the Orion A region the bow morphology was a more natural interpretation and that the helical and the bow were both more probable than a toroidal morphology. I reached this conclusion by combining my magnetic field results with those of Planck and then constructing theoretical models that I compared to these observations.
- Concluding that helical or toroidal fields are not easily produced in already-formed

filaments. I made this conclusion through numerical (MHD) and analytical investigations of filaments with different initial parameters for their physical structure, rotation, and magnetic fields.

6.3 Future Work

To find and investigate the most probable magnetic field morphologies in filamentary molecular clouds, both theoretical and observational studies are necessary. Further observational studies with an increased number of rotation measure data (and with higher sensitivity) would improve our ability to map and interpret the large-scale 3D structure of the magnetic fields. Theoretical simulations would help us understand the origin of these magnetic field morphologies and how they can affect the evolution of the filaments and the subsequent formation of stars within them.

6.3.1 Observations

Future observational work that would contribute to our understanding of magnetic field morphology in star-forming filaments can be done in three main categories: 1) obtaining more B_{LOS} measurements using the method presented in Chapter 3, 2) upgrading my method, and 3) combining B_{LOS} with B_{POS} results in different regions.

1) More B_{LOS} data and regions: More data will be available with future RM catalogs such as POSSUM and VLASS, which will provide better-sampled maps of the large-scale 3D and B_{LOS} magnetic field morphologies of filamentary MCs. Additionally, the uncertainties of RM data in these new surveys will be reduced, since they will have several observing bands, as opposed to Taylor et al. (2009), where two observing bands plus knowledge of the fractional polarisation were used. This will improve the sampling and accuracy of the inferred magnetic field strengths.

Since the helical and bow magnetic field morphologies manifest in two distinct environmental conditions, comparing the B_{LOS} morphologies in regions that are relatively isolated (such as Chameleon-Musca), with those that are influenced by their environment (e.g., Orion A; Soler et al. 2018) can shed light on the most probable 3D magnetic morphologies in different environments. Investigating the correlations between the B_{LOS} information of each region and its surrounding environment, specifically for regions with observed magnetic field reversal, will be a step forward towards understanding the most probable morphology(ies) and the effects of environment.

2) Upgrading my method: Two relatively straight-forward approaches to upgrade my method are: a) obtaining higher source density as explained above, and b) using more sophisticated chemical evolution codes. The chemical evolution code that I used assumed a homogeneous cloud without considering dynamical effects or the ambient Galactic magnetic field. Using a more sophisticated code, such as the SILCC project¹ (Seifried et al. 2017*b*), would help to further reduce uncertainties and produce more accurate B_{LOS} calculations.

3) B_{POS} dust polarisation data: After determining the B_{LOS} vectors for regions with field reversals, combining B_{LOS} with B_{POS} provides insight into the 3D magnetic morphology. While this thesis used the Planck results in Orion A, there are other telescopes that can provide more and better measurements of B_{POS} in other clouds (e.g. APEX, BLASTPOL, BLASTPOL2, JCMT, etc). These observations, along with new and improved measurements of B_{LOS} using my technique, will be key to mapping and understanding the 3D magnetic fields.

6.3.2 Theoretical Simulations

To more rigorously investigate helical or bow magnetic fields, it is important to examine different factors involved. These factors include external flow along the long axis of the

¹<https://hera.ph1.uni-koeln.de/~silcc/>

filamentary structure in a non-ideal MHD environment, external accretion flow perpendicular to a rotating filament, recurrent shocks from the surrounding environment, and etc. Recurrent shocks can hypothetically bend the field lines around the filamentary structure (Heiles 1997) and influence its evolution. My existing simulations should be modified to include these factors, to see if these conditions will result in twisting of the field lines and production of the observed reversal across the rotating filament. In addition, different rotation rates and magnetic field strengths should be explored to see if any combination of these can wrap the magnetic field lines around the filaments.

Rigorous theoretical and observational studies will help us find the most likely magnetic field morphologies in filamentary molecular clouds to explain the observed B_{LOS} direction change across the filamentary structures. Different magnetic morphologies are associated with different environmental conditions and have different formation and evolution mechanisms. Investigating these morphologies will not only expand our knowledge on the role magnetism plays in star formation, it will also help reveal important information about feedback mechanisms from already formed stars. Therefore, investigating these morphologies can potentially make significant contributions in our understanding of the different phases in star formation.

Bibliography

- Andersson, B.-G. (2015), Interstellar Grain Alignment: Observational Status, *in* A. Lazarian, E. M. de Gouveia Dal Pino and C. Melioli, eds, ‘Magnetic Fields in Diffuse Media’, Vol. 407 of *Astrophysics and Space Science Library*, p. 59.
- Andersson, B.-G., Lazarian, A. and Vaillancourt, J. E. (2015), ‘Interstellar Dust Grain Alignment’, *ARA&A* **53**, 501–539.
- André, P., Di Francesco, J., Ward-Thompson, D., Inutsuka, S.-I., Pudritz, R. E. and Pineda, J. E. (2014), ‘From Filamentary Networks to Dense Cores in Molecular Clouds: Toward a New Paradigm for Star Formation’, *Protostars and Planets VI* pp. 27–51.
- André, P., Men’shchikov, A., Bontemps, S., Könyves, V., Motte, F., Schneider, N., Didelon, P., Minier, V., Saraceno, P., Ward-Thompson, D., di Francesco, J., White, G., Molinari, S., Testi, L., Abergel, A., Griffin, M., Henning, T., Royer, P., Merín, B., Vavrek, R., Attard, M., Arzoumanian, D., Wilson, C. D., Ade, P., Aussel, H., Baluteau, J.-P., Benedettini, M., Bernard, J.-P., Blommaert, J. A. D. L., Cambrésy, L., Cox, P., di Giorgio, A., Hargrave, P., Hennemann, M., Huang, M., Kirk, J., Krause, O., Launhardt, R., Leeks, S., Le Pennec, J., Li, J. Z., Martin, P. G., Maury, A., Olofsson, G., Omont, A., Peretto, N., Pezzuto, S., Prusti, T., Roussel, H., Russeil, D., Sauvage, M., Sibthorpe, B., Sicilia-Aguilar, A., Spinoglio, L., Waelkens, C., Woodcraft, A. and Zavagno, A. (2010), ‘From filamentary clouds to prestellar cores to the stellar IMF: Initial highlights from the Herschel Gould Belt Survey’, *A&A* **518**, L102.

- Arzoumanian, D., André, P., Didelon, P., Könyves, V., Schneider, N., Men'shchikov, A., Sousbie, T., Zavagno, A., Bontemps, S., di Francesco, J., Griffin, M., Hennemann, M., Hill, T., Kirk, J., Martin, P., Minier, V., Molinari, S., Motte, F., Peretto, N., Pezzuto, S., Spinoglio, L., Ward-Thompson, D., White, G. and Wilson, C. D. (2011), ‘Characterizing interstellar filaments with Herschel in IC 5146’, *A&A* **529**, L6.
- Arzoumanian, D., Shimajiri, Y., Inutsuka, S.-i., Inoue, T. and Tachihara, K. (2018), ‘Molecular filament formation and filament-cloud interaction: Hints from Nobeyama 45 m telescope observations’, *PASJ* **70**, 96.
- Babcock, H. W. (1953), ‘Magnetic Observations of HD 188041 and HD 133029’, *PASP* **65**, 194.
- Bachiller, R. and Cernicharo, J. (1984), ‘Molecular observations of B 1 - A dense globule in Perseus’, *A&A* **140**, 414–420.
- Bachiller, R. and Cernicharo, J. (1986), ‘Physical and chemical conditions in Perseus globules from NH₃ and HC₃N observations’, *A&A* **168**, 262–270.
- Bally, J., Langer, W. D. and Liu, W. (1991), ‘Infrared dust and millimeter-wave carbon monoxide emission in the Orion region’, *ApJ* **383**, 645–663.
- Bally, J., Walawender, J., Johnstone, D., Kirk, H. and Goodman, A. (2008), The Perseus Cloud, in B. Reipurth, ed., ‘Handbook of Star Forming Regions, Volume I’, Astronomical Society of the Pacific, p. 308.
- Banerjee, R., Pudritz, R. E. and Holmes, L. (2004), ‘The formation and evolution of protostellar discs; three-dimensional adaptive mesh refinement hydrosimulations of collapsing, rotating Bonnor-Ebert spheres’, *MNRAS* **355**, 248–272.
- Barnes, J. and Hut, P. (1986), ‘A hierarchical $O(n \log n)$ force-calculation algorithm’, *Nature* **324**(6096).

- Bate, M. R. (2009), ‘Stellar, brown dwarf and multiple star properties from hydrodynamical simulations of star cluster formation’, *MNRAS* **392**, 590–616.
- Bergin, E. A., Hartmann, L. W., Raymond, J. C. and Ballesteros-Paredes, J. (2004), ‘Molecular Cloud Formation behind Shock Waves’, *ApJ* **612**, 921–939.
- Bergin, E. A., Langer, W. D. and Goldsmith, P. F. (1995), ‘Gas-phase chemistry in dense interstellar clouds including grain surface molecular depletion and desorption’, *ApJ* **441**, 222–243.
- Bergin, E. A., Plume, R., Williams, J. P. and Myers, P. C. (1999), ‘The Ionization Fraction in Dense Molecular Gas. II. Massive Cores’, *ApJ* **512**, 724–739.
- Berman, P. R. (2010), ‘Optical Faraday rotation’, *AAPT* **78**.
- Blitz, L. (1987), The structure of molecular clouds, in G. E. Morfill and M. Scholer, eds, ‘NATO ASIC Proc. 210: Physical Processes in Interstellar Clouds’, pp. 35–58.
- Bohlin, R. C., Savage, B. D. and Drake, J. F. (1977), ‘A survey of interstellar HI from L alpha absorption measurements 2’, *NASA STI/Recon Technical Report N* **78**.
- Bolton, J. G. and Wild, J. P. (1957), ‘On the Possibility of Measuring Interstellar Magnetic Fields by 21-CM Zeeman Splitting.’, *ApJ* **125**, 296.
- Broten, N. W., MacLeod, J. M. and Vallee, J. P. (1988), ‘Catalogue of unambiguous (Faraday-thin, one-component, spectrum-selected) rotation measures for galaxies and quasars’, *Ap&SS* **141**, 303–331.
- Brown, J.-A. C. (2002), The magnetic field in the outer galaxy, PhD thesis, UNIVERSITY OF CALGARY (CANADA).
- Brown, J. C., Haverkorn, M., Gaensler, B. M., Taylor, A. R., Bizunok, N. S., McClure-Griffiths, N. M., Dickey, J. M. and Green, A. J. (2007), ‘Rotation Measures of Extragalactic Sources

- behind the Southern Galactic Plane: New Insights into the Large-Scale Magnetic Field of the Inner Milky Way', *ApJ* **663**, 258–266.
- Brown, J. C., Stil, J. M. and Landecker, T. L. (2008), 'Visualizing the Invisible using Polarisation Observations', *Physics in Canada* **64**.
- Brown, J. C. and Taylor, A. R. (2001), 'The Structure of the Magnetic Field in the Outer Galaxy from Rotation Measure Observations through the Disk', *ApJ* **563**, L31–L34.
- Brown, J. C., Taylor, A. R. and Jackel, B. J. (2003), 'Rotation Measures of Compact Sources in the Canadian Galactic Plane Survey', *ApJS* **145**, 213–223.
- Buckle, J. V., Davis, C. J., Francesco, J. D., Graves, S. F., Nutter, D., Richer, J. S., Roberts, J. F., Ward-Thompson, D., White, G. J., Brunt, C., Butner, H. M., Cavanagh, B., Chrysostomou, A., Curtis, E. I., Duarte-Cabral, A., Etxaluze, M., Fich, M., Friberg, P., Friesen, R., Fuller, G. A., Greaves, J. S., Hatchell, J., Hogerheijde, M. R., Johnstone, D., Matthews, B., Matthews, H., Rawlings, J. M. C., Sadavoy, S., Simpson, R. J., Tothill, N. F. H., Tsamis, Y. G., Viti, S., Wouterloot, J. G. A. and Yates, J. (2012), 'The JCMT Legacy Survey of the Gould Belt: mapping ^{13}CO and C^{18}O in Orion A', *MNRAS* **422**, 521–541.
- Caselli, P., Benson, P. J., Myers, P. C. and Tafalla, M. (2002), 'Dense Cores in Dark Clouds. XIV. N_2H^+ (1-0) Maps of Dense Cloud Cores', *ApJ* **572**, 238–263.
- Castets, A., Duvert, G., Dutrey, A., Bally, J., Langer, W. D. and Wilson, R. W. (1990), 'A multi-transition study of carbon monoxide in the Orion A molecular cloud', *A&A* **234**, 469–486.
- Chen, C.-Y., King, P. K., Li, Z.-Y., Fissel, L. M. and Mazzei, R. R. (2018), 'A New Method to Trace Three-dimensional Magnetic Field Structure within Molecular Clouds Using Dust Polarization', *ArXiv e-prints*, **arXiv:1810.10020**.

- Churchwell, E., Babler, B. L., Meade, M. R., Whitney, B. A., Benjamin, R., Indebetouw, R., Cyganowski, C., Robitaille, T. P., Povich, M., Watson, C. and Bracker, S. (2009), ‘The Spitzer/GLIMPSE Surveys: A New View of the Milky Way’, *PASP* **121**, 213.
- Clark, P. C. and Glover, S. C. O. (2014), ‘On column density thresholds and the star formation rate’, *MNRAS* **444**, 2396–2414.
- Clarke, D. (2010), *Stellar Polarimetry*, Wiley, ISBN: 978-3-527-40895-5.
- Condon, J. J., Cotton, W. D., Greisen, E. W., Yin, Q. F., Perley, R. A., Taylor, G. B. and Broderick, J. J. (1998), ‘The NRAO VLA Sky Survey’, *AJ* **115**, 1693–1716.
- Contreras, Y., Rathborne, J. and Garay, G. (2013), ‘Structure and radial equilibrium of filamentary molecular clouds’, *MNRAS* **433**, 251–258.
- Cordes, J. M. and Lazio, T. J. W. (2001), ‘Anomalous Radio-Wave Scattering from Interstellar Plasma Structures’, *ApJ* **549**, 997–1010.
- Cox, D. P. (2005), ‘The Three-Phase Interstellar Medium Revisited’, *ARA&A* **43**, 337–385.
- Crutcher, R. (2005), Magnetic Fields and Star Formation, in K. T. Chyzy, K. Otmianowska-Mazur, M. Soida and R.-J. Dettmar, eds, ‘The Magnetized Plasma in Galaxy Evolution’, pp. 103–110.
- Crutcher, R. M. (1999), ‘Magnetic Fields in Molecular Clouds: Observations Confront Theory’, *ApJ* **520**, 706–713.
- Crutcher, R. M., Roberts, D. A., Troland, T. H. and Goss, W. M. (1999), ‘The Magnetic Field of the NGC 2024 Molecular Cloud’, *ApJ* **515**, 275–285.
- Crutcher, R. M. and Troland, T. H. (2008), ‘Testing Faraday Rotation Estimates of Magnetic Field Strengths toward Dark Clouds’, *ApJ* **685**, 281–284.

- Crutcher, R. M., Troland, T. H., Goodman, A. A., Heiles, C., Kazes, I. and Myers, P. C. (1993), ‘OH Zeeman observations of dark clouds’, *ApJ* **407**, 175–184.
- Crutcher, R. M., Troland, T. H., Lazareff, B. and Kazes, I. (1996), ‘CN Zeeman Observations of Molecular Cloud Cores’, *ApJ* **456**, 217.
- Crutcher, R. M., Troland, T. H., Lazareff, B., Paubert, G. and Kazès, I. (1999), ‘Detection of the CN Zeeman Effect in Molecular Clouds’, *ApJ* **514**, L121–L124.
- Crutcher, R. M., Wandelt, B., Heiles, C., Falgarone, E. and Troland, T. H. (2010), ‘Magnetic Fields in Interstellar Clouds from Zeeman Observations: Inference of Total Field Strengths by Bayesian Analysis’, *ApJ* **725**, 466–479.
- Davies, R. D. (1963), ‘The magnetic field of the Galaxy’, *Radiotekhnika* pp. 119–125.
- Davis, L. and Greenstein, J. L. (1949), ‘The Polarization of Starlight by Interstellar Dust Particles in a Galactic Magnetic Field’, *Physical Review* **75**, 1605–1605.
- Dawson, J. R. (2013), ‘The Supershell - Molecular Cloud Connection: Large-Scale Stellar Feedback and the Formation of the Molecular ISM’, *PASA* **30**, e025.
- Duarte-Cabral, A., Fuller, G. A., Peretto, N., Hatchell, J., Ladd, E. F., Buckle, J., Richer, J. and Graves, S. F. (2010), ‘The physical and dynamical structure of Serpens. Two very different sub-(proto)clusters’, *A&A* **519**, A27.
- Dutrey, A., Duvert, G., Castets, A., Langer, W. D., Bally, J. and Wilson, R. W. (1993), ‘A multi-transition study of carbon monoxide in the Orion A molecular cloud. II - C(O-18)’, *A&A* **270**, 468–476.
- Everett, J. E. and Zweibel, E. G. (2011), ‘The Interaction of Cosmic Rays with Diffuse Clouds’, *ApJ* **739**, 60.
- Falgarone, E., Troland, T. H., Crutcher, R. M. and Paubert, G. (2008), ‘CN Zeeman measurements in star formation regions’, *A&A* **487**, 247–252.

Federrath, C., Banerjee, R., Clark, P. C. and Klessen, R. S. (2010), ‘Modeling Collapse and Accretion in Turbulent Gas Clouds: Implementation and Comparison of Sink Particles in AMR and SPH’, *ApJ* **713**, 269–290.

Fernández-López, M., Arce, H. G., Looney, L., Mundy, L. G., Storm, S., Teuben, P. J., Lee, K., Segura-Cox, D., Isella, A., Tobin, J. J., Rosolowsky, E., Plunkett, A., Kwon, W., Kauffmann, J., Ostriker, E., Tassis, K., Shirley, Y. L. and Pound, M. (2014), ‘CARMA Large Area Star Formation Survey: Observational Analysis of Filaments in the Serpens South Molecular Cloud’, *ApJ* **790**, L19.

Fiege, J. D. and Pudritz, R. E. (1999), Helical Fields and Filamentary Molecular Clouds, *in* A. R. Taylor, T. L. Landecker and G. Joncas, eds, ‘New Perspectives on the Interstellar Medium’, Vol. 168 of *Astronomical Society of the Pacific Conference Series*, p. 248.

Fiege, J. D. and Pudritz, R. E. (2000a), ‘Helical fields and filamentary molecular clouds - I’, *MNRAS* **311**, 85–104.

Fiege, J. D. and Pudritz, R. E. (2000b), ‘Helical fields and filamentary molecular clouds - II. Axisymmetric stability and fragmentation’, *MNRAS* **311**, 105–119.

Fiege, J. D. and Pudritz, R. E. (2000c), ‘Polarized Submillimeter Emission from Filamentary Molecular Clouds’, *ApJ* **544**, 830–837.

Fissel, L. M., Ade, P. A. R., Angilè, F. E., Ashton, P., Benton, S. J., Devlin, M. J., Dober, B., Fukui, Y., Galitzki, N., Gandilo, N. N., Klein, J., Korotkov, A. L., Li, Z.-Y., Martin, P. G., Matthews, T. G., Moncelsi, L., Nakamura, F., Netterfield, C. B., Novak, G., Pascale, E., Poidevin, F., Santos, F. P., Savini, G., Scott, D., Shariff, J. A., Diego Soler, J., Thomas, N. E., Tucker, C. E., Tucker, G. S. and Ward-Thompson, D. (2016), ‘Balloon-Borne Submillimeter Polarimetry of the Vela C Molecular Cloud: Systematic Dependence of Polarization Fraction on Column Density and Local Polarization-Angle Dispersion’, *ApJ* **824**, 134.

- Flower, D. R., Pineau Des Forêts, G. and Walmsley, C. M. (2007), ‘The fractional ionization in dark molecular clouds’, *A&A* **474**, 923–930.
- Freidberg, J. P. (2014), *Ideal MHD*, Cambridge University Press, ISBN: 978-1-107-00625-6.
- Gibson, D., Plume, R., Bergin, E., Ragan, S. and Evans, N. (2009), ‘Molecular Line Observations of Infrared Dark Clouds. II. Physical Conditions’, *ApJ* **705**, 123–134.
- Girichidis, P., Federrath, C., Banerjee, R. and Klessen, R. S. (2011), ‘Importance of the initial conditions for star formation - I. Cloud evolution and morphology’, *MNRAS* **413**, 2741–2759.
- Glover, S. C. O. and Clark, P. C. (2012), ‘Star formation in metal-poor gas clouds’, *MNRAS* **426**, 377–388.
- Glover, S. C. O., Federrath, C., Mac Low, M.-M. and Klessen, R. S. (2010), ‘Modelling CO formation in the turbulent interstellar medium’, *MNRAS* **404**, 2–29.
- Goldsmith, P. F., Heyer, M., Narayanan, G., Snell, R., Li, D. and Brunt, C. (2008), ‘Large-Scale Structure of the Molecular Gas in Taurus Revealed by High Linear Dynamic Range Spectral Line Mapping’, *ApJ* **680**, 428–445.
- Goldsmith, P. F., Li, D. and Krčo, M. (2007), ‘The Transition from Atomic to Molecular Hydrogen in Interstellar Clouds: 21 cm Signature of the Evolution of Cold Atomic Hydrogen in Dense Clouds’, *ApJ* **654**, 273–289.
- Gómez, G. C., Vázquez-Semadeni, E. and Zamora-Avilés, M. (2018), ‘The magnetic field structure in molecular cloud filaments’, *MNRAS* **480**, 2939–2944.
- Gong, Y., Li, G. X., Mao, R. Q., Henkel, C., Menten, K. M., Fang, M., Wang, M. and Sun, J. X. (2018), ‘The Serpens filament at the onset of slightly supercritical collapse’, *A&A* **620**, A62.

- Goodman, A. A., Crutcher, R. M., Heiles, C., Myers, P. C. and Troland, T. H. (1989), ‘Measurement of magnetic field strength in the dark cloud Barnard 1’, *ApJ* **338**, L61–L64.
- Großschedl, J. E., Alves, J., Meingast, S., Ackerl, C., Ascenso, J., Bouy, H., Burkert, A., Forbrich, J., Fürnkranz, V., Goodman, A., Hacar, Á., Herbst-Kiss, G., Lada, C. J., Larreina, I., Leschinski, K., Lombardi, M., Moitinho, A., Mortimer, D. and Zari, E. (2018), ‘3D shape of Orion A from Gaia DR2’, *A&A* **619**, A106.
- Güver, T. and Özel, F. (2009), ‘The relation between optical extinction and hydrogen column density in the Galaxy’, *MNRAS* **400**, 2050–2053.
- Habing, H. J. (1968), ‘The interstellar radiation density between 912 Å and 2400 Å’, *Bull. Astron. Inst. Netherlands* **19**, 421.
- Hacar, A., Tafalla, M., Kauffmann, J. and Kovács, A. (2013), ‘Cores, filaments, and bundles: hierarchical core formation in the L1495/B213 Taurus region’, *A&A* **554**, A55.
- Hall, J. S. (1949), ‘Observations of the Polarized Light from Stars’, *Science* **109**, 166–167.
- Hall, J. S. (1955), The Polarization of Star Light from Stars behind Filamentary Structure, in ‘Liege International Astrophysical Colloquia’, Vol. 6 of *Liege International Astrophysical Colloquia*, pp. 543–546.
- Hall, J. S. and Mikesell, A. H. (1949), ‘Observations of polarized light from stars.’, *AJ* **54**, 187–188.
- Hanawa, T., Nakamura, F., Matsumoto, T., Nakano, T., Tatematsu, K., Umemoto, T., Kameya, O., Hirano, N., Hasegawa, T., Kaifu, N. and Yamamoto, S. (1993), ‘Effects of magnetic fields and rotation on the fragmentation of filamentary molecular clouds - Comparison of the theory with the Orion A cloud’, *ApJ* **404**, L83–L86.
- Harrison, S., Faure, A. and Tennyson, J. (2013), ‘CN excitation and electron densities in diffuse molecular clouds’, *MNRAS* **435**, 3541–3546.

Hartmann, L., Ballesteros-Paredes, J. and Bergin, E. A. (2001), ‘Rapid Formation of Molecular Clouds and Stars in the Solar Neighborhood’, *ApJ* **562**, 852–868.

Harvey, P. M., Fallscheer, C., Ginsburg, A., Terebey, S., André, P., Bourke, T. L., Di Francesco, J., Könyves, V., Matthews, B. C. and Peterson, D. E. (2013), ‘A First Look at the Auriga-California Giant Molecular Cloud with Herschel and the CSO: Census of the Young Stellar Objects and the Dense Gas’, *ApJ* **764**, 133.

Harvey-Smith, L., Madsen, G. J. and Gaensler, B. M. (2011), ‘Magnetic Fields in Large-diameter H II Regions Revealed by the Faraday Rotation of Compact Extragalactic Radio Sources’, *ApJ* **736**, 83.

Hasegawa, T. I. and Herbst, E. (1993), ‘Three-Phase Chemical Models of Dense Interstellar Clouds - Gas Dust Particle Mantles and Dust Particle Surfaces’, *MNRAS* **263**, 589.

Heiles, C. (1976), ‘The interstellar magnetic field’, *ARA&A* **14**, 1–22.

Heiles, C. (1987), Interstellar magnetic fields, *in* D. J. Hollenbach and H. A. Thronson, Jr., eds, ‘Interstellar Processes’, Vol. 134 of *Astrophysics and Space Science Library*, pp. 171–194.

Heiles, C. (1997), ‘A Holistic View of the Magnetic Field in the Eridanus/Orion Region’, *ApJS* **111**, 245–288.

Heiles, C., Goodman, A. A., McKee, C. F. and Zweibel, E. G. (1993), Magnetic fields in star-forming regions - Observations, *in* E. H. Levy and J. I. Lunine, eds, ‘Protostars and Planets III’, pp. 279–326.

Hennebelle, P. (2013), ‘On the origin of non-self-gravitating filaments in the ISM’, *A&A* **556**, A153.

Hentschel, K. (2009), *Zeeman Effect*, Compendium of Quantum Physics. Springer, Berlin Heidelberg. ISBN: 978-3-540-70626-7.

Heyer, M. H. and Brunt, C. M. (2004), ‘The Universality of Turbulence in Galactic Molecular Clouds’, *ApJ* **615**, L45–L48.

Hildebrand, R. H. (1988), ‘Magnetic alignment of grains’, *Astrophysical Letters and Communications* **26**, 263–275.

Hildebrand, R. H., Kirby, L., Dotson, J. L., Houde, M. and Vaillancourt, J. E. (2009), ‘Dispersion of Magnetic Fields in Molecular Clouds. I’, *ApJ* **696**, 567–573.

Hiltner, W. A. (1949), ‘Polarization of Light from Distant Stars by Interstellar Medium’, *Science* **109**, 165.

Hollenbach, D. J. and Tielens, A. G. G. M. (1995), Theoretical models of photodissociation regions (PDRs)., in G. Winnewisser and G. C. Pelz, eds, ‘The Physics and Chemistry of Interstellar Molecular Clouds’, Vol. 459 of *Lecture Notes in Physics*, Berlin Springer Verlag, pp. 164–174.

Hollenbach, D. J. and Tielens, A. G. G. M. (1997), ‘Dense Photodissociation Regions (PDRs)’, *ARA&A* **35**, 179–216.

Hollenbach, D. J. and Tielens, A. G. G. M. (1999), ‘Photodissociation regions in the interstellar medium of galaxies’, *Reviews of Modern Physics* **71**, 173–230.

Hoq, S., Clemens, D. P., Guzmán, A. E. and Cashman, L. R. (2017), ‘Tracing the Magnetic Field of IRDC G028.23-00.19 Using NIR Polarimetry’, *ApJ* **836**, 199.

Houde, M. (2011), Magnetic Fields in Three Dimensions, in P. Bastien, N. Manset, D. P. Clemens and N. St-Louis, eds, ‘Astronomical Polarimetry 2008: Science from Small to Large Telescopes’, Vol. 449 of *Astronomical Society of the Pacific Conference Series*, p. 213.

Houde, M., Bastien, P., Dotson, J. L., Dowell, C. D., Hildebrand, R. H., Peng, R., Phillips, T. G., Vaillancourt, J. E. and Yoshida, H. (2002), ‘On the Measurement of the Magnitude and Orientation of the Magnetic Field in Molecular Clouds’, *ApJ* **569**, 803–814.

Howard, C. S., Pudritz, R. E. and Harris, W. E. (2017), ‘Simulating radiative feedback and star cluster formation in GMCs - II. Mass dependence of cloud destruction and cluster properties’, *MNRAS* **470**, 3346–3358.

Howard, C. S., Pudritz, R. E., Harris, W. E. and Klessen, R. S. (2018), ‘Simulating the UV escape fractions from molecular cloud populations in star-forming dwarf and spiral galaxies’, *MNRAS* **475**, 3121–3134.

Hull, C. L. H., Girart, J. M., Tychoniec, Ł., Rao, R., Cortés, P. C., Pokhrel, R., Zhang, Q., Houde, M., Dunham, M. M., Kristensen, L. E., Lai, S.-P., Li, Z.-Y. and Plambeck, R. L. (2017), ‘ALMA Observations of Dust Polarization and Molecular Line Emission from the Class 0 Protostellar Source Serpens SMM1’, *ApJ* **847**, 92.

Hull, C. L. H. and Plambeck, R. L. (2015), ‘The 1.3mm Full-Stokes Polarization System at CARMA’, *Journal of Astronomical Instrumentation* **4**, 1550005.

Hutchinson, I. H. (1987), *Principles of plasma diagnostics*, Cambridge: Cambridge University Press. doi:10.1017/CBO9780511613630.

Inoue, T., Hennebelle, P., Fukui, Y., Matsumoto, T., Iwasaki, K. and Inutsuka, S.-i. (2018), ‘The formation of massive molecular filaments and massive stars triggered by a magnetohydrodynamic shock wave’, *PASJ* **70**, S53.

Johnstone, D. and Bally, J. (1999a), ‘JCMT/SCUBA Submillimeter Wavelength Imaging of the Integral-shaped Filament in Orion’, *ApJ* **510**, L49–L53.

Johnstone, D. and Bally, J. (1999b), ‘JCMT/SCUBA Submillimeter Wavelength Imaging of the Integral-shaped Filament in Orion’, *ApJ* **510**, L49–L53.

Johnstone, D. and Bally, J. (1999c), SCUBA-Mapping at the JCMT: The Orion Molecular Ridge, *in* V. Ossenkopf, J. Stutzki and G. Winnewisser, eds, ‘The Physics and Chemistry of the Interstellar Medium’.

- Johnstone, D. and Bally, J. (2006), ‘Large-Area Mapping at 850 μ m. V. Analysis of the Clump Distribution in the Orion A South Molecular Cloud’, *ApJ* **653**, 383–397.
- Kainulainen, J., Beuther, H., Henning, T. and Plume, R. (2009), ‘Probing the evolution of molecular cloud structure. From quiescence to birth’, *A&A* **508**, L35–L38.
- Killeen, N. E. B., Lo, K. Y. and Crutcher, R. (1992), ‘Zeeman measurements of the magnetic fields at the Galactic center’, *ApJ* **385**, 585–603.
- Kirk, H., Klassen, M., Pudritz, R. and Pillsworth, S. (2015), ‘The Role of Turbulence and Magnetic Fields in Simulated Filamentary Structure’, *ApJ* **802**, 75.
- Klassen, M., Kuiper, R., Pudritz, R. E., Peters, T., Banerjee, R. and Buntemeyer, L. (2014), ‘A General Hybrid Radiation Transport Scheme for Star Formation Simulations on an Adaptive Grid’, *ApJ* **797**, 4.
- Klassen, M., Peters, T. and Pudritz, R. E. (2012), ‘H II Region Variability and Pre-main-sequence Evolution’, *ApJ* **758**, 137.
- Klassen, M., Pudritz, R. E. and Kirk, H. (2017), ‘Filamentary flow and magnetic geometry in evolving cluster-forming molecular cloud clumps’, *MNRAS* **465**, 2254–2276.
- Kolmogorov, A. (1941), ‘The Local Structure of Turbulence in Incompressible Viscous Fluid for Very Large Reynolds’ Numbers’, *Akademiiia Nauk SSSR Doklady* **30**, 301–305.
- Kong, S., Lada, C. J., Lada, E. A., Román-Zúñiga, C., Bieging, J. H., Lombardi, M., Forbrich, J. and Alves, J. F. (2015), ‘The Relationship between the Dust and Gas-Phase CO across the California Molecular Cloud’, *ApJ* **805**, 58.
- Könyves, V., André, P., Men’shchikov, A., Palmeirim, P., Arzoumanian, D., Schneider, N., Roy, A., Didelon, P., Maury, A., Shimajiri, Y., Di Francesco, J., Bontemps, S., Peretto, N., Benedettini, M., Bernard, J.-P., Elia, D., Griffin, M. J., Hill, T., Kirk, J., Ladjelate, B., Marsh, K., Martin, P. G., Motte, F., Nguyêñ Luong, Q., Pezzuto, S., Roussel, H., Rygl,

- K. L. J., Sadavoy, S. I., Schisano, E., Spinoglio, L., Ward-Thompson, D. and White, G. J. (2015), ‘A census of dense cores in the Aquila cloud complex: SPIRE/PACS observations from the Herschel Gould Belt survey’, *A&A* **584**, A91.
- Kounkel, M., Hartmann, L., Loinard, L., Ortiz-León, G. N., Mioduszewski, A. J., Rodríguez, L. F., Dzib, S. A., Torres, R. M., Pech, G., Galli, P. A. B., Rivera, J. L., Boden, A. F., Evans, II, N. J., Briceño, C. and Tobin, J. J. (2017), ‘The Gould’s Belt Distances Survey (GOBELINS) II. Distances and Structure toward the Orion Molecular Clouds’, *ApJ* **834**, 142.
- Koyama, H. and Inutsuka, S.-i. (2002), ‘An Origin of Supersonic Motions in Interstellar Clouds’, *ApJ* **564**, L97–L100.
- Krumholz, M. R., Cunningham, A. J., Klein, R. I. and McKee, C. F. (2010), ‘Radiation Feedback, Fragmentation, and the Environmental Dependence of the Initial Mass Function’, *ApJ* **713**, 1120–1133.
- Kulsrud, R. M. (2005), *Plasma Physics for Astrophysics*, Princeton University Press, ISBN: 0-691-12073-0.
- Kunz, M. (2016), ‘Introduction to MHD, https://static.ias.edu/pitp/2016/sites/pitp/files/kunz_1.pdf’.
- Kunz, M. (2019), *Private communication*.
- Kunz, M. W. and Mouschovias, T. C. (2010), ‘The non-isothermal stage of magnetic star formation - II. Results’, *MNRAS* **408**, 322–341.
- Lada, C. J., Lombardi, M. and Alves, J. F. (2009), ‘The California Molecular Cloud’, *ApJ* **703**, 52–59.
- Larson, R. B. (1981), ‘Turbulence and star formation in molecular clouds’, *MNRAS* **194**, 809–826.

Larson, R. B. (1994), The Evolution of Molecular Clouds, in T. L. Wilson and K. J. Johnston, eds, ‘The Structure and Content of Molecular Clouds’, Vol. 439 of *Lecture Notes in Physics*, Springer Verlag, Berlin, p. 13.

Larson, R. B. (2003), ‘The physics of star formation’, *Reports on Progress in Physics* **66**, 1651–1697.

Le Teuff, Y. H., Millar, T. J. and Markwick, A. J. (2000), ‘The UMIST database for astrochemistry 1999’, *A&AS* **146**, 157–168.

Lee, D. (2013), ‘A solution accurate, efficient and stable unsplit staggered mesh scheme for three dimensional magnetohydrodynamics’, *Journal of Computational Physics* **243**, 269–292.

Lee, K. I., Fernández-López, M., Storm, S., Looney, L. W., Mundy, L. G., Segura-Cox, D., Teuben, P., Rosolowsky, E., Arce, H. G., Ostriker, E. C., Shirley, Y. L., Kwon, W., Kauffmann, J., Tobin, J. J., Plunkett, A. L., Pound, M. W., Salter, D. M., Volgenau, N. H., Chen, C.-Y., Tassis, K., Isella, A., Crutcher, R. M., Gammie, C. F. and Testi, L. (2014), ‘CARMA Large Area Star Formation Survey: Structure and Kinematics of Dense Gas in Serpens Main’, *ApJ* **797**, 76.

Li, H.-b., Fang, M., Henning, T. and Kainulainen, J. (2013), ‘The link between magnetic fields and filamentary clouds: bimodal cloud orientations in the Gould Belt’, *MNRAS* **436**, 3707–3719.

Li, H.-B., Goodman, A., Sridharan, T. K., Houde, M., Li, Z.-Y., Novak, G. and Tang, K. S. (2014), ‘The Link Between Magnetic Fields and Cloud/Star Formation’, *Protostars and Planets VI* pp. 101–123.

Li, H.-b. and Houde, M. (2008), ‘Probing the Turbulence Dissipation Range and Magnetic Field Strengths in Molecular Clouds’, *ApJ* **677**, 1151–1156.

Li, H.-B., Jiang, H., Fan, X., Gu, Q. and Zhang, Y. (2017), ‘The link between magnetic field orientations and star formation rates’, *Nature Astronomy* **1**, 0158.

Li, P. S., McKee, C. F. and Klein, R. I. (2015), ‘Magnetized interstellar molecular clouds - I. Comparison between simulations and Zeeman observations’, *MNRAS* **452**, 2500–2527.

Liu, T., Li, P. S., Juvela, M., Kim, K.-T., Evans, II, N. J., Di Francesco, J., Liu, S.-Y., Yuan, J., Tatematsu, K., Zhang, Q., Ward-Thompson, D., Fuller, G., Goldsmith, P. F., Koch, P. M., Sanhueza, P., Ristorcelli, I., Kang, S.-j., Chen, H.-R., Hirano, N., Wu, Y., Sokolov, V., Lee, C. W., White, G. J., Wang, K., Eden, D., Li, D., Thompson, M., Pattle, K. M., Soam, A., Nasedkin, E., Kim, J., Kim, G., Lai, S.-P., Park, G., Qiu, K., Zhang, C.-P., Alina, D., Eswaraiah, C., Falgarone, E., Fich, M., Greaves, J., Gu, Q.-L., Kwon, W., Li, H.-b., Malinen, J., Montier, L., Parsons, H., Qin, S.-L., Rawlings, M. G., Ren, Z.-Y., Tang, M., Tang, Y.-W., Toth, L. V., Wang, J., Wouterloot, J., Yi, H.-W. and Zhang, H.-W. (2018), ‘A Holistic Perspective on the Dynamics of G035.39-00.33: The Interplay between Gas and Magnetic Fields’, *ApJ* **859**, 151.

Lock, J. A. and Gouesbet, G. (2009), ‘Generalized lorenz–mie theory and applications’, *Journal of Quantitative Spectroscopy and Radiative Transfer* **110**(11), 800 – 807.
Light Scattering: Mie and More Commemorating 100 years of Mie’s 1908 publication.
URL: <http://www.sciencedirect.com/science/article/pii/S0022407308002653>

Lombardi, M. (2009), ‘NICEST, a near-infrared color excess method tailored to small-scale structures’, *A&A* **493**, 735–745.

Lombardi, M., Lada, C. J. and Alves, J. (2010), ‘2MASS wide field extinction maps. III. The Taurus, Perseus, and California cloud complexes’, *A&A* **512**, A67.

Mac Low, M.-M., Smith, M. D., Klessen, R. S. and Burkert, A. (1998), ‘The Decay of Supersonic and Super-Alfvénic Turbulence in Star-Forming Clouds’, *Ap&SS* **261**, 195–196.

Machida, M. N., Inutsuka, S.-I. and Matsumoto, T. (2011), ‘Effect of Magnetic Braking on Circumstellar Disk Formation in a Strongly Magnetized Cloud’, *PASJ* **63**, 555–573.

Macneice, P., Olson, K. M., Mobarry, C., de Fainchtein, R. and Packer, C. (2000), ‘Paramesh: A parallel adaptive mesh refinement community toolkit’, *Computer Physics Communications* **126**(3), 330–354.

MacNeice, P., Olson, K. M., Mobarry, C., de Fainchtein, R. and Packer, C. (2011), ‘PARAMESH V4.1: Parallel Adaptive Mesh Refinement’, Astrophysics Source Code Library.

URL: <https://sourceforge.net/projects/paramesh/>

Matsumoto, T., Nakamura, F. and Hanawa, T. (1994), ‘Fragmentation of a magnetized filamentary molecular cloud rotating around its axis’, *PASJ* **46**, 243–255.

Matthews, B. C., Wilson, C. D. and Fiege, J. D. (2001), ‘Magnetic Fields in Star-forming Molecular Clouds. II. The Depolarization Effect in the OMC-3 Filament of Orion A’, *ApJ* **562**, 400–423.

McKee, C. F. and Ostriker, E. C. (2007), ‘Theory of Star Formation’, *ARA&A* **45**, 565–687.

Mitchell, G. F., Johnstone, D., Moriarty-Schieven, G., Fich, M. and Tothill, N. F. H. (2001), ‘A Submillimeter Dust and Gas Study of the Orion B Molecular Cloud’, *ApJ* **556**, 215–229.

Mo, H., van den Bosch, F. C. and White, S. (2010), *Galaxy Formation and Evolution*, Cambridge, UK: Cambridge University Press.

Molinari, S., Schisano, E., Elia, D., Pestalozzi, M., Traficante, A., Pezzuto, S., Swinyard, B. M., Noriega-Crespo, A., Bally, J., Moore, T. J. T., Plume, R., Zavagno, A., di Giorgio, A. M., Liu, S. J., Pilbratt, G. L., Mottram, J. C., Russeil, D., Piazzo, L., Veneziani, M., Benedettini, M., Calzolatti, L., Faustini, F., Natoli, P., Piacentini, F., Merello, M., Palmese, A., Del Grande, R., Polychroni, D., Rygl, K. L. J., Polenta, G., Barlow, M. J., Bernard,

J.-P., Martin, P. G., Testi, L., Ali, B., André, P., Beltrán, M. T., Billot, N., Carey, S., Cesaroni, R., Compiègne, M., Eden, D., Fukui, Y., Garcia-Lario, P., Hoare, M. G., Huang, M., Joncas, G., Lim, T. L., Lord, S. D., Martinavarro-Armengol, S., Motte, F., Paladini, R., Paradis, D., Peretto, N., Robitaille, T., Schilke, P., Schneider, N., Schulz, B., Sibthorpe, B., Strafella, F., Thompson, M. A., Umana, G., Ward-Thompson, D. and Wyrowski, F. (2016), ‘Hi-GAL, the Herschel infrared Galactic Plane Survey: photometric maps and compact source catalogues. First data release for the inner Milky Way: $+68\text{deg} \geq l \geq -70\text{deg}$ ’, *A&A* **591**, A149.

Molinari, S., Swinyard, B., Bally, J., Barlow, M., Bernard, J.-P., Martin, P., Moore, T., Noriega-Crespo, A., Plume, R., Testi, L., Zavagno, A., Abergel, A., Ali, B., Anderson, L., André, P., Baluteau, J.-P., Battersby, C., Beltrán, M. T., Benedettini, M., Billot, N., Blommaert, J., Bontemps, S., Boulanger, F., Brand, J., Brunt, C., Burton, M., Calzoletti, L., Carey, S., Caselli, P., Cesaroni, R., Cernicharo, J., Chakrabarti, S., Chrysostomou, A., Cohen, M., Compiegne, M., de Bernardis, P., de Gasperis, G., di Giorgio, A. M., Elia, D., Faustini, F., Flagey, N., Fukui, Y., Fuller, G. A., Ganga, K., Garcia-Lario, P., Glenn, J., Goldsmith, P. F., Griffin, M., Hoare, M., Huang, M., Ikhenaode, D., Joblin, C., Joncas, G., Juvela, M., Kirk, J. M., Lagache, G., Li, J. Z., Lim, T. L., Lord, S. D., Marengo, M., Marshall, D. J., Masi, S., Massi, F., Matsuura, M., Minier, V., Miville-Deschénes, M.-A., Montier, L. A., Morgan, L., Motte, F., Mottram, J. C., Müller, T. G., Natoli, P., Neves, J., Olmi, L., Paladini, R., Paradis, D., Parsons, H., Peretto, N., Pestalozzi, M., Pezzuto, S., Piacentini, F., Piazzo, L., Polychroni, D., Pomarès, M., Popescu, C. C., Reach, W. T., Ristorcelli, I., Robitaille, J.-F., Robitaille, T., Rodón, J. A., Roy, A., Royer, P., Russeil, D., Saraceno, P., Sauvage, M., Schilke, P., Schisano, E., Schneider, N., Schuller, F., Schulz, B., Sibthorpe, B., Smith, H. A., Smith, M. D., Spinoglio, L., Stamatellos, D., Strafella, F., Stringfellow, G. S., Sturm, E., Taylor, R., Thompson, M. A., Traficante, A., Tuffs, R. J., Umana, G., Valenziano, L., Vavrek, R., Veneziani, M., Viti, S., Waelkens, C., Ward-Thompson, D., White, G., Wilcock, L. A., Wyrowski, F., Yorke, H. W. and Zhang,

- Q. (2010), ‘Clouds, filaments, and protostars: The Herschel Hi-GAL Milky Way’, *A&A* **518**, L100.
- Morlino, G. and Gabici, S. (2015), ‘Cosmic ray penetration in diffuse clouds’, *MNRAS* **451**, L100–L104.
- Mouschovias, T. (2001), Star Formation Models with Magnetic Fields, in G. Mathys, S. K. Solanki and D. T. Wickramasinghe, eds, ‘Magnetic Fields Across the Hertzsprung-Russell Diagram’, Vol. 248 of *Astronomical Society of the Pacific Conference Series*, p. 515.
- Mouschovias, T. C. (1985), ‘Star formation and the galactic magnetic field - The B-rho relation, flux freezing, and magnetic braking’, *A&A* **142**, 41–47.
- Mouschovias, T. C., Ciolek, G. E. and Morton, S. A. (2011), ‘Hydromagnetic waves in weakly-ionized media - I. Basic theory, and application to interstellar molecular clouds’, *MNRAS* **415**, 1751–1782.
- Mouschovias, T. C., Kunz, M. W. and Christie, D. A. (2009), ‘Formation of interstellar clouds: Parker instability with phase transitions’, *MNRAS* **397**, 14–23.
- Nakamura, F., Hanawa, T. and Nakano, T. (1993), ‘Fragmentation of filamentary molecular clouds with longitudinal and helical magnetic fields’, *PASJ* **45**, 551–566.
- Olmi, L. and Testi, L. (2002), ‘Constraints on star formation theories from the Serpens molecular cloud and protocluster’, *A&A* **392**, 1053–1068.
- Ostriker, J. (1964), ‘The Equilibrium of Polytropic and Isothermal Cylinders.’, *ApJ* **140**, 1056.
- Pacholczyk, A. G. (1970), *Radio astrophysics. Nonthermal processes in galactic and extra-galactic sources*, W.H. Freeman, San Francisco, ISBN: 0716703297.
- Padoan, P. and Nordlund, Å. (1999), ‘A Super-Alfvénic Model of Dark Clouds’, *ApJ* **526**, 279–294.

Padoan, P., Nordlund, Å., Rögnvaldsson, Ö. E. and Goodman, A. (2001), Turbulent Fragmentation and the Initial Conditions for Star Formation, *in* T. Montmerle and P. André, eds, ‘From Darkness to Light: Origin and Evolution of Young Stellar Clusters’, Vol. 243 of *Astronomical Society of the Pacific Conference Series*, p. 279.

Padovani, M. and Galli, D. (2013), Cosmic-Ray Propagation in Molecular Clouds, *in* D. F. Torres and O. Reimer, eds, ‘Cosmic Rays in Star-Forming Environments’, Vol. 34 of *Astrophysics and Space Science Proceedings*, p. 61.

Padovani, M., Galli, D. and Glassgold, A. E. (2009), ‘Cosmic-ray ionization of molecular clouds’, *A&A* **501**, 619–631.

Padovani, M., Marcowith, A., Hennebelle, P. and Ferrière, K. (2016), ‘Protostars: Forges of cosmic rays?’, *A&A* **590**, A8.

Palmeirim, P., André, P., Kirk, J., Ward-Thompson, D., Arzoumanian, D., Könyves, V., Didelon, P., Schneider, N., Benedettini, M., Bontemps, S., Di Francesco, J., Elia, D., Griffin, M., Hennemann, M., Hill, T., Martin, P. G., Men’shchikov, A., Molinari, S., Motte, F., Nguyen Luong, Q., Nutter, D., Peretto, N., Pezzuto, S., Roy, A., Rygl, K. L. J., Spinoglio, L. and White, G. L. (2013), ‘Herschel view of the Taurus B211/3 filament and striations: evidence of filamentary growth?’, *A&A* **550**, A38.

Papoutsakis, A., Sazhin, S. S., Begg, S., Danaila, I. and Luddens, F. (2018), ‘An efficient adaptive mesh refinement (amr) algorithm for the discontinuous galerkin method: Applications for the computation of compressible two-phase flows’, *Journal of Computational Physics* **363**, 399 – 427.

Pattle, K., Ward-Thompson, D., Berry, D., Hatchell, J., Chen, H.-R., Pon, A., Koch, P. M., Kwon, W., Kim, J., Bastien, P., Cho, J., Coudé, S., Di Francesco, J., Fuller, G., Furuya, R. S., Graves, S. F., Johnstone, D., Kirk, J., Kwon, J., Lee, C. W., Matthews, B. C., Mottram, J. C., Parsons, H., Sadavoy, S., Shinnaga, H., Soam, A., Hasegawa, T., Lai,

S.-P., Qiu, K. and Friberg, P. (2017), ‘The JCMT BISTRO Survey: The Magnetic Field Strength in the Orion A Filament’, *ApJ* **846**, 122.

Pattle, K., Ward-Thompson, D., Hasegawa, T., Bastien, P., Kwon, W., Lai, S.-P., Qiu, K., Furuya, R., Berry, D. and JCMT BISTRO Survey Team (2018), ‘First Observations of the Magnetic Field inside the Pillars of Creation: Results from the BISTRO Survey’, *ApJ* **860**, L6.

Planck Collaboration, Ade, P. A. R., Aghanim, N., Alves, M. I. R., Arnaud, M., Arzoumanian, D., Ashdown, M., Aumont, J., Baccigalupi, C., Banday, A. J., Barreiro, R. B., Bartolo, N., Battaner, E., Benabed, K., Benoît, A., Benoit-Lévy, A., Bernard, J.-P., Bersanelli, M., Bielewicz, P., Bock, J. J., Bonavera, L., Bond, J. R., Borrill, J., Bouchet, F. R., Boulanger, F., Bracco, A., Burigana, C., Calabrese, E., Cardoso, J.-F., Catalano, A., Chiang, H. C., Christensen, P. R., Colombo, L. P. L., Combet, C., Couchot, F., Crill, B. P., Curto, A., Cuttaia, F., Danese, L., Davies, R. D., Davis, R. J., de Bernardis, P., de Rosa, A., de Zotti, G., Delabrouille, J., Dickinson, C., Diego, J. M., Dole, H., Donzelli, S., Doré, O., Douspis, M., Ducout, A., Dupac, X., Efstathiou, G., Elsner, F., Enßlin, T. A., Eriksen, H. K., Falceta-Gonçalves, D., Falgarone, E., Ferrière, K., Finelli, F., Forni, O., Frailis, M., Fraisse, A. A., Franceschi, E., Frejsel, A., Galeotta, S., Galli, S., Ganga, K., Ghosh, T., Giard, M., Gjerløw, E., González-Nuevo, J., Górski, K. M., Gregorio, A., Gruppuso, A., Gudmundsson, J. E., Guillet, V., Harrison, D. L., Helou, G., Hennebelle, P., Henrot-Versillé, S., Hernández-Monteagudo, C., Herranz, D., Hildebrandt, S. R., Hivon, E., Holmes, W. A., Hornstrup, A., Huffenberger, K. M., Hurier, G., Jaffe, A. H., Jaffe, T. R., Jones, W. C., Juvela, M., Keihänen, E., Keskitalo, R., Kisner, T. S., Knoche, J., Kunz, M., Kurki-Suonio, H., Lagache, G., Lamarre, J.-M., Lasenby, A., Lattanzi, M., Lawrence, C. R., Leonardi, R., Levrier, F., Liguori, M., Lilje, P. B., Linden-Vørnle, M., López-Caniego, M., Lubin, P. M., Macías-Pérez, J. F., Maino, D., Mandolesi, N., Mangilli, A., Maris, M., Martin, P. G., Martínez-González, E., Masi, S., Matarrese, S., Melchiorri, A., Mendes, L., Mennella, A.,

Migliaccio, M., Miville-Deschénes, M.-A., Moneti, A., Montier, L., Morgante, G., Mortlock, D., Munshi, D., Murphy, J. A., Naselsky, P., Nati, F., Netterfield, C. B., Noviello, F., Novikov, D., Novikov, I., Oppermann, N., Oxborrow, C. A., Pagano, L., Pajot, F., Paladini, R., Paoletti, D., Pasian, F., Perotto, L., Pettorino, V., Piacentini, F., Piat, M., Pierpaoli, E., Pietrobon, D., Plaszczynski, S., Pointecouteau, E., Polenta, G., Ponthieu, N., Pratt, G. W., Prunet, S., Puget, J.-L., Rachen, J. P., Reinecke, M., Remazeilles, M., Renault, C., Renzi, A., Ristorcelli, I., Rocha, G., Rossetti, M., Roudier, G., Rubiño-Martín, J. A., Rusholme, B., Sandri, M., Santos, D., Savelainen, M., Savini, G., Scott, D., Soler, J. D., Stolyarov, V., Sudiwala, R., Sutton, D., Suur-Uski, A.-S., Sygnet, J.-F., Tauber, J. A., Terenzi, L., Toffolatti, L., Tomasi, M., Tristram, M., Tucci, M., Umana, G., Valenziano, L., Valiviita, J., Van Tent, B., Vielva, P., Villa, F., Wade, L. A., Wandelt, B. D., Wehus, I. K., Ysard, N., Yvon, D. and Zonca, A. (2016), ‘Planck intermediate results. XXXV. Probing the role of the magnetic field in the formation of structure in molecular clouds’, *A&A* **586**, A138.

Pon, A., Johnstone, D. and Heitsch, F. (2011), ‘Modes of Star Formation in Finite Molecular Clouds’, *ApJ* **740**, 88.

Pon, A., Toalá, J. A., Johnstone, D., Vázquez-Semadeni, E., Heitsch, F. and Gómez, G. C. (2012), ‘Aspect Ratio Dependence of the Free-fall Time for Non-spherical Symmetries’, *ApJ* **756**, 145.

Reich, W., Fürst, E., Reich, P., Wielebinski, R. and Wolleben, M. (2002), Polarization surveys of the galaxy, *in* S. Cecchini, S. Cortiglioni, R. Sault and C. Sbarra, eds, ‘Astrophysical Polarized Backgrounds’, Vol. 609 of *American Institute of Physics Conference Series*, pp. 3–8.

Reissl, S., Stutz, A. M., Brauer, R., Pellegrini, E. W., Schleicher, D. R. G. and Klessen, R. S. (2018), ‘Magnetic fields in star-forming systems (I): idealized synthetic signatures of dust polarization and Zeeman splitting in filaments’, *MNRAS* **481**, 2507–2522.

Richardson, L. F. (1922), *Weather prediction by numerical process*, Cambridge University Press, London.

Robishaw, T. (2008), Magnetic Fields Near and Far: Galactic and Extragalactic Single-Dish Radio Observations of the Zeeman Effect, PhD thesis, University of California, Berkeley.

Röllig, M., Abel, N. P., Bell, T., Bensch, F., Black, J., Ferland, G. J., Jonkheid, B., Kamp, I., Kaufman, M. J., Le Bourlot, J., Le Petit, F., Meijerink, R., Morata, O., Ossenkopf, V., Roueff, E., Shaw, G., Spaans, M., Sternberg, A., Stutzki, J., Thi, W.-F., van Dishoeck, E. F., van Hoof, P. A. M., Viti, S. and Wolfire, M. G. (2007), ‘A photon dominated region code comparison study’, *A&A* **467**, 187–206.

Rybicki, G. B. and Lightman, A. P. (1986), *Radiative Processes in Astrophysics*, Wiley-VCH , ISBN: 0-471-82759-2.

Ryden, B., Peterson, B. M. and Demianski, M. (2010), ‘Foundations of Astrophysics’, *American Journal of Physics* **78**, 127–127.

Salji, C. J., Richer, J. S., Buckle, J. V., di Francesco, J., Hatchell, J., Hogerheijde, M., Johnstone, D., Kirk, H., Ward-Thompson, D. and JCMT GBS Consortium (2015), ‘The JCMT Gould Belt Survey: properties of star-forming filaments in Orion A North’, *MNRAS* **449**, 1782–1796.

Schisano, E., Rygl, K. L. J., Molinari, S., Busquet, G., Elia, D., Pestalozzi, M., Polychroni, D., Billot, N., Carey, S., Paladini, R., Noriega-Crespo, A., Moore, T. J. T., Plume, R., Glover, S. C. O. and Vázquez-Semadeni, E. (2014), ‘The Identification of Filaments on Far-infrared and Submillimiter Images: Morphology, Physical Conditions and Relation with Star Formation of Filamentary Structure’, *ApJ* **791**, 27.

Schleicher, D. R. G. and Stutz, A. (2018), ‘Magnetic tension and instabilities in the Orion A integral-shaped filament’, *MNRAS* **475**, 121–127.

- Schnee, S., Mason, B., Di Francesco, J., Friesen, R., Li, D., Sadavoy, S. and Stanke, T. (2014), ‘Evidence for large grains in the star-forming filament OMC 2/3’, *MNRAS* **444**, 2303–2312.
- Seifried, D., Pudritz, R. E., Banerjee, R., Duffin, D. and Klessen, R. S. (2012), ‘Magnetic fields during the early stages of massive star formation - II. A generalized outflow criterion’, *MNRAS* **422**, 347–366.
- Seifried, D. and Walch, S. (2015), ‘The impact of turbulence and magnetic field orientation on star-forming filaments’, *MNRAS* **452**, 2410–2422.
- Seifried, D., Walch, S., Girichidis, P., Naab, T., Wünsch, R., Klessen, R. S., Glover, S. C. O., Peters, T. and Clark, P. (2017a), ‘SILCC-Zoom: the dynamic and chemical evolution of molecular clouds’, *MNRAS* **472**, 4797–4818.
- Seifried, D., Walch, S., Girichidis, P., Naab, T., Wünsch, R., Klessen, R. S., Glover, S. C. O., Peters, T. and Clark, P. (2017b), ‘SILCC-Zoom: the dynamic and chemical evolution of molecular clouds’, *MNRAS* **472**, 4797–4818.
- Shibata, K. and Matsumoto, R. (1991), ‘Formation of giant molecular clouds and helical magnetic fields by the Parker instability’, *Nature* **353**, 633–635.
- Shu, F. H. (1992), *The physics of astrophysics. Volume II: Gas dynamics.*, University Science Books, Mill Valley, CA (USA), ISBN: 0-935702-65-2.
- Sivia, D. and Skilling, J. (2006), *Data Analysis A Bayesian Tutorial*, OUP Oxford, ISBN: 9780198568315.
- Smith, R. J., Glover, S. C. O., Clark, P. C., Klessen, R. S. and Springel, V. (2014), ‘CO-dark gas and molecular filaments in Milky Way-type galaxies’, *MNRAS* **441**, 1628–1645.
- Smith, R. J., Glover, S. C. O. and Klessen, R. S. (2014), ‘On the nature of star-forming filaments - I. Filament morphologies’, *MNRAS* **445**, 2900–2917.

- Soler, J. D., Bracco, A. and Pon, A. (2018), ‘The magnetic environment of the Orion-Eridanus superbubble as revealed by Planck’, *A&A* **609**, L3.
- Sousbie, T. (2011), ‘The persistent cosmic web and its filamentary structure - I. Theory and implementation’, *MNRAS* **414**, 350–383.
- Spitzer, L. (1978), *Physical processes in the interstellar medium*, Wiley-Interscience, New York, ISBN: 978-0-471-29335-4.
- Spitzer, L. and Tukey, J. W. (1949), ‘Interstellar Polarization, Galactic Magnetic Fields, and Ferromagnetism’, *Science* **109**, 461–462.
- Stil, J. M. and Hryhoriw, A. (2016), ‘Magnetic Field Strength in an Intermediate-velocity Ionized Filament in the First Galactic Quadrant’, *ApJ* **826**, 202.
- Stone, J. M., Ostriker, E. C. and Gammie, C. F. (1998), ‘Dissipation in Compressible Magnetohydrodynamic Turbulence’, *ApJ* **508**, L99–L102.
- Stutz, A. M. and Gould, A. (2016), ‘Slingshot mechanism in Orion: Kinematic evidence for ejection of protostars by filaments’, *A&A* **590**, A2.
- Tahani, M., Plume, R., Brown, J. C. and Kainulainen, J. (2018), ‘Helical magnetic fields in molecular clouds?. A new method to determine the line-of-sight magnetic field structure in molecular clouds’, *A&A* **614**, A100.
- Taylor, A. R., Stil, J. M. and Sunstrum, C. (2009), ‘A Rotation Measure Image of the Sky’, *ApJ* **702**, 1230–1236.
- Tritsis, A., Panopoulou, G. V., Mouschovias, T. C., Tassis, K. and Pavlidou, V. (2015), ‘Magnetic field-gas density relation and observational implications revisited’, *MNRAS* **451**, 4384–4396.
- Troland, T. H., Crutcher, R. M. and Kazes, I. (1986), ‘Detection of the OH Zeeman effect toward Orion A’, *ApJ* **304**, L57–L60.

- Troland, T. H. and Heiles, C. (1982), ‘The Zeeman effect in 21 centimeter line radiation - Methods and initial results’, *ApJ* **252**, 179–192.
- Troland, T. H., Heiles, C. and Goss, W. M. (1989), ‘Aperture synthesis observations of the 21 centimeter Zeeman effect toward Orion A’, *ApJ* **337**, 342–354.
- Truelove, J. K., Klein, R. I., McKee, C. F., Holliman, II, J. H., Howell, L. H. and Greenough, J. A. (1997), ‘The Jeans Condition: A New Constraint on Spatial Resolution in Simulations of Isothermal Self-gravitational Hydrodynamics’, *ApJ* **489**, L179–L183.
- Uchida, Y., Fukui, Y., Minoshima, Y., Mizuno, A. and Iwata, T. (1991), ‘Evidence for a rotating helical filament in L1641, part of the Orion cloud complex’, *Nature* **349**, 140–142.
- Valente, P. C. (2013), ‘Energy transfer and dissipation in equilibrium and nonequilibrium turbulence’, *arXiv e-prints* .
- Van Eck, C. L., Brown, J. C., Stil, J. M., Rae, K., Mao, S. A., Gaensler, B. M., Shukurov, A., Taylor, A. R., Havercorn, M., Kronberg, P. P. and McClure-Griffiths, N. M. (2011), ‘Modeling the Magnetic Field in the Galactic Disk Using New Rotation Measure Observations from the Very Large Array’, *ApJ* **728**, 97.
- Van Eck, C. L., Havercorn, M., Alves, M. I. R., Beck, R., de Bruyn, A. G., Enßlin, T., Farnes, J. S., Ferrière, K., Heald, G., Horellou, C., Horneffer, A., Iacobelli, M., Jelić, V., Martí-Vidal, I., Mulcahy, D. D., Reich, W., Röttgering, H. J. A., Scaife, A. M. M., Schnitzeler, D. H. F. M., Sobey, C. and Sridhar, S. S. (2017), ‘Faraday tomography of the local interstellar medium with LOFAR: Galactic foregrounds towards IC 342’, *A&A* **597**, A98.
- Verschuur, G. L. (1967), The Zeeman effect in interstellar clouds., in H. van Woerden, ed., ‘Radio Astronomy and the Galactic System’, Vol. 31 of *IAU Symposium*, p. 385.

- Verschuur, G. L. (1996), ‘New Zeeman Effect Measurements of Thermal OH Sources S106, Orion B, B1, and L134 at 1665 and 1667 MHz’, *AJ* **112**, 2718.
- Willacy, K. and Williams, D. A. (1993), ‘Desorption processes in molecular clouds - Quasi-steady-state chemistry’, *MNRAS* **260**, 635–642.
- Williams, J. P., Bergin, E. A., Caselli, P., Myers, P. C. and Plume, R. (1998), ‘The Ionization Fraction in Dense Molecular Gas. I. Low-Mass Cores’, *ApJ* **503**, 689–699.
- Wilson, T. L., Rohlf, K. and Hüttemeister, S. (2013), *Tools of Radio Astronomy*, Springer-Verlag Berlin Heidelberg, ISBN: 978-3-642-39949-7.
- Wolleben, M. and Reich, W. (2004a), ‘Faraday screens associated with local molecular clouds’, *A&A* **427**, 537–548.
- Wolleben, M. and Reich, W. (2004b), Modelling Faraday Screens in the Interstellar Medium, in B. Uyaniker, W. Reich and R. Wielebinski, eds, ‘The Magnetized Interstellar Medium’, pp. 99–104.
- Wünsch, R., Walch, S., Dinnbier, F. and Whitworth, A. (2018), ‘Tree-based solvers for adaptive mesh refinement code FLASH - I: gravity and optical depths’, *MNRAS* **475**, 3393–3418.
- Yusef-Zadeh, F., Wardle, M. and Parastaran, P. (1997), ‘The Nature of the Faraday Screen Toward the Galactic Center Nonthermal Filament G359.54+0.18’, *ApJ* **475**, L119–L122.